HIGH-RESOLUTION LABEL FREE IMAGING OF ENDOGENOUS CHROMOPHORES VIA NON-LINEAR PHOTOACOUSTIC MICROSCOPY

A Dissertation

by

SCOTT PRESTON MATTISON

Submitted to the Office of Graduate and Professional Studies of
Texas A&M University
in partial fulfillment of the requirements for the degree of

DOCTOR OF PHILOSOPHY

Chair of Committee,	Brian E. Applegate
Committee Members,	Raffaella Righetti
	Vladislav V. Yakovlev
	Alvin T. Yeh
Head of Department,	Anthony Guiseppi-Elie

May 2016

Major Subject: Biomedical Engineering

ABSTRACT

Molecular specific subcellular imaging of biological tissues is vital for understanding the mechanisms of various pathologies. Current technologies for subcellular absorption contrast imaging, such as fluorescence confocal microscopy, require exogenous contrast agents to gain access to relevant biomolecules. All non-fluorescing biomolecules must therefore be tagged by a fluorescent marker to be visible in fluorescence confocal images. While these markers are effective, they can change the local environments, and any exogenous contrast agent must first achieve FDA approval for wide-spread use in humans.

Photoacoustic microscopy (PAM) is a hybrid imaging modality combining optical absorption imaging with ultrasonic detection capable of endogenous absorption contrast. Unfortunately, traditional photoacoustic microscopy suffers from poor axial resolution, precluding it from three-dimensional subcellular imaging. High axial resolution may be lent to PAM through the addition of a pump-probe spectroscopy technique known as transient absorption. This high resolution PAM technique, known as transient absorption ultrasonic microscopy (TAUM) enables three-dimensional subcellular imaging of endogenous biomolecules.

The pump-probe spectroscopy properties inherent to TAUM provide optically resolved point spread functions, access to ground state recovery time, and access to transient absorption spectrum measurements. This manuscript describes the author's efforts to improve the processing capabilities of both PAM and TAUM.

In this manuscript various TAUM systems are designed and characterized in detail. A second generation TAUM system improves the processing speed of TAUM to enable processing in parallel with data acquisition. Following the improvements to processing, a novel optical schematic of TAUM is developed, greatly simplifying the design requirements of TAUM images. This system is validated by collecting volumetric images of erythrocytes in blood smears. This work enables any PAM system to be converted to a TAUM system through the addition of an optical modulator. The culmination of this work is a multispectral TAUM system hybridized with a confocal microscope to enable high resolution imaging with both scattering and absorption contrast of biological tissues. The capabilities of this PAM and TAUM are demonstrated by obtaining high resolution images of the endogenous chromophores: hemoglobin, melanin, and cytochrome C.

DEDICATION

For Snuffles and Indiana

ACKNOWLEDGEMENTS

I would like to thank my committee chair, Dr. Applegate, for investing the necessary time to help me succeed in my degree. I would also like to thank my committee members, Dr. Righetti, Dr. Yakovlev, and Dr. Yeh, for their guidance and support throughout the course of this research.

All of my colleagues at Texas A&M over the years have also been vital to my success. I would like to thank Dr. Ryan Shelton for his guidance and patience during my first year of graduate school. There are many other individuals who contributed to the success of this research over the years whether through direct involvement, useful discussions, or shared resources. For this, I would like to thank Esteban Carbajal, Xi Chen, Dr. Holly Gibbs, Carl Johnson, Wihan Kim, Sangmin Kim, Ryan Maxson, Eli Mondragon, Cory Olsovsky, Dr. Jesung Park, Kalyanramu Vemishetty, and Felipe Zambrano. Additional thanks go to my friends, colleagues, and the department faculty and staff for making my time at Texas A&M University a great experience. I also want to extend my gratitude to the National Science Foundation, which provided funding to my research.

I would also like to say thank you to my dogs who kept my feet warm as I wrote my dissertation, my wife, Ashley, whose patience, love, and support helped me complete my degree and thanks to my family for their love and support.

NOMENCLATURE

FPGA	Field Programmable Gate Array
HT	Hilbert Transform
MH	Microscope Head
MRI	Magnetic Resonance Imaging
OA-PAM	Off-axis Photoacoustic Microscopy
PAM	Photoacoustic Microscopy
QD	Quadrature Demodulation
SH	Second Harmonic
SL	Scan Lens
TAUM	Transient Absorption Ultrasonic Microscopy
TL	Tube Lens

TABLE OF CONTENTS

Page

Page

Page

LIST OF FIGURES

Page

Page

Page

CHAPTER I

INTRODUCTION AND LITERATURE REVIEW

Biomedical Imaging

Over the last century, biomedical imaging techniques have undergone rapid growth and development. Each step the biomedical imaging community has taken forward has provided novel insights into biological processes, aided in disease diagnosis, expanded the scientific understanding of biochemical pathways, and improved patient prognosis.

In the field of medical imaging, the advent of ultrasound imaging for medical purposes in the late 1940s [1] heralded the true beginnings of the biomedical imaging renaissance. By providing a non-invasive tool for imaging deep within tissue without the use of ionizing radiation, ultrasound has revolutionized many medical procedures and diagnostic techniques. Shortly after ultrasound found common usage in medical clinics, X-ray computed tomography [2] provided a mechanism for capturing three-dimensional reconstructions comprised of multiple two dimensional slices enabling whole body imaging. Similarly, the development of magnetic resonance imaging (MRI) in the 1970s [3] furthered the capabilities of deep tissue imaging and demonstrated the role of non-ionizing radiation for whole body imaging. Since their inception, each of these techniques has been improved upon and new avenues of medical diagnosis have become available. Ultrasound may now take advantage of the Doppler effect to detect movement of fluids within the body [4], [5]. MRI has been utilized to determine the movement of blood throughout the brain to perform brain activity scans through functional MRI [6]. The tools

for x-ray computed tomography are now utilized in positron emission tomography (PET), and single-photon emission computed tomography (SPECT). As opposed to x-ray computed tomography, which derives its signal from the varied absorption of an external radiation source, PET and SPECT both use exogenous contrast agents which produce high energy particles to identify regions of pathology within a whole body scan [7], [8]. All of these techniques provide information on the order of 10s to 100s of μm; however, there is a great deal of information that can be gained from tissue and cellular level imaging.

Cellular and Molecular Imaging

Prior to the invention of confocal microscopy in the 1950s, cellular imaging was done through the use of histology slides. The advent of confocal microscopy meant axial sectioning previously only available through precision slicing of biological samples was afforded to whole tissue imaging. Since the inception of confocal microscopy, high resolution imaging has established itself as a key tool for research in biology and biochemistry [9], [10]. Imaging biological samples with subcellular resolution provides insight into diseases from an early stage, enabling earlier diagnosis and better patient prognosis [11], [12].

Shortly after the development of traditional confocal microscopy, several techniques were developed to provide molecular contrast to high resolution imaging modalities. Obtaining the molecular content of a biological sample with high resolution can provide unique understanding of disease mechanisms, and improve disease diagnostic capabilities. Techniques that use high resolution optical molecular imaging can obtain comparable

information with that obtained from histopathological evaluation of tissue sections, without the need for tissue biopsy [13], [14]. Biopsy of tissue is currently the gold standard for diagnosis of most tissue pathologies; however, in addition to being highly invasive to the patient, as the biopsied tissue is dead, it cannot provide any information on dynamic molecular processes underlying the pathology in question. High resolution optical molecular imaging is an ideal tool to replace tissue biopsy for accessible anatomy because it is non-invasive and has excellent molecular specificity. In inaccessible anatomy, high resolution optical imaging is already being used to augment tissue biopsy and provide diagnostic information [15].

The most widely used three-dimensional optical imaging techniques are confocal fluorescence microscopy and two-photon fluorescence microscopy [16]–[18]. Newer methodologies which have gained rapid adoption over recent years include structured illumination microscopy [19] and selective plane illumination microscopy [20]. All of these techniques provide excellent subcellular resolution; however, each of these techniques collect signal via fluorescence emission. As a result, these techniques are limited to a small pool of endogenous fluorophores including nicotinamide adenine dinucleotide phosphate (NADP), flavins, and certain amino acids. In a research setting, the fields of biology and biochemistry have seen tremendous improvements due to the advent of genetically-linked fluorescent molecules [21] and targeted exogenous contrast agents. Unfortunately, these contrast agents are not ideal for human studies as genetically-linked fluorescent molecules would require introduction of foreign genes, which could lead to severe complications as well as facing many ethical implications [22].

Additionally, while exogenous contrast agents are commonly used in *ex vivo* and animal studies, it can still be difficult to obtain FDA approval for use in humans.

Other approaches to high resolution optical imaging techniques include second and third harmonic generation [23], and sum frequency generation [24]. Second harmonic generation is an ideal tool for imaging noncentro-symmetric molecules such as collagen [25], [26]; however, the pool of other exogenous contrast agents is extremely small. Coherent Anti-Stokes Raman Scattering (CARS) has been demonstrated to be an effective high resolution molecular imaging modality [27]. By measuring vibrational resonances of target molecules, CARS is applicable to a wide range of endogenous chromophores; nevertheless, as it is most efficient in a transmission geometry, thick biological samples are precluded from most forms of CARS imaging [28].

Since their development in the 1990s, super resolution optical imaging techniques have provided new information about molecular dynamics on a scale of tens of nanometers [29]–[31]. Similar to confocal fluorescence and two-photon absorption fluorescence microscopy, most super resolution techniques require the use of exogenous fluorophores, precluding them from *in vivo* human studies.

The Photoacoustic Effect

The photoacoustic effect is the generation of acoustic waves by the absorption of pulsed electromagnetic energy [32]. Through the photoacoustic effect, pulsed electromagnetic excitation is absorbed by a chromophore causing local thermoelastic expansion. The resulting pressure profile may be initially approximated by Equation 1

where β and C_p are the isobaric volumetric expansion coeffient and the specific heat of the sample respectively, c_s is the speed of sound in the media, μ_a is the absorption coefficient of the chromophore, and F is the fluence of the electromagnetic excitation [33].

$$P_0 \sim \frac{\beta {c_s}^2}{C_p} \mu_a F \tag{1}$$

To efficient generate photoacoustic signals, the excitation pulse width, τ_p, must be selected to meet the conditions of stress and thermal confinement. Stress confinement, defined in equation 2, requires that the excitation pulse width be shorter than the duration of acoustic propagation within excited area of the sample ($\tau_p < \tau_s$). Here, L_p is the characteristic linear dimension of the sample. Similarly, thermal confinement, defined in equation 3, requires the excitation pulse width to be less than the thermal diffusion time of the sample ($\tau_p < \tau_{Th}$). Here D_T is the thermal diffusivity of the sample. For most biological samples, D_T is approximately$1.4 \cdot 10^{-3}\, {cm^2}/{S}$ [33].

$$\tau_s = \frac{L_p}{c_s} \tag{2}$$

$$\tau_{Th} = \frac{{L_p}^2}{D_T} \tag{3}$$

The localized stress displacement generated by photoacoustic emission propagates through materials as acoustic and thermal waves until it reaches a detector or is fully attenuated [34]. These acoustic waves will cause surface deformation of materials from the range of 100s of pm up to 10s of μm based on material properties and fluence of the electromagnetic excitation [35]. Historically, PAM systems have utilized piezoelectric transducers to detect acoustic waves generated by optical excitation. These mechanical transducers require physical coupling between the sample and the transducer. Physical

coupling is generally accomplished using water meaning the sample typically is fully submerged. This pressure wave can then be detected with an ultrasound transducer, providing depth information about the chromophore through time-of-flight measurements of the recorded ultrasound signal.

Photoacoustic Microscopy

Photoacoustic microscopy (PAM), sometimes called optoacoustic microscopy, is a hybrid imaging modality which exploits the photoacoustic effect to provide optical absorption contrast via ultrasonic detection. Traditional approaches to PAM can provide optical diffraction limited lateral resolution and ultrasonic limited axial resolution. Photoacoustic microscopy has previously been utilized in a research setting to assess vascular disease, perform functional imaging of the brain, and screen for cancerous lesions [34], [36], [37]. The primary benefit of photoacoustic microscopy is increased imaging depth. Since ultrasonic radiation is attenuated three orders of magnitude less than visible radiation in tissue, PAM is able to image biological structures deeper than other high resolution optical imaging modalities [34]. A secondary benefit of PAM is the fact that the signal is generated through vibrational relaxation of the excited chromophores, not radiative transitions such as fluorescence or stimulated emission, resulting in a much larger pool of chromophores that may be reached by photoacoustic imaging as the majority of chromophores generally undergo relation electron relaxation through non-radiative pathways. For this reason, PAM may image many biological chromophores that are not accessible to fluorescence based absorption contrast techniques. Additionally, molecules

that exhibit fluorescence emission also exhibit photoacoustic emission at the same excitation wavelength.

While any molecule with sufficient absorption is a potential target for photoacoustic imaging, hemoglobin [38], cytochromes [39], myoglobin [40], melanin and DNA/RNA have been the most heavily investigated targets for biomedical photoacoustic research. Additional exogenous contrast agents have been developed for photoacoustic microscopy, including fluorescent dyes [41], gold nanoparticles [42], and non-fluorescent dyes [43].

Photoacoustic imaging is a widely scalable technique capable of performing ultrasonic confined tomographic measurements cm deep into tissue or optically confined microscopy measurements mm deep into tissue [44], [45]. The spatial resolution of photoacoustic tomography (PAT) is largely determined by the ability to reconstruct the sample from a variety of detectors and the bandwidth of the piezo crystal found in the ultrasound transducer [46]. Due to the ultrasonic detection and the lack of a need to focus the optical excitation, PAT is capable of providing a resolution on the order of 10s to 100s μm centimeters deep into tissue. To obtain higher resolution at shallower imaging depths, the transducer bandwidth may simply be increased with no other changes required to the imaging system. Unfortunately, this trade-off begins to limit photoacoustic imaging systems as they transition from the realm of tomography to the realm of microscopy [47]. The point spread function of a PAM system is limited axially by the bandwidth of the ultrasonic transducer as defined by Equation 4 below where PSF_Z denotes the axial point spread function, V_s denotes the speed of sound in tissue, and β denotes the bandwidth of the ultrasonic detector.

$$PSF_Z = \frac{0.88V_s}{\beta} \quad (4)$$

There are two primary approaches to PAM, acoustic resolution PAM and optical resolution PAM. In acoustic resolution PAM, unfocused light is shone onto the sample and the signal localization is achieved solely through the focused transducer parameters [48]. This results in axial and transverse resolutions on the order of 10s of μm at penetration depths up to cm. A second implementation of PAM, termed optical resolution PAM, uses focused optical excitation to localize the signal in the lateral dimensions [49]; however, the axial resolution is governed by the localization of acoustic signal by the bandwidth of the ultrasonic transducer. As a result the lateral resolution of PAM is comparable to other high-resolution optical imaging techniques; however, the axial resolution is still typically limited to 10s of μm.

Since the axial resolution of PAM is tied to the bandwidth of the ultrasonic transducer, higher axial resolution can be obtained by utilizing a larger bandwidth transducer. Unfortunately, as the frequency of acoustic waves increases the attenuation of acoustic waves in biological tissue also increases. At 25 MHz, the acoustic attenuation of water is 0.15 dB/mm; conversely, at 100 MHz, the acoustic attenuation of water is 2 dB/mm [47]. In order to achieve axial resolution equivalent to that of other high resolution optical imaging modalities (~1 μm), a bandwidth of 1.5 GHz would be required. At 1.5 GHz the attenuation in water is greater than 100 dB/mm. The large acoustic attenuation of tissue at high frequencies limits transducer bandwidth to roughly 100 MHz in order to maintain an imaging depth of at least 500 μm. This effectively limits the axial resolution of photoacoustic microscopy to ~10μm. While this is sufficient for mapping out most

vasculature, the current primary application of photoacoustic imaging, it is a significant barrier for utilizing PAM for optical molecular imaging of cellular structures in multiple planes or acquiring three-dimensional datasets of subcellular structures.

Several groups have proposed methods for improving the axial resolution of photoacoustic microscopy. Despite their limited penetration depth, custom-made large bandwidth transducers in combination with deconvolution techniques have been utilized to achieve axial section in photoacoustic microscopy [50]. This work demonstrated that small features generated acoustic signals that were frequency shifted to higher frequencies. Another group has developed a novel super resolution imaging technique termed photoacoustic nanoscopy capable of achieving lateral and axial sectioning on the order of 100 nm [51], [52]; unfortunately, this technique requires saturable chromophores to isolate the signal in space.

This work presented in this manuscript expands upon the merging of photoacoustic microscopy with pump-probe spectroscopy for a technique termed transient absorption ultrasonic microscopy (TAUM) [53]. The merging of photoacoustic microscopy and pump probe spectroscopy provides an optically resolved point spread function in all dimensions. This technology has the added benefit of providing increased molecular contrast and specificity compared to traditional PAM [54]. Additionally, by merging TAUM with scattering confocal microscopy it is possible to simultaneously acquire morphological and molecular information from the sample.

Confocal Microscopy

As indicated earlier, confocal microscopy offers significant advantages over traditional optical microscopy. The most significant of these advantages is the ability to perform optical sectioning even in thick biological samples [55]. In contrast to a wide field microscope, which illuminates the entire sample simultaneously, a confocal microscope scans a spot excitation across the sample point by point to build up an image [56].

The basic principle behind confocal microscopy is the presence of a pinhole in the conjugate imaging plane of the microscope focus. Figure 1 depicts the design of a basic confocal microscope. The pinhole acts as a spatial filter to eliminate out of focus light from the sample. This optical sectioning enables the acquisition of three dimensional images. To build an image, the excitation is scanned across the sample in the lateral dimension through either stage scanning or scanning of the laser beam in space. The axial dimension may be built up using either stage scanning or using tunable lenses [57].

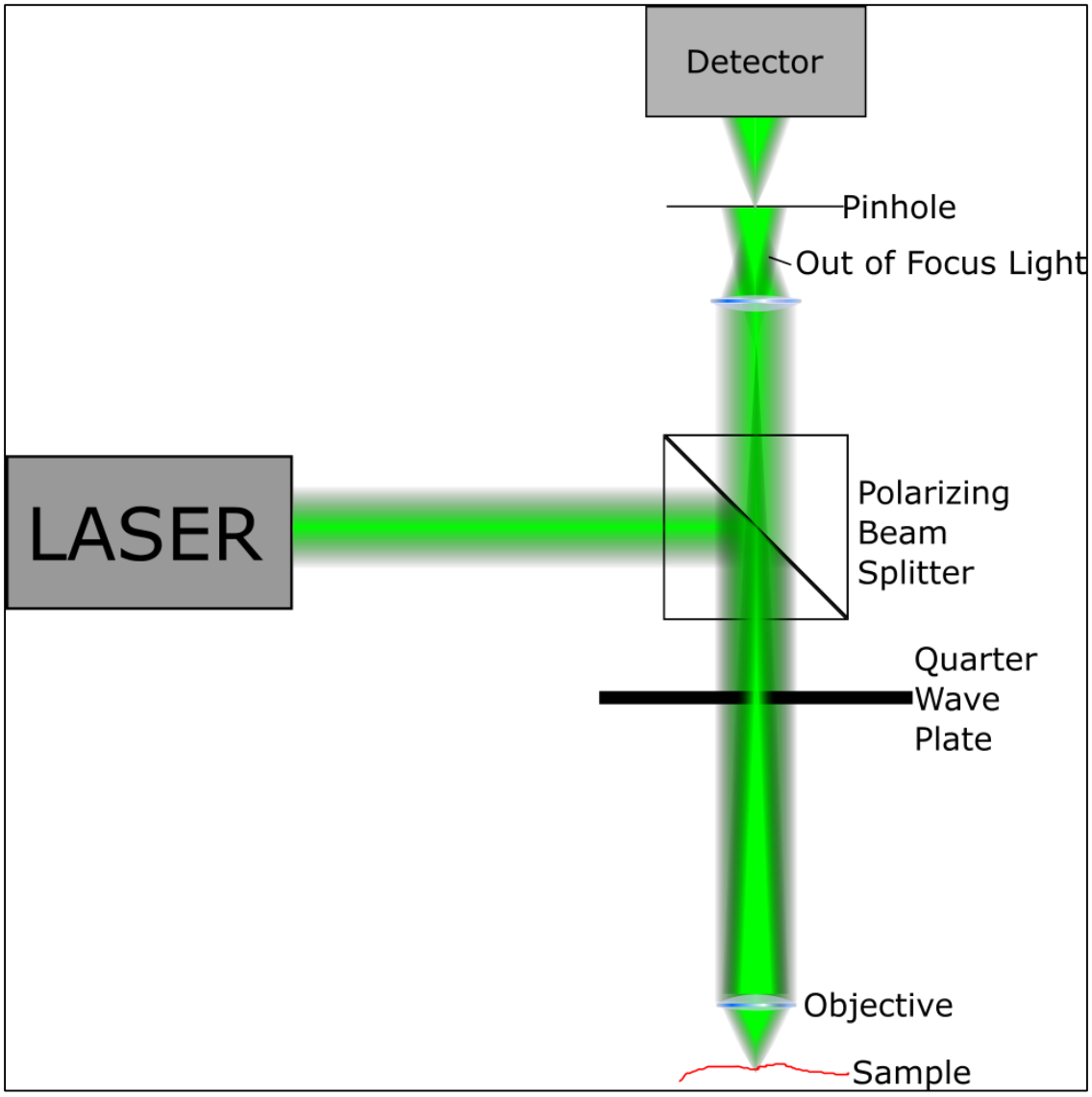

Figure 1. Simplified schematic diagram of a confocal microscopy system sensitive to optical scattering. The quarter wave plate and polarizing beam splitter act to direct light collected from the sample toward the confocal pinhole. The pinhole filters out any out of focus light from the sample; only signal from the focal spot of the objective is passed by the pinhole.

Confocal microscopy improves both the lateral resolution of the system as well as the axial resolution. The degree of improvement is related to the confocal parameter, which is defined by the size of the pinhole relative to the beam diameter [58]. In essence the pinhole

diameter determines the degree axial resolution of the image. The smaller the pinhole, the better the axial resolution; however, the smaller the pinhole, the less signal is acquired. This trade-off is a fundamental aspect of confocal microscopy and is a key consideration when determining pinhole size.

Pump-Probe Spectroscopy

The underlying process behind transient absorption ultrasonic microscopy (TAUM) is transient absorption. Transient absorption is typically measured with pump-probe absorption spectroscopy and commonly used to characterize molecular dynamics [59]. Nominally a molecule is excited with a pump and a probe pulse, separated in time by an interpulse delay. The pump pulse drives a molecule from its ground state to some excited state. This process transiently alters the absorption coefficient. The transient change can be measured by recording the absorption of the probe with the pump both on and off. The difference between the two is then the transient absorption signal [53]. Typically the pump is modulated at some frequency. The depth of modulation transferred to the probe is then the transient absorption signal.

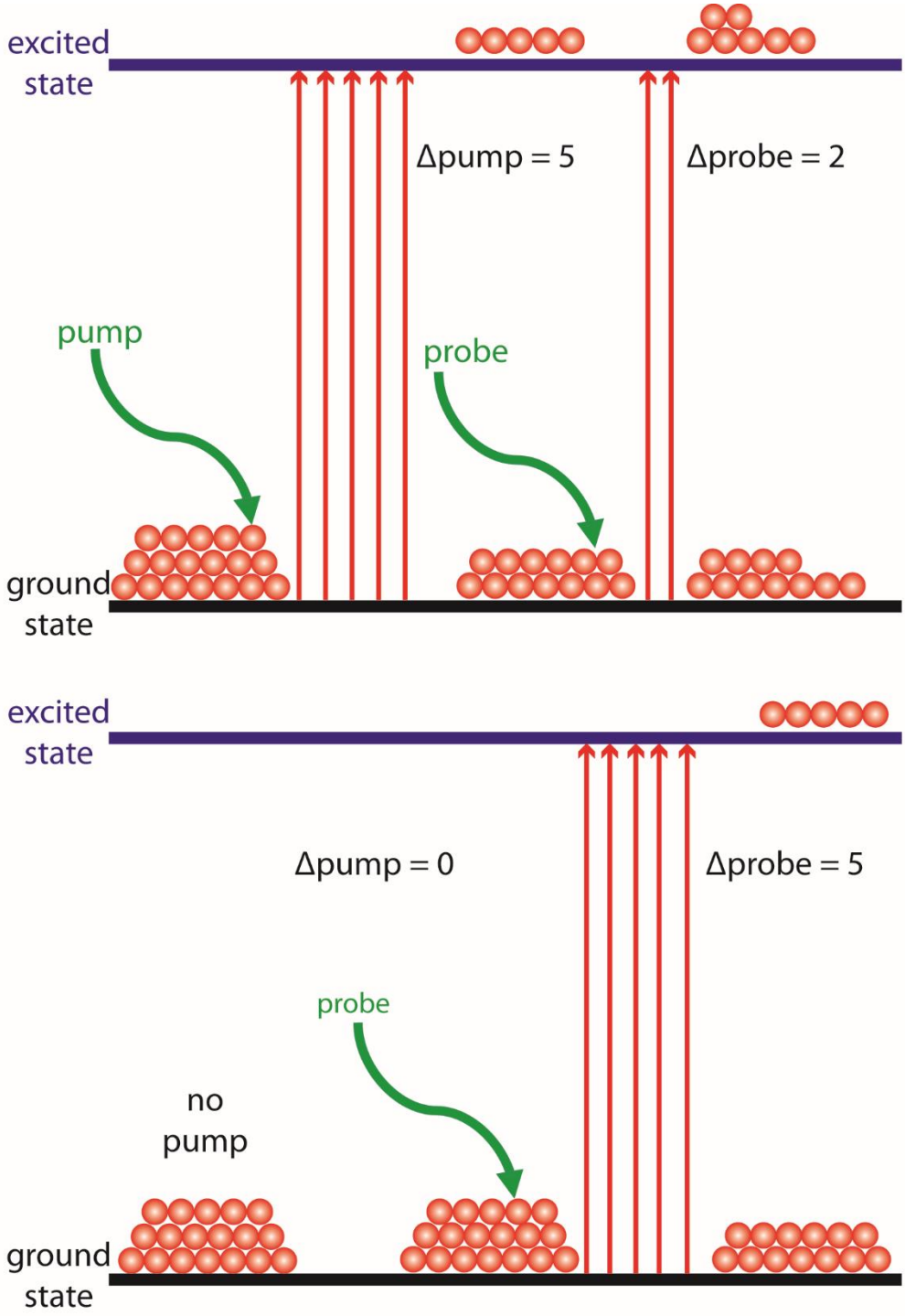

Figure 2. Schematic of a two level energy level diagram illustrating the transient absorption process. The left side of the diagram corresponds to when both the pump and the probe beams illuminate the sample. Meanwhile, the right side of the diagram depicts the condition when only the probe beam illuminates the sample. The difference in the net change is the result of the transient absorption process.

The phenomenon of two photon microscopy is illustrated as a 2-level energy diagram in Figure 2, where the x-axis corresponds to increasing time and the y-axis corresponds to increasing energy. As shown in the diagram, a pump pulse first drives a percentage of the total ground state electrons into a higher energy state. The probe pulse then drives a percentage of the remaining electrons into the higher energy state. The percentage of electrons driven by each pulse is defined by the Einstein coefficient B_{12} ($J^{-1}\ m^3\ s^{-2}$) which gives the probability per unit time per unit spectral energy density of the radiation field that an electron in state 1 will absorb a photon with an energy $E_2 - E_1 = hv$ and jump to state 2. With this in mind, observing the probe signal through either the amount of transmitted light, fluorescence emission, or photoacoustic emission, with and without the presence of the preceding pump pulse, provides insight into the electron dynamics of the molecule.

If the probe signal is measured as a function of the delay between the pump and probe pulses, the signal should map out as an exponential decay which has a characteristic lifetime known as the ground state recovery time. In a two level system, this is dependent upon the Einstein coefficient A_{21} (s^{-1}) which gives the probability per unit time that an electron in state 2 will decay spontaneously to state 1. Pump-probe spectroscopy has previously been harnessed for high-resolution molecular imaging of hemoglobin [60] and melanin [61], neither of which give off observable fluorescence. However, the imaging depth of this technique is typically limited to < 100 μm in a trans-illumination geometry.

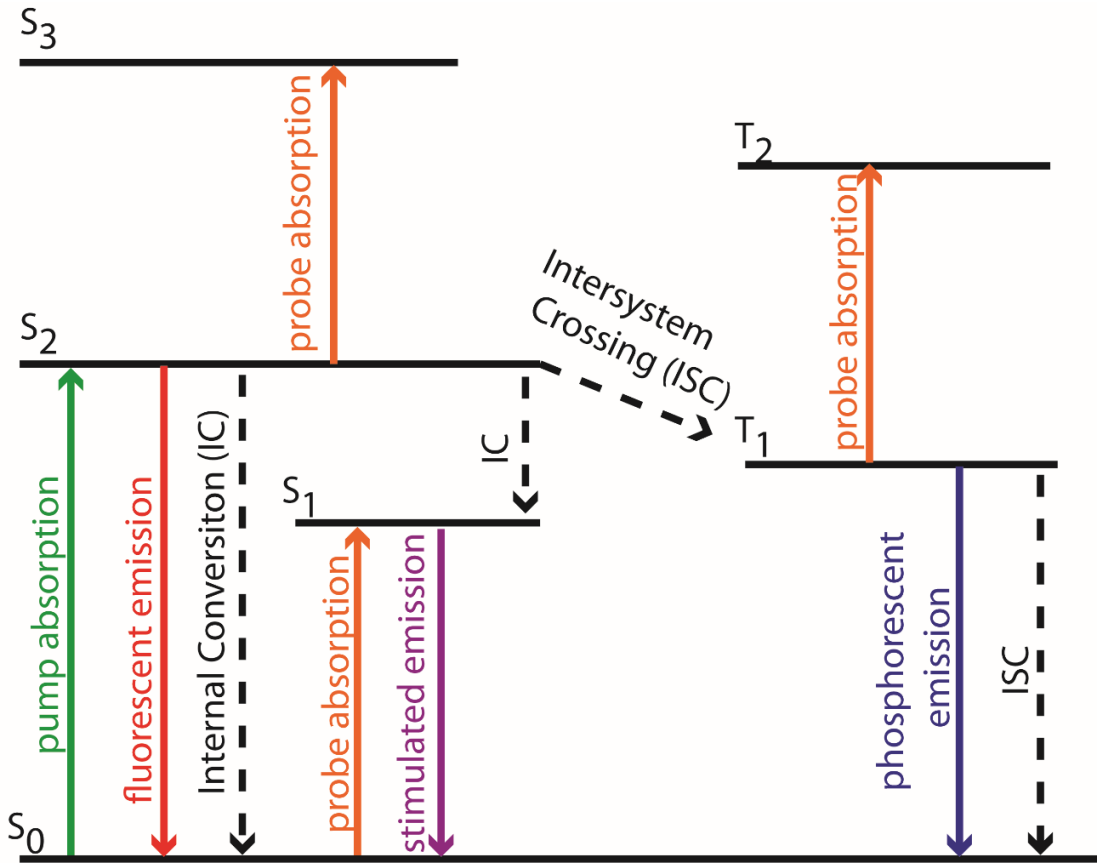

Figure 3. A multilevel Jablonski energy diagram showing various possible electronic transitions which may be probed through pump-probe spectroscopy.

It is important to note that a two level system is an oversimplification of all biologically relevant molecules. In reality, there are many possible electron state couplings which may be measured with pump-probe techniques. Figure 3 shows a schematic diagram listing many possible excitation and relaxation pathways. Depending upon the wavelength of the pump and probe pulses, as well as the allowable transitions in the molecule, each pathway may be measured using pump-probe techniques.

Potential Cellular and Molecular Targets

The primary target for most current photoacoustic microscopes is hemoglobin [37], [38], [46], [62]–[64]. As hemoglobin acts as the primary mode of oxygen transport in vertebrates [65], it is a readily available target in the erythrocytes of any healthy vertebrate. The oxidized (deoxygenated) and reduced (oxygenated) forms of hemoglobin have distinct absorption spectra that enable differentiation through the excitation wavelength [66]. Additionally, as will be discussed in detail later, the oxidized and reduced forms of hemoglobin present distinct ground state recovery times which may be measured using TAUM. Extensive work has previously been performed to differentiate between the oxidized and reduced forms of hemoglobin using photoacoustic microscopy and photoacoustic tomography as it provides a window into the oxygen metabolism of an organism [67]. Functional imaging of mouse and rat brains has been performed to observe the changes in oxygen concentration due to external stimuli [68], [69]. While interesting on a macro scale, subcellular imaging of hemoglobin oxygenation is more limited in its applications.

Cellular metabolic activity is a key indicator of cell health. When measured using optical methods, typically the endogenous fluorophores NADH and $FADH_2$ are used as secondary markers of cellular metabolism [70]. While both NADH and $FADH_2$ are potential targets for TAUM using a 355 nm pulsed laser source, photoacoustic microscopy is sensitive to molecules which may act as primary markers of cellular metabolism. Cytochrome C is one of many porphyrin molecules that are an integral component of the metabolic pathway [71]. Similar to hemoglobin, cytochrome C has distinct absorption

spectrum between its oxidized and reduced forms. By probing the oxidative state of cytochrome C, one can directly observe the transfer of elections between complex III and complex IV in the electron transport chain [72]. This would facilitate a direct measurement of cellular metabolic activity. This method of monitoring an oxidative pair of the electron transport chain instead of metabolic intermediates would provide more precise information on the cellular response to various external stimuli such as heat, pH, or the presence of exogenous compounds.

Fibroblasts are an excellent model cell for imaging of reduced cytochrome C *in vitro [52]*. Fibroblasts have a large number of highly active cellular mitochondria with little presence of porphyrins outside the mitochondria. Conversely, regardless of the presence of oxygen, most cancer cells predominately produce ATP through glycolysis followed by lactic fermentation rather than through the electron transport chain. This is known as the Warburg effect and is a result of the mutations that lead to malignant transformation [73]. For this reason, tumor cells will be an ideal target for observing oxidized cytochrome C *in vitro.*

Both DNA and RNA absorb strongly in the near UV with a peak at approximately 285 nm. DNA is typically a double stranded helix which contains the genetic hereditary information of an organism [74]. RNA is a typically a single stranded helix which contains the transcribed hereditary information that can be translated into proteins or other functional units [75]. While DNA and RNA helices are too small to resolve with traditional optical microscopy, the macromolecules composed of DNA known as chromatin, found in the nuclei of cells, is observable using optical microscopy. Chromatin structure has been

linked to cell development [76]. Any nucleated cell may be used an ideal target for chromatin imaging *in vitro*. It is important to note that absorption of UV light has been shown to cause mutations in cellular DNA, precluding any imaging in humans.

Melanin is one of the most abundant pigments in humans, yet its function has not been well characterized. It does not have a single molecular structure, but rather represents groups of molecules. There are three groups, eumelanin, pheomelanin, and neuoromelanin [77]. Within each of these three groups are molecular species with different physical properties and biochemical functions. The different forms of melanin play various roles in the function of the brain, ear, eyes, and skin [78]. Melanoma, an aggressive cancer, is endemic to each of these organs. Differentiation between eumelanin and pheomelanin can be obtained from their similar, yet distinct, absorption spectra. The presence of high amounts of pheomelanin has been causally linked to the harmful effects of ultraviolet radiation [78], [79]. Additionally, work in animal models and in cell culture has demonstrated that pheomelanin generates excess free radicals following exposure to ultraviolet light.

There are several potential targets for differentiating between eumelanin and pheomelanin. Differentiating types of melanin within melanocytes would have the largest impact and requires the ability to perform subcellular imaging. However, hair samples from a variety of individuals could easily provide a baseline for differentiating between quantities of eumalinin and pheomelanin. Hair samples from individuals with yellow to reddish hair will have higher quantities of pheomelanine. Conversely, eumelanin will be found in higher quantities from individuals with black to brown hair.

Other interesting potential molecular targets for TAUM include anthocyanins [80], carotenoids, chlorophylls in plants [81], and hemocyanins found in some invertebrates [82] including lobsters. Myoglobin is a potentially interesting target; however, attempts at imaging myoglobin *ex vivo* have yielded mixed results in photoacoustic microscopy [83]. Additionally, any endogenous or exogenous fluorophore may act as a molecular target for TAUM.

Field Programmable Gate Arrays

The rapid development of novel imaging techniques owes a debt to the development of improved computer processors of the 20th and 21st centuries. One of the primary requirements for an imaging system to be considered for clinical use is the production of real time image output. Hours or even minutes of post processing required before an acquired image is displayed causes problems when a decision needs to be made quickly based off the information gathered from the data acquisition [84].

Serial processors, such as those found in personal computers, excel at running operating systems and performing sequential tasks; however, they typically struggle with high performance computation and simulation. It is for this reason that both field programmable gate arrays (FPGAs) and graphic processing units (GPUs) are typically used in computing for accelerating complex calculations [85]. By offloading data from the central processing unit (CPU), performing the calculations in parallel on the FPGA or GPU, and then sending them back to the CPU upon completion, complex calculations can be performed quickly in parallel. Parallel processors can be much more efficient when it

comes to computation and simulation because they may run many simultaneous tasks without any decrease in performance due to increased load. Any algorithm that may be parallelized will see great benefits in execution time when executed on a FPGA or GPU [85].

In general, FPGAs have less overhead than GPUs when communicating with the CPU. Additionally, a digitizer may directly load information onto the FPGA whereas typically, data must be transferred through computer memory to be accessed by a GPU. The lack of overhead makes an FPGA the product of choice for the purpose of TAUM imaging; however, either choice could perform the required processing.

FPGAs consist of billions of transistors that make up configurable logic blocks capable of complex mathematics, digital filtering, and high-speed synchronization. The FPGA logic blocks are interconnected by a programmable wiring mesh that allows complete reconfigurations of the signal routing. This design provides flexibility for a variety of applications and reconfigurable programming based on application needs. Figure 4 depicts an example of a how a desired function might be implemented within the wiring mesh of a FPGA.

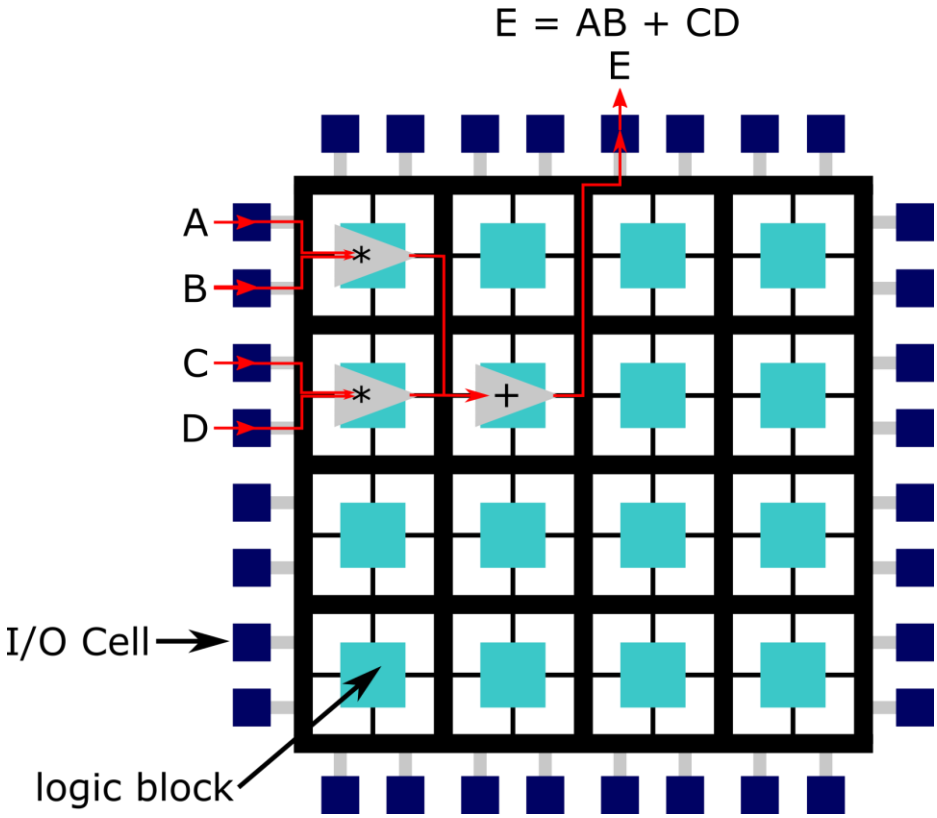

Figure 4. Schematic depicting a possible data configuration for routing a function through a FPGA. The function is implemented by routing the input from the I/O cells to their appropriate logic blocks.

FPGAs have found use in many different imaging applications including fluorescence lifetime imaging [86], optical coherence tomography [87], confocal microscopy [88], MRI [89], and ultrasound imaging [90]. Any imaging system that has sufficient imaging processing or strict synchronization requirements can benefit from the parallel nature of FPGAs and GPUs. As is detailed in Appendix B, TAUM requires a significant amount of processing, including a large array fast Fourier transform, which makes the technology an excellent candidate for utilization of the FPGA.

CHAPTER II

REAL-TIME DEMODULATION OF PHOTOACOUSTIC SIGNALS[*]

Implementation of Photoacoustic Post Processing on a Field Programmable Gate Array

This section of Chapter II introduces post-processing algorithms for optical resolution photoacoustic microscopy (PAM) and describes the implementation of one algorithm on a field programmable gate array for real-time implementation. This implementation forms the foundation of the future processing applications on the FPGA. Characterization of this system is detailed as well.

Introduction

PAM is a hybrid imaging modality which exploits the photoacoustic effect to provide optical absorption contrast via ultrasonic detection. Through the photoacoustic effect, pulsed optical excitation is absorbed by a chromophore causing local thermoelastic expansion. This localized expansion propagates through the sample as a stress wave, and the wave can be detected with an ultrasonic transducer [32]. PAM can provide optical diffraction limited lateral resolution and ultrasonic limited axial resolution [51]. In tissue, ultrasonic radiation is attenuated three orders of magnitude less than visible radiation,

[*] Part of this chapter was reprinted with permission from "Continuous real-time photoacoustic demodulation via field programmable gate array for dynamic imaging of zebrafish cardiac cycle" by S. P. Mattison, R. L. Shelton, R. T. Maxson, and B. E. Applegate, 2013. *Biomedical Optics Express*, 4, 8, 1451–1463. Copyright 2013 OSA.

enabling PAM to image biological structures deeper than other high resolution optical imaging modalities [36]. The capability of PAM to collect an entire axial line (a-line) per laser pulse enables the capture of volumetric frames without the need for scanning of the axial direction. The high speed of PAM allows for capturing of volumetric datasets of dynamic biological processes *in vivo*. As such, real time PAM has previously been demonstrated in biological tissues [48], [91], [92].

PAM has been demonstrated as an effective tool for imaging both exogenous and endogenous chromophores. It has been employed to image microvasculature, melanoma tumors, and cell mitochondria through endogenous chromophores such as hemoglobin [93], melanin [94], and cytochrome C [83]. In a clinical setting, these chromophores can potentially aid in tumor margining and characterization of port-wine stains [95]. Additionally, these endogenous contrast agents aid in the research of tumor angiogenesis, hemodynamics, and imaging of cellular mitochondria. Furthermore, through exogenous contrast agents including methylene blue, rhodamine 6G, and gold nanoparticles, PAM has been used as a research and diagnostic tool for a variety of applications [96], [97].

In most PAM systems, the optical excitation and acoustic pathways are arranged in one of three co-axial designs. A reflection mode co-axial design allows for optimal geometry between the excitation and detection pathways to maximize axial resolution in thick tissue samples. However, reflection mode co-axial PAM systems require technically complex custom optical/acoustic beam combiners to allow for the excitation and detection pathways to be combined [49]. Alternatively, a transmission mode co-axial design uses an ultrasonic transducer opposing an optical objective to remove the need for a custom beam

combiner; however, this approach is not feasible for thick tissue samples or for most *in vivo* applications. A third approach for performing co-axial PAM utilizes dark field optical imaging to direct the beam around the ultrasonic transducer to the sample. This setup again requires bulky custom optics to direct the excitation beam to the sample. Alternatively, optical methods can be used to detect pressure waves using phase sensitive interferometry and Fabry-Perot interferometry [98]. Optical detection suffers from drawbacks in the form of decreased sensitivity to acoustic waves or the requirement of direct contact with the sample. Previously, off-axis PAM (OA-PAM) which allows for confocal alignment of the excitation and detection pathways in reflection geometry, has been demonstrated to allow for photoacoustic imaging without the need for custom optics. OA-PAM enables the use of commercially available microscope objectives and ultrasonic transducers at the cost of a mild reduction in axial resolution.

Real-time photoacoustic microscopy has previously been demonstrated through the scanning of the excitation beam through galvanometers, microelectromechanical mirrors, and voice coils [91], [92]. These systems allow for collection of an entire volume of data in real time; however, data storage and processing act as a bottleneck between data acquisition and display. Shi et al. [99] demonstrated real-time capture of volumetric datasets through the use of PCI data acquisition cards. This work overcame the data collection limitation typically associated with PAM, enabling collection of large PAM datasets in real-time. However, little work has been done to enable high speed data processing required to obtain morphologically accurate images from the raw pressure profiles collected by ultrasound transducers. Since the PAM signal is oscillating in time,

the morphological information of the axial dimension is distorted by the bi-polar nature of the signal. Other imaging techniques, including magnetic resonance imaging and ultrasound imaging, collect bi-polar signals; however, these techniques employ demodulation and signal enveloping to process the bi-polar signal into morphologically accurate information [100]. Conversely, PAM images are typically published as maximum amplitude projection (MAP) images or processed through Weiner deconvolution [101]. While useful in many scenarios, MAP images take the highest intensity pixel in depth, thereby removing axial information from the image. Conversely, Wiener deconvolution corrects the bi-polar PAM signal for accurate morphological display of the axial dimension; however, it is an iterative process, and, consequentially, time consuming.

Hilbert transform enveloping (HT) and quadrature demodulation enveloping (QD) are both common methods for enveloping a bi-polar signal. QD computes an envelope of the signal by mixing a periodic signal of interest with in-phase and out-of-phase reference signals of the same frequency, and then utilizes a low pass filter to extract the output signal. HT combines the original signal with its Hilbert transform to build an analytical signal. The magnitude of the analytical signal is then computed to extract a time domain envelope of the bi-polar signal [102]. HT has a notable advantage in its lack of need for any prior knowledge of the frequency content of the a-line.

The Hilbert transform of a signal s(t) can be described mathematically as the convolution of a signal with a shaping function. Practically, there are two methods for performing a Hilbert transform of a signal. The first method involves taking a Fourier transform of the signal, then phase shifting the signal by multiplying the positive

frequencies of the Fourier spectrum by –j and the negative frequencies by j. The inverse Fourier transform is then taken to complete the Hilbert transform. A signal envelope may be constructed using the Hilbert transform by taking the square root of the sum of the squares of the original signal and the quadrature of the Hilbert transform of the original signal as shown in Equation 5 where p(t) denotes the original photoacoustic signal, H{} denotes the Hilbert transform, and P(t) denotes the enveloped photoacoustic signal. The second method for performing a Hilbert transforms is through convolution of the raw photoacoustic signal with a Hilbert filter in the time domain. Mathematically, these two methods are equivalent as convolution in the time domain is multiplication in the Fourier domain. Quite recently, GPU processing for the implementation of Fourier domain Hilbert transform for photoacoustic microscopy was demonstrated to provide real time photoacoustic processing [62].

$$P(t) = \sqrt{p(t)^2 + jH\{p(t)\}^2} \tag{5}$$

For QD to display an accurate signal, the reference signals must be matched to the center of the input signal's frequency spectrum. QD benefits from low processing overhead since all of the signal manipulation can be performed in the time domain, while HT requires two Fourier transforms, adding a significant amount of processing overhead. HT and QD processing were run in MatLab on a raw photoacoustic dataset of a Syrian Hamster Cheek pouch (Figure 5-A). Both QD processing (Figure 5-B) and HT processing (Figure 5-C) resulted in a morphologically accurate representation of the time domain transducer response; however, due to the low pass filter, QD results in a smooth profile

whereas the HT generates a signal envelope with minor ripples throughout the peak. QD was chosen to be implemented due to its smoother profile and lower processing overhead.

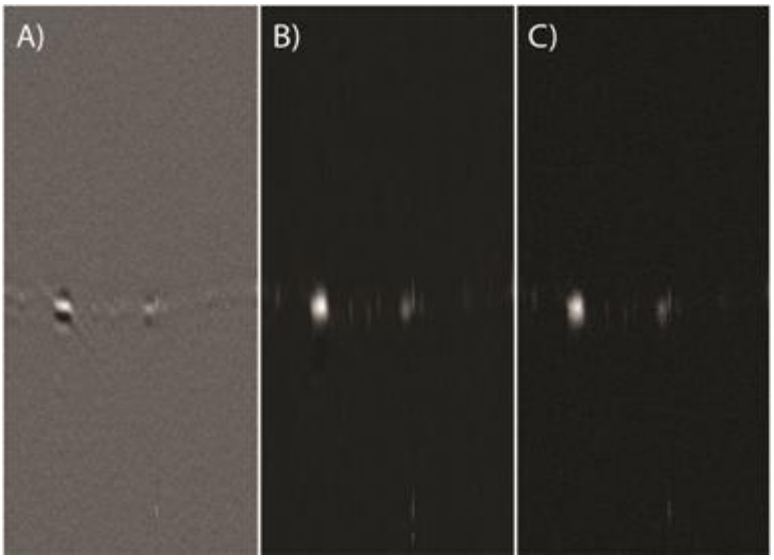

Figure 5. Photoacoustic b-scans of a Syrian hamster cheek pouch. (A) Photoacoustic b-scan of a Syrian hamster cheek pouch with no post processing. (B) B-scan of a hamster cheek pouch processed using QD. (C) B-scan of a hamster check pouch processed using HT. Reproduced with permission from [46]. Copyright 2013 OSA.

To illustrate these techniques, consider a signal, $p_s(t) = A_s sin(\omega t + \phi_s)$, which will represent the center frequency component of a photoacoustic A-line. In reality, the A-line is a broadband signal composed of many sine waves; however, for simplicity, a single frequency will suffice. Combining this signal with a reference signal of equal frequency, $p_R(t) = A_R \sin(\omega t + \phi_R)$ $p_R(t) = A_R(\omega t + \phi_R)$, yields Equation 6 below. In this case, p_m is the resulting signal from the mixing of the signal of interest and the reference signal, A_s

and A_R are the signal amplitudes of the photoacoustic signal and reference signal, ω is the signal frequency, and ϕ_s is the signal phase.

$$p_m = \frac{1}{2}A_s A_R \cos(\phi_R - \phi_S) + \frac{1}{2}A_s A_R \sin(2\omega t + \phi_R + \phi_S) \quad (3)$$

Equation 6 shows the frequency components at DC and 2ω that arise when the photoacoustic signal is mixed with the reference signal. The phase of both the photoacoustic signal and the reference signal must be known. The signal may be mixed with a reference signal with a ninety-degree phase shift to remove the dependence upon the signal phase. Taking the product of the two reference signals and the original signal will yield the signal shown in Equation 7.

$$p_{m1} = \frac{1}{2}A_s A_R \cos(\phi_R - \phi_S) + \frac{1}{2}A_s A_R \sin(2\omega t + \phi_R + \phi_S) \quad (7)$$

$$p_{m2} = \frac{1}{2}A_s A_R \cos\left(\phi_R - \phi_S - \frac{\pi}{2}\right) + \frac{1}{2}A_s A_R \sin(2\omega t + \phi_R + \phi_S - \frac{\pi}{2})$$

The mixed signals which represent the in-phase and out-of-phase components of the signal are then low pass filtered around the baseband signal component. The bandwidth and cutoff frequency of the filter are determined by the frequency content of the ultrasonic transducer. The magnitude, p_{mag}, of the resulting filtered signals is then taken by computing the square root of the sum of the squares as shown in Equation 8, effectively yielding a phase independent envelope of the photoacoustic A-line.

$$p_{MAG} = \sqrt{{p_{M1}}^2 + {p_{m2}}^2} \quad (8)$$

Field programmable gate arrays (FPGA) and graphic process units (GPU) were identified as potential hardware options for performing QD. Both FPGAs and GPUs are typically used in computing for accelerating complex calculations by offloading data from

the central processing unit (CPU), performing the calculations in parallel on the FPGA or GPU, then sending it back upon completion [85]. In general, FPGAs have less overhead than GPUs when communicating with the CPU. For the purpose of continuous PAM imaging, unexpected latency when communicating the PAM signal could lead to data loss. Therefore, a FPGA was chosen to perform enveloping of the PAM signal.

FPGAs are reconfigurable chips with interconnected logic gates. An FPGA has low overhead and determinism similar to an application-specific integrated circuit but with much more flexibility. The functionality of the FPGA can be defined by using software to configure the FPGA gates. The ability to reconfigure the FPGA through software is useful when performing QD since a different set of reference signals and a low-pass filter are required for each transducer used. Due to the architecture of the FPGA, many algorithms can be parallelized; making it an ideal tool for many biomedical applications [103]–[105]. By utilizing the parallel nature of the FPGA, the time taken to perform QD can be greatly reduced.

Materials and Methods

Figure 6-A depicts the off-axis orientation of the optical detection and ultrasonic detection. Figure 6-B and Figure 6-C depict the optical setup of the PAM system. A 26 MHz focused ultrasound transducer (PI50-2 Panametrics-NDT, 1.5 inch focal length) with 100 percent -6 dB bandwidth was fixed at a 50° angle relative to the optical axis. A Q-switched frequency doubled Nd:YVO4 laser (Advanced Optical Technologies – YVO-100Qsp) operating at 532 nm was used for optical excitation in this system. Laser pulses (0.7 ns pulse duration, 100 kHz repetition rate) were sent through an x-y galvanometer

pair (Cambridge 6210H) into a set of lenses used to image the scanning of the galvanometer onto the objective. Two different interchangeable objectives (Nikon Fluor 10Xw and Thorlabs AC254-75) were used to obtain a lateral resolution of either 30 μm or 40 μm, respectively.

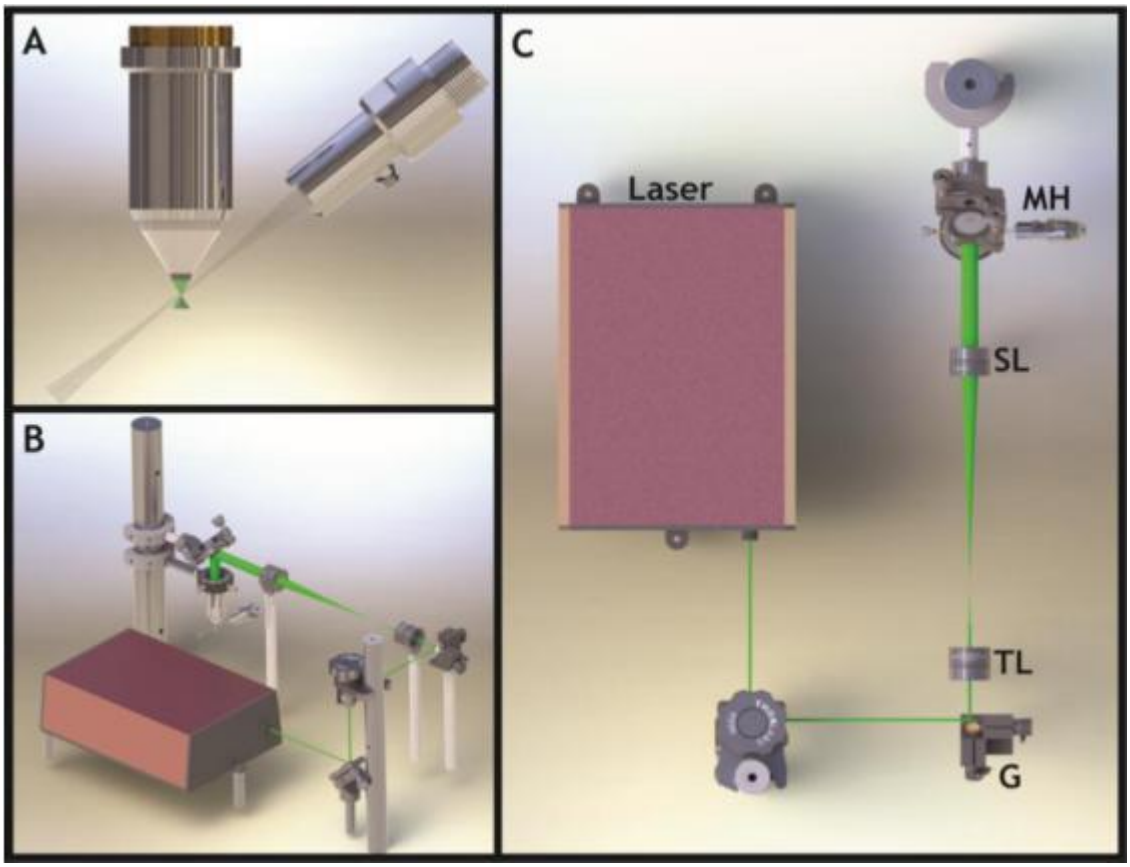

Figure 6. Schematic of the off-axis photoacoustic microscope. (A) Off-axis setup of the objective and ultrasound transducer. (B) Isometric view of the off axis PAM system. (C) Schematic of PAM system. G is an x-y galvanometer scanning pair, TL and SL are the tube and scan lenses respectively. MH is the microscope head consisting of the objective and ultrasound transducer as shown in A. Reproduced with permission from [46]. Copyright 2013 OSA.

The acquired signal was sent through a preamplifier (Mitex AU-1579-11575), low pass filtered at 70 MHz (Mini-circuits SLP-70+), then underwent second stage amplification (Mini-circuits ZFL-500LN+) for a total amplification of 51 dB. The signal was then converted from analog to digital via an 80 MHz digitizer (National Instruments 5732) and processed via FPGA (National Instruments 7965R).

For QD, the demodulated output signal, PA, comes from multiplying the input signal by a sine wave of frequency ω, equal to the center frequency of the transducer. Separately, the input signal is also multiplied by a cosine wave of frequency ω. Frequency mixing with the sine and cosine results in the shifting of the original signal to baseband and 2ω. While this could be accomplished with just one reference signal, using both sine and cosine removes sensitivity to phase variations. The results are then sent through a low pass filter with a pass band dependent upon the transducer bandwidth. Finally, the square root of the sum of the squares is performed to provide the enveloped signal. Since the result of QD has a magnitude of half of the magnitude of the input signal, the result is multiplied by two to provide an accurate envelope.

While requiring less computing power than HT, QD is still a computationally intensive process with significant data processing required to perform the low pass filter. A distinct benefit of the FPGA is the ability to pipeline data processing. Pipelining allows complex calculations requiring multiple clock cycles to be parallelized for increased efficiency. Using parallel processing, these steps can be performed simultaneously on multiple data points. To illustrate the benefit of data pipelining, consider an algorithm that would typically take 100 clock cycles to process a single pixel. Utilizing an FPGA with an 80

MHz clock, processing a 1000 by 1000 pixel image would take 1.25 seconds without pipelining. With data pipelining, this 100 clock cycles per pixel processing overhead is translated to an initial latency of 100 clock cycles followed by a pixel being output every clock cycle. Utilizing the same 80 MHz FPGA, the 1 megapixel data set takes only 0.0125 seconds to process, an improvement of 2 orders of magnitude.

An algorithm was developed to run on an 80 MHz FPGA (National Instruments 7965R) for performing QD on the PAM signal as it was collected. The low pass filter would typically act as a bottleneck in signal processing, taking 36 clock cycles of the FPGA to complete per pixel. At 80 MHz, this translates to a 450 ns delay per pixel. Through pipelining, this delay is translated into a 450 ns latency followed by constant throughput at 12.5 ns per pixel. Table 1 demonstrates the throughput of the system and the latency that occurs at each step. For a PAM system equipped with a 100 kHz laser, a 1000 by 1000 by 1000 pixel PAM dataset could be collected in 10 seconds. With data pipelining this image can be collected and processed in 10.575 seconds, demonstrating a processing overhead of less than 6% of the total time for acquisition and processing. Using the same clock rate, it would take 550.25 seconds to collect and process an identical dataset without pipelining. Figure 7 illustrates the flow of data for QD through the FPGA. The latency due to data processing could be removed from the system by implementing QD completely in hardware through signal mixers and analog filters. However, software-based QD provides flexibility for optimizing filters for multiple transducers.

Table 1: Steps for QD of raw photoacoustic signal. Reproduced with permission from [46]. Copyright 2013 OSA.

Processing Steps	Clock Cycles required	Latency (ns)
Read in of signal from digitizer	1	12.5
Mixing of signal with reference signals	0	0
Low Pass Filter	36	450
Squaring of Signals	0	0
Summing of Squares	0	0
Square root of sum	12	150
Transfer to output array	1	12.5

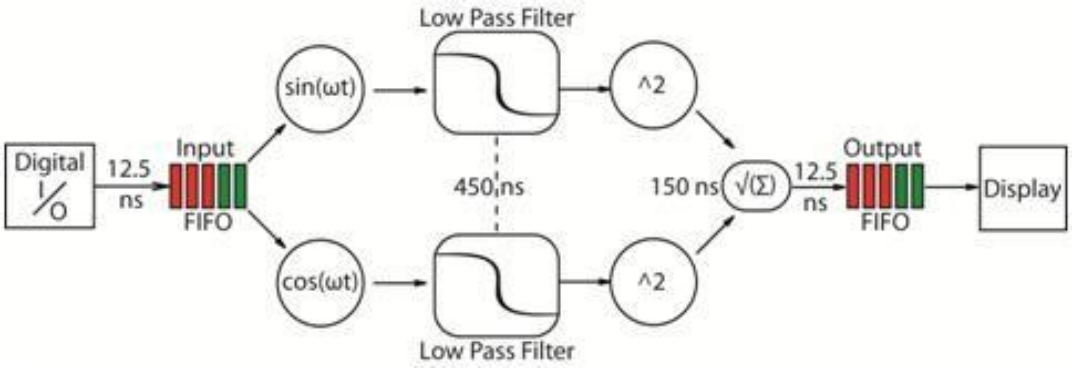

Figure 7. The flow of signal through the FPGA as the raw photoacoustic signal undergoes quadrature demodulation. Each clock cycle, a single data point is read in via a digitizer. The point is passed to a processing loop where it undergoes QD. Time points indicate latency for steps. Reproduced with permission from [46]. Copyright 2013 OSA.

System Evaluation

The theoretical axial resolution of an off-axis PAM system is the resolution axial resolution of a PAM system, as previously defined in Equation 4, projected onto the optical axis. This projection is defined by Equation 9 where V_s is the speed of sound in tissue, β is the bandwidth of the transducer, and θ is the angle of the transducer relative to the optical axis.

$$PSF_z \frac{0.88V_s}{\beta cos\theta} \quad (9)$$

The relationship between co-axial and off-axis PAM can be seen when θ is zero, Equation 9 simplified to Equation 4. In this off-axis PAM system, β equals 27 MHz and θ equals 50°; therefore, the theoretical axial resolution is 89.75 μm. In order to evaluate the axial resolution, a volumetric image (Figure 8-A) was taken of a small ink mark on a coverslip and rendered via Image J. Given the intrinsically thin nature of the ink mark, the resultant a-line will be the impulse response of the system, thus providing an approximation of the axial resolution [63]. An artifact due to the reflection of the acoustic signal through the coverslip is clearly seen in the b-scan of the data, displayed in Figure 8-B. A demodulated a-line, shown in Figure 8-C, taken from the ink mark was found to have a FWHM of approximately 90 μm. These results are in good agreement with the theoretical axial resolution. Additionally, by decreasing the angle between the ultrasonic transducer and the microscope objective, axial resolution may be recovered.

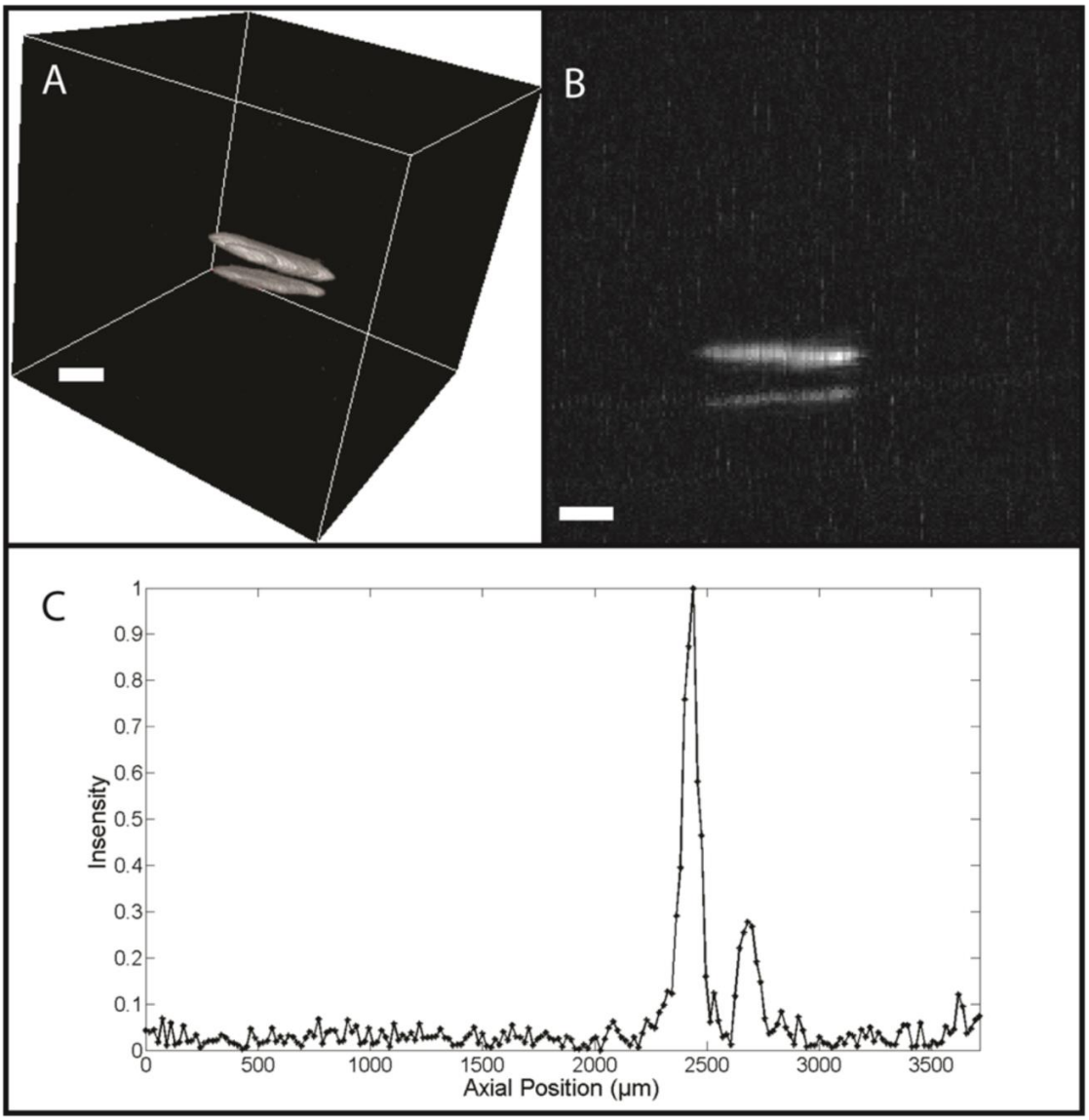

Figure 8. Characterization of Off-axis PAM resolution. (A) Volume of ink mark on the coverslip. (B) B-scan of ink mark taken from volume. Note the reflection of the PAM signal from the far side of the coverslip. (C) A-line of demodulated PAM signal, FWHM corresponds to axial resolution of the system. Scale bar is 100 μm. Reproduced with permission from [46]. Copyright 2013 OSA.

Using an unfocused transducer has previously been demonstrated as an effective method for accommodation of galvanometer scanning [106]. In place of an unfocused transducer, a focused transducer may be used to optimize the signal to noise ratio (SNR)

at the cost of field of view (FOV). By placing the sample in the near field of the focused transducer a larger field of view can be obtained with minimal reduction of SNR.

The transducer was translated along its focal axis such that the sample was located in the near field of the transducer focus. The loss of SNR with respect to the offset from the focus of the transducer was characterized using an ink sample. The corresponding increase in field of view was characterized using an air force resolution chart. SNR was calculated as twenty times the log base 10 of the peak signal strength to the standard deviation of the noise floor. Figure 9-A demonstrates the adjusted design of the off-axis setup. Moving farther into the near field of the transducer provided an increase in lateral FOV, shown in Figure 9-B. As expected, with the increase in lateral FOV came a reduction in SNR, shown in Figure 9-C. Signal fluctuations are known to occur in the near-field of a focused transducer and explain the noisy sinusoidal shape of the SNR. At the maximum field of view of 2.74 mm, the SNR was reduced by 1.15 dB from the focus of the transducer; however, this point corresponded with a peak in the near field fluctuations. Observing the SNR at a trough in the near field fluctuations, corresponded to a reduction in SNR by 3.85 dB with a field of view of only 2.4 mm; therefore it was important to maximize both field of view and SNR based on the near field fluctuations. Figure 9-D characterizes the loss of SNR with increasing FOV demonstrating the fluctuations in SNR with respect to FOV. If the optical excitation was moved too far in the near-field of the transducer, the detection path of the transducer would be obscured by the side of the objective, limiting further improvement in the FOV. Lateral and axial resolutions were not affected by utilizing the near field of the transducer.

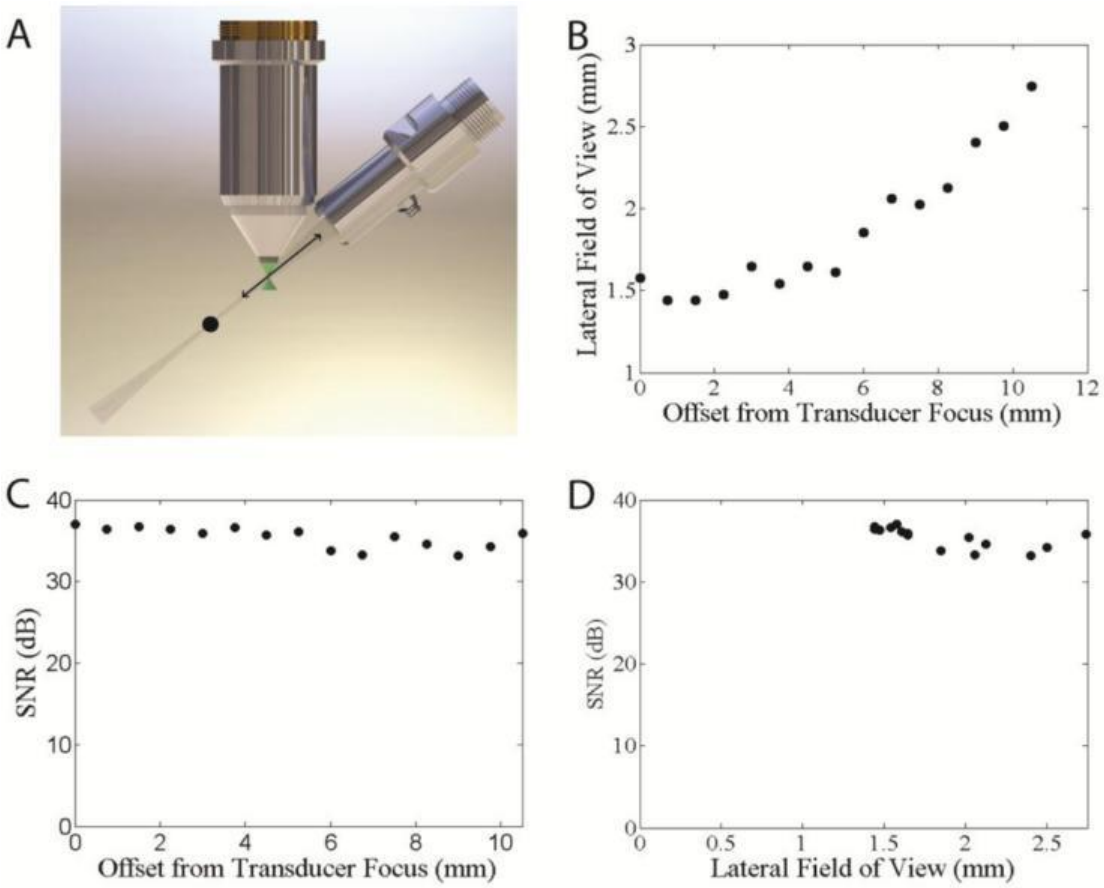

Figure 9. Characterization of SNR and FOV for off-axis PAM system. (A) Modified off-axis design of the objective and transducer. Black dot indicates focal spot of transducer. Arrows show the direction of transducer displacement. (B) Increase in field of view with respect to position in the near field of the transducer. (C) Loss of signal to noise ratio in dB with respect to position in the near field of the transducer. (D) Loss of signal to noise ratio in dB with respect to increased field of view. Reproduced with permission from [46]. Copyright 2013 OSA.

Moving into the near field of the transducer causes fluctuations in signal intensity in both the lateral and axial dimensions. In order to characterize the signal fluctuations caused by operating in the near field of the transducer, a piece of black tape was imaged as a uniform absorber. The SNR of the photoacoustic signal was monitored as a function of distance from the transducer. Figure 10-A demonstrates the 5.1 dB variance of the

lateral signal to noise ratio across the -6dB field of view of the transducer. Similarly, the signal strength in the axial dimension was characterized by imaging an ink mark on paper and observing the SNR of the photoacoustic signal as the axial position of the ink mark was adjusted. Likewise, Figure 10-B characterizes the 0.4297 dB variance of the axial signal to noise ratio across the -6dB depth of focus. These near field fluctuations of the PAM signal can limit the effectiveness of quantitative analysis of photoacoustic signals. Additionally, in the near field, the near field fluctuations across the entire field of view can reduce image quality. Near field fluctuations can be processed out through normalization of captured data to the near field of the transducer.

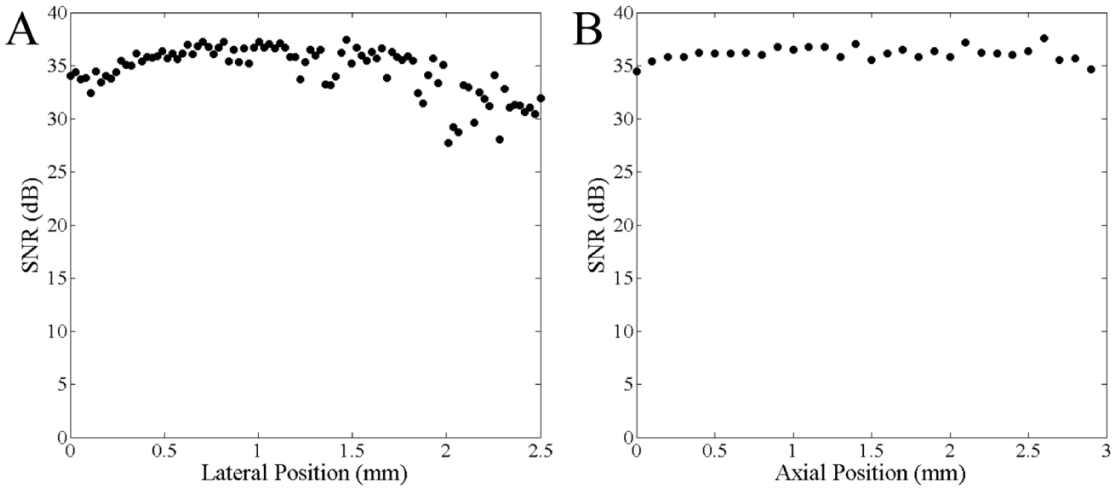

Figure 10. Characterization of the near field fluctuations of 25 MHz focused ultrasound transducer for (A) the lateral dimension and (B) the axial dimension. Transducer sensitivity is characterized by the measured SNR. Reproduced with permission from [46]. Copyright 2013 OSA.

Finally, to fully evaluate the potential for high speed PAM applications, the FPGA was setup to run at its maximum sampling frequency of 80 MHz and transfer demodulated

data to the computer via first in first out array. With 80 pixels per a-line, a 200 by 200 by 80 pixel volume was simulated and the program ran without issue. This translates to a line rate of 1 MHz. A data transfer rate of 800 MB/s between the FPGA and the host computer enables continuous transfer of full b-scans through block memory of the FPGA. Currently this limitation lies solely on the speed of the digitizer being used. With a faster digitizer, greater line rates could be achieved; however, current hardware limitations between the FGPA and the host computer would eventually cap the maximum data throughput.

Conclusion

The previous prototype of an off-axis PAM system was improved through the implementation of galvanometer scanning. Additionally, continuous collection and display of morphologically accurate PAM images has been enabled through the implementation of QD of a PAM signal via FPGA. Currently, the limiting factor of the PAM system is the repetition rate of the laser. Using simulated data, the capability of the FPGA to handle laser repetition rates up to 1 MHz has been confirmed. By eliminating the delay between image capture and display, FPGA technology can further enable research applications of PAM.

Acquisition of Real-time Photoacoustic Images

This section of Chapter II details a real-time application for photoacoustic microscopy. The cardiac cycle of a zebrafish embryo is captured in real-time b-scans. A method for stitching together periodic events is also presented and utilized to generate a 4-dimensional scan of the zebrafish embryo cardiac cycle.

Introduction

Photoacoustic microscopy (PAM) is a hybrid imaging modality which exploits the photoacoustic effect to provide optical absorption contrast via ultrasonic detection. PAM can provide optical diffraction limited lateral resolution and ultrasonic limited axial resolution [51]. The capability of PAM to collect an entire axial line (a-line) per laser pulse enables the capture of volumetric frames without the need for scanning of the axial direction. The high speed of PAM allows for capturing of volumetric datasets of dynamic biological processes *in vivo*.

As photoacoustic signals are bipolar, they must be post-processed to adequately reconstruct the true morphology of the sample. Bipolar signals are commonly found throughout the field of biomedical imaging. Both ultrasound imaging and magnetic resonance imaging (MRI) collect bipolar and use them to produce morphological images. These techniques typically use the concept of demodulation and signal enveloping to adequately display the morphological information. Utilizing the FPGA based quadrature demodulation algorithm described in the previous section, real-time images were captured of the dynamic heartbeat of a zebrafish embryo.

Materials and Methods

Figure 6-A in the previous section depicts the off-axis orientation of the optical detection and ultrasonic detection. Figure 6-B and Figure 6-C from the previous section depict the optical setup of the PAM system. A 26 MHz focused ultrasound transducer (PI50-2 Panametrics-NDT, 1.5 inch focal length) with 100 percent -6 dB bandwidth was fixed at a 50° angle relative to the optical axis. A Q-switched frequency doubled Nd:YVO4 laser (Advanced Optical Technologies – YVO-100Qsp) operating at 532 nm was used for optical excitation in this system. Laser pulses (0.7 ns pulse duration, 100 kHz repetition rate) were sent through an x-y galvanometer pair (Cambridge 6210H) into a set of lenses used to image the scanning of the galvanometer onto the objective. A custom made objective (Thorlabs AC254-75) was used to obtain a lateral resolution of either 30 μm or 40 μm, respectively.

Since imaging of the zebrafish embryo only utilized 1 mm of the available 2.5 mm field of view, signal generation could be localized to a region with minimal near field fluctuations, removing the need for signal normalization.

Embryos were treated with 1-phenyl 2-thiourea during development to block the formation of melanin [107]. Prior to imaging, the zebrafish embryo was anesthetized using 0.0175% Tricaine and embedded in a 1% agarose solution to restrict movement.

Results and Discussion

To dynamically image the heart of a zebrafish embryo, demodulated b-scan sequences were captured in time across a 1 mm region of the zebrafish heart. Each frame in a sequence consisted of 200 a-lines captured at a line rate of 25 kHz. Each frame took 8 ms

to capture followed by a galvanometer fly back of 0.8 ms for an effective frame rate of 113 Hz. Each sequence consisted of 200 b-scans for a total capture time of 1.76 seconds. Figure 11 shows 3 frames from a sequence of demodulated b-scans. Demodulation was performed in parallel to data acquisition via FPGA, no additional post-processing was performed. A total of 31 b-sequences were captured in 5 µm increments across the zebrafish heart. The result was a collection of 31, 200 by 200 by 200 pixel datasets of the beating zebrafish embryo heart. The collection of sequences was then assembled into a four-dimensional dataset via post-acquisition synchronization. Post-acquisition synchronization utilizes periodic events in a collection of videos to generate a time sequence of volumetric datasets [108]. In addition to post-acquisition synchronization, the image was resampled 4 to 1 in the axial dimension to achieve symmetrical voxels. Figure 12 shows 16 volumetric images from a rendered 4-dimensional dataset of the beating of a developing zebrafish embryo.

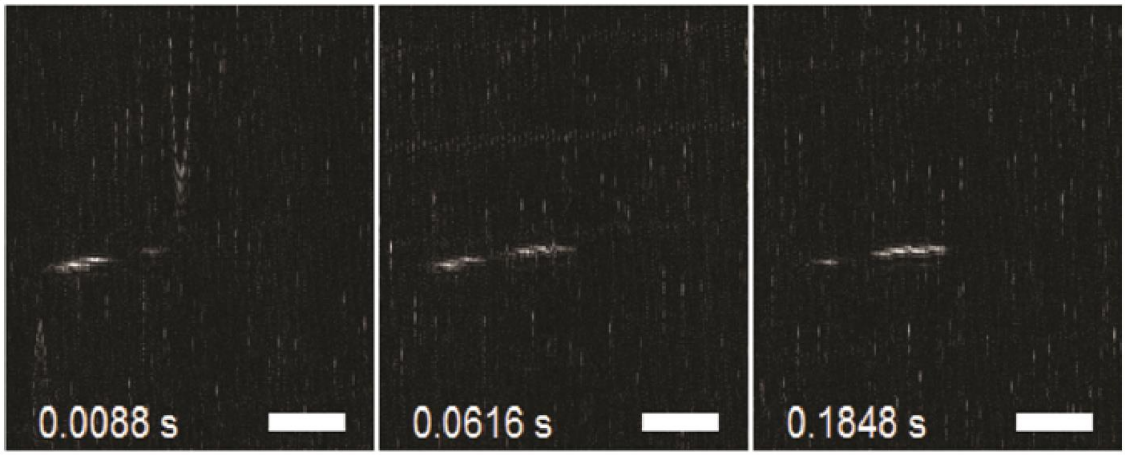

Figure 11. Frames of demodulated b-scans capturing dynamic images of zebrafish embryo heart using the OA-PAM system. Diastole and systole of both chambers are shown. Lateral scale bar is 100 μm. Reproduced with permission from [46]. Copyright 2013 OSA.

A zebrafish embryo 48-72 hours post fertilization has a documented heart rate of 147 beats per minute [109]. To capture a 200 by 31 by 200 pixel volume sampled at the Nyquist frequency would require a laser repetition rate of 75.02 kHz. Due to power limitations of the laser itself, the system was limited to a maximum repetition rate of 25 kHz in biological samples. Thus, it proved necessary to use post-acquisition synchronization to capture an appropriately sampled volume of the beating zebrafish heart. Each frame was generated using ImageJ 3d-Viewer.

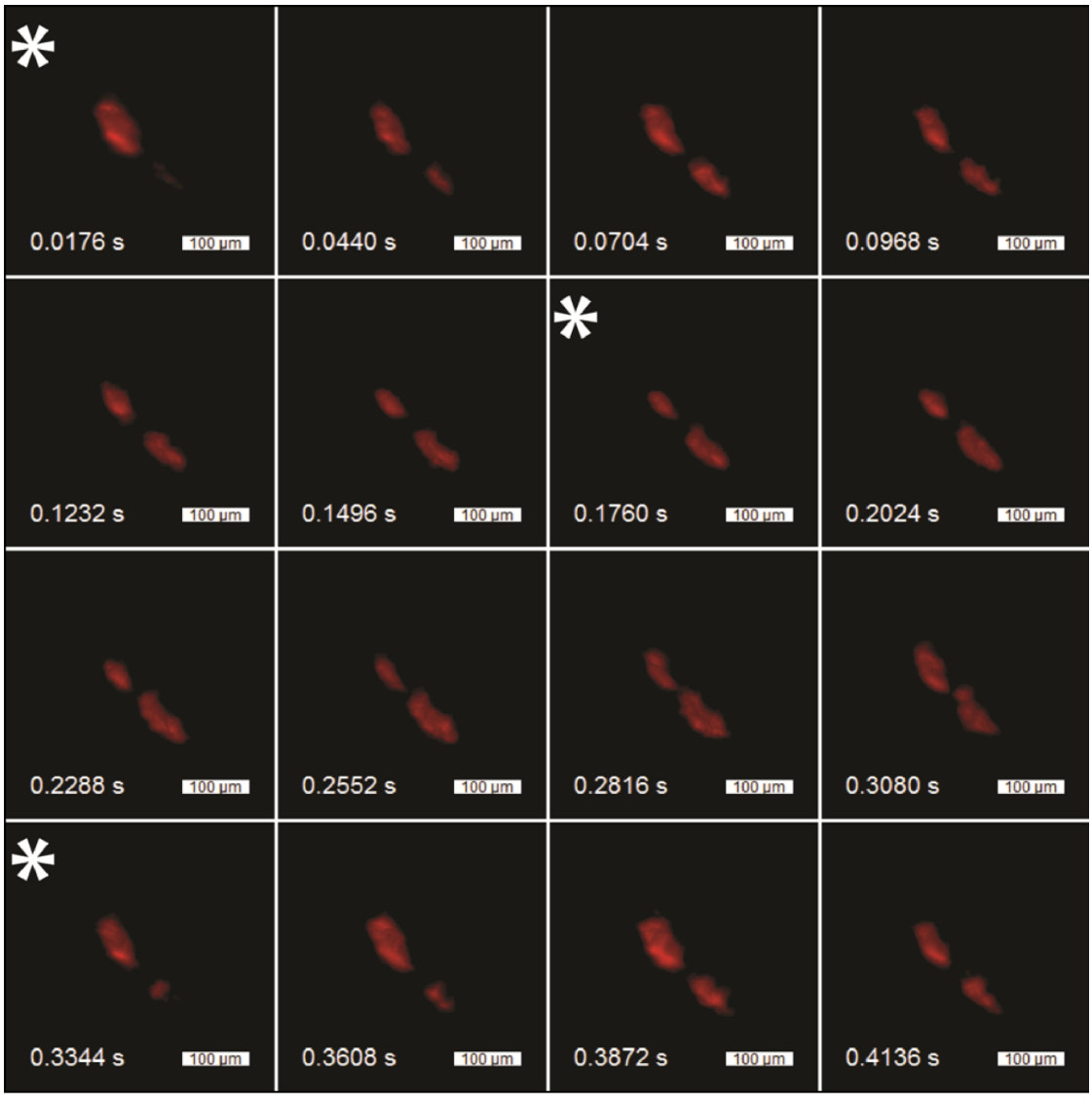

Figure 12. Three dimensional volumes taken from a four-dimensional dataset of a zebrafish heart. In order to show the progression of a single heartbeat, the figure shows every third volume from the dataset of a single cardiac cycle. Chamber 1, on the left, starts in diastole while Chamber 2, on the right, is in systole. As the heartbeat progresses, chamber 2 relaxes while chamber 1 begins to contract. At 0.1760 seconds, chamber 1 is in systole while chamber 2 is in diastole. The heartbeat finishes at 0.3344s as chamber 1 returns to diastole. Key frames are marked by an asterisk for clarity. Reproduced with permission from [46]. Copyright 2013 OSA.

The zebrafish embryo has a two-chambered heart that pumps asynchronously. Figure 12 illustrates the asynchronous pumping of the two heart chambers so that when one

chamber is in diastole, the other is in systole. Following the image from left to right, top to bottom, it can be seen that the left chamber starts in diastole, while the right chamber is in systole. As the beat progresses, the left chamber contracts into systole while the right chamber relaxes into diastole. Finally, to complete the cycle, the left chamber relaxes back into diastole and the right chamber returns to systole. At 48 – 72 hours post fertilization, the heart of a zebrafish appears as a U-shaped tube. In Figure 12, both chambers are shown, with the region connecting the two chambers lying outside of the imaging plane.

Conclusion

The high speed images capabilities of the PAM system were established by capturing a four-dimensional dataset of the beating heart of a zebrafish embryo. This implies that by utilizing a higher repetition rate laser, 4-dimensional images of dynamic processes could be captured without the need for post-acquisition synchronization.

CHAPTER III

HIGH RESOLUTION MOLECULAR IMAGING VIA NON-LINEAR PHOTOACOUSTIC MICROSCOPY[*]

Optimization of Transient Absorption Ultrasonic Microscopy Processing on a Field Programmable Gate Array

The first section of chapter III outlines the implementation of the processing for transient absorption ultrasonic microscopy onto a field programmable gate array. This processing removes the needs for post-processing of the data and reduces the size of datasets by four orders of magnitude. The higher speed afforded by real-time processing also enables volumetric TAUM imaging.

Introduction

Photoacoustic microscopy (PAM) is an absorption contrast imaging technique that has seen rapid growth in recent years. PAM harnesses the photoacoustic effect, in which pulsed optical excitation induces molecular vibrations in a chromophore, leading to rapid thermoelastic expansion and the emission of a pressure wave. The pressure wave can then

---

[*] Part of this chapter was modified with permission from "Volumetric imaging of erythrocytes using label-free multiphoton photoacoustic microscopy" by R. L. Shelton, S. P. Mattison, and B. E. Applegate, 2014. Journal of Biophotonics, 7, 10, 834-840, Copyright 2014 Wiley-VCH Verlag GmbH & Co. KGaA. Reproduced with permission.

[*] Part of this chapter was reprinted with permission from "Simplified method for ultra high-resolution photoacoustic microscopy via transient absorption" by S. P. Mattison, and B. E. Applegate, 2014. Optics Lettesr, 39, 15, 4474-4477, Copyright 2014 OSA.

be detected using an ultrasound transducer, providing depth information about the chromophore through the time-of-flight measurements of the recorded ultrasound signal. One of the primary benefits of photoacoustic imaging is the energy conversion from light to sound (pressure) that takes place in the chromophore after absorption. Due to its much longer wavelength, ultrasonic radiation is attenuated three orders of magnitude less than visible light radiation in tissue [47]. This allows photoacoustic microscopy to image much deeper than other optical microscopic techniques. There has been significant interest in recent years in trying to improve the resolution of PAM. The vast majority of these efforts have focused on improving the transverse resolution through tighter optical focusing [51], [52], [110] down to the optical diffraction limit; however, far less effort has been put forth to improve upon the axial resolution of PAM. Multiphoton techniques such as two-photon absorption leading to photoacoustic emission have been reported [111]; however, the signal from this type of non-resonant process results in very weak photoacoustic emission.

The primary reason for the lack of ultrahigh axial resolution photoacoustic microscopes is due to the parameters that govern the axial resolution in PAM. The point spread function of PAM is limited by the ultrasound transducer bandwidth in the axial dimension and the focusing of the excitation light in the lateral dimension. Resolutions on the order of one wavelength of light can be achieved in the transverse dimension [49]; however, the axial resolution is still limited to 10s of microns. The resulting asymmetric point spread function is the primary reason most PAM images are published as maximum amplitude projection (MAP) images, with most of the depth information thrown away. This problem of asymmetry prompted the development of a method to obtain wholly

optically resolved point spread function. The result was a preliminary demonstration of transient absorption ultrasonic microscopy (TAUM) [53].

Transient absorption (TA) is a resonant multi-photon process often used in spectroscopy to characterize chromophores by measuring molecule-specific physical properties. TA measurements employ a pump pulse and a probe pulse, separated in time by an interpulse delay. The pump pulse is absorbed by the molecule, populating one or more excited electronic states. The probe pulse immediately follows, interrogating the ground state population, which changes as electronic relaxation occurs. By observing the change in signal of the probe with the pump present and absent, information about the electron dynamics of the molecule may be directly measured. Through this technique, two important molecular signatures may be obtained: transient absorption spectrum and ground state recovery time. When used in an imaging configuration, as is the case in TAUM, TA introduces improved optical depth sectioning equivalent to that in two-photon excited fluorescence and confocal microscopy. This is due to the fact that TA is a two-photon process and the signal is a product of the pump and probe pulse power, resulting in an intensity-squared dependence. These concepts are discussed in detail in the section *Simplification of Transient Absorption Ultrasonic Microscopy* in Chapter III.

TAUM merges photoacoustic microscopy and transient absorption techniques by introducing a pump excitation beam to a photoacoustic microscope. Two pulses delayed from each other in time are absorbed by the sample, leading to separate, but temporally overlapping photoacoustic emission. Through frequency encoding of the excitation light, the signal arising from the transient absorption process is extracted and the light is raster

scanned on the sample to build up an image. TAUM is particularly well-suited for ultrahigh resolution photoacoustic imaging. Unlike the two-photon absorption PAM technique mentioned previously, transient absorption is a resonant process, resulting in much stronger photoacoustic signal. Furthermore, TAUM is implemented with a low frequency, low bandwidth, 5 MHz ultrasound transducer, which minimizes ultrasonic attenuation in tissue and provides higher sensitivity than techniques which use high frequency ultrasound transducers.

A prototype TAUM system was previously built to demonstrate the improved axial sectioning of TAUM. However, due to the hardware used and the extensive post-processing that was required, TAUM was only feasible as a 2D imaging system. For this reason, a more sophisticated TAUM system was designed to improve the imaging speed. By moving to a higher repetition rate laser, and replacing stage scanning with galvanometer scanning, the imaging speed of TAUM was greatly improved. Unfortunately, to extract the TAUM signal from the raw photoacoustic signal, extensive post processing is required. For each TAUM pixel, 128 raw photoacoustic A-lines must be acquired and concatenated into a single array. Next, a fast Fourier transform must be applied to convert the photoacoustic signal to the frequency domain. Finally, the signal that arises due to the sum and difference of the pump and probe frequencies must be extracted and summed. This processing was the largest bottleneck of the prototype system. In order to overcome this bottleneck, all of the processing for the TAUM signal extraction was implemented on a field programmable gate array (FPGA).

FPGAs are reconfigurable chips with interconnected logic gates. An FPGA has low overhead and determinism similar to an application-specific integrated circuit but with much more flexibility. The functionality of the FPGA can be defined by using software to configure the FPGA gates. Due to the architecture of the FPGA, many algorithms can be parallelized; making it an ideal tool for many biomedical applications [86], [88], [89], [112]. By utilizing the parallel nature of the FPGA, the time taken to perform TAUM can be greatly reduced.

Methods and Materials

Figure 13-A and Figure 13-B respectively show the isometric and top-down views of the system schematic. A frequency doubled Nd:YVO_4 (Advanced Optical Technologies, Inc.) laser operating at 532 nm was used as the source. The output of the laser is split by a 50/50 beam splitter, forming the pump and probe beams. The pump beam passes through the beam splitter, while the probe beam is reflected into a short (~1 ns) optical delay arm. Another 50/50 beam splitter then recombines these beams after they are amplitude modulated at separate frequencies using a dual frequency optical chopper. The beams are frequency encoded so their contributions can later be extracted using Fourier domain analysis. The recombined beams are then sent through a galvanometer scanning mirror pair and a telecentric lens system with a magnification of 3x before being focused through a 0.8 NA water immersion objective lens (Nikon Fluor 40X) onto the sample.

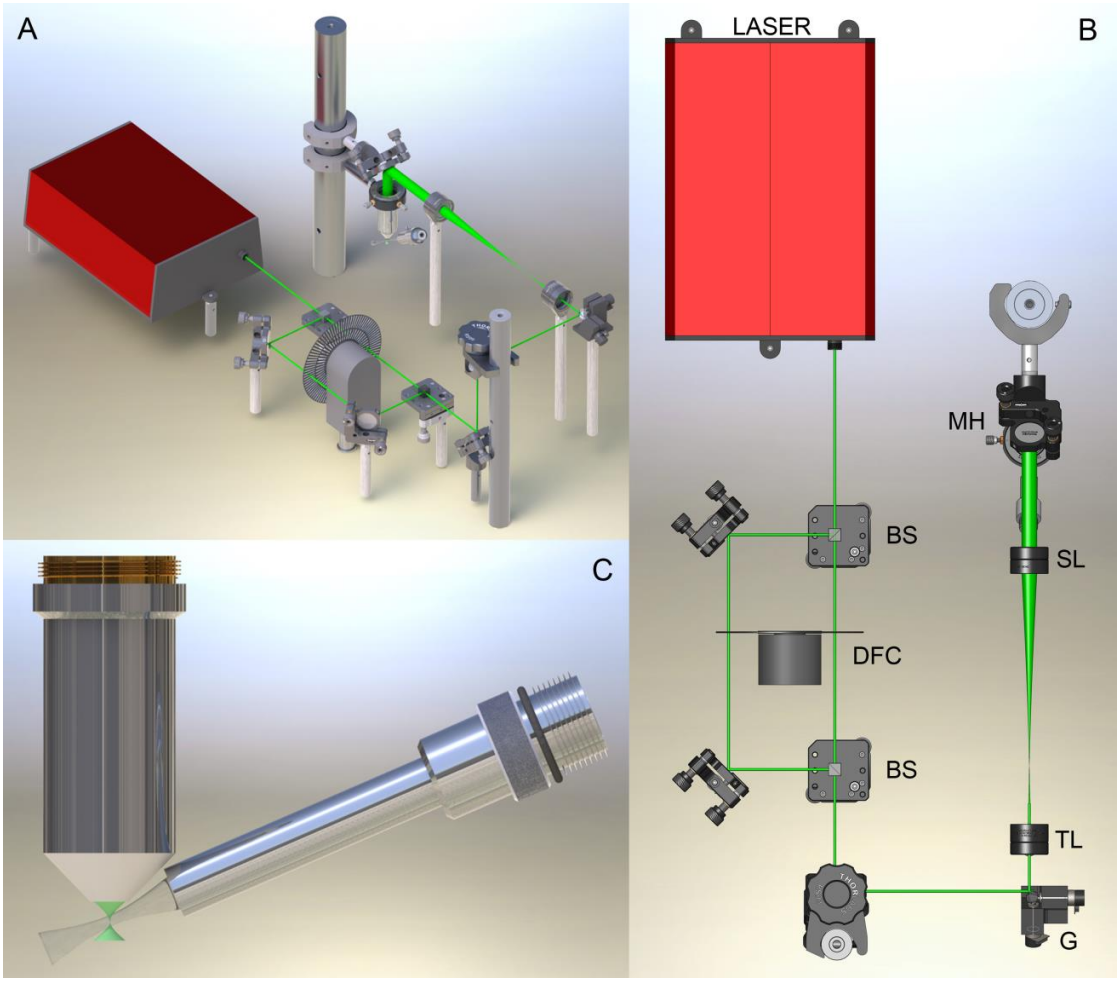

Figure 13. Schematic of the TAUM system. (A) Isometric view of the TAUM microscope. (B) Top-down view of the microscope with components labeled. BS: 50/50 Beam splitter, DFC: Dual-frequency optical chopper, G: Galvanometer scanning mirror pair, SL: Scan lens, TL: Tube lens, MH: Microscope head. (C) Close-up rendering of the off-axis detection scheme used in the microscope head. Modified with permission from [113]. Copyright 2014 Wiley-VCH Verlag GmbH & Co. KGaA

The frequency encoded photoacoustic emission is collected using a 5 MHz immersion ultrasound transducer (NA = 0.23) in off-axis detection geometry as described and shown in Figure 13-C. The imaging beam is scanned inside the focal spot of the transducer, so no mechanical scanning of the transducer is needed. For depth scanning of the sample a

motorized stage (Newport Corp.) is used. The transducer signal is amplified by two RF amplifiers and then routed to the input of an 80 MHz digitizer front-end adapter module (NI 5732, National Instruments, Inc.) connected to a field programmable gate array (FPGA) FlexRIO board (PXIe-7965R, National Instruments, Inc.) for processing.

The pump and probe light pulses are separated by only 1 ns, yet the temporal response of a 5 MHz transducer is ~ 200 ns, so the resulting photoacoustic signals are temporally overlapped. Consequently, the TAUM signal must be extracted from the frequency domain at the frequencies dictated by the dual frequency optical chopper. In order to achieve sufficient spectral resolution, a number of photoacoustic A-lines are consecutively collected at a single location and Fourier analysis is performed on the larger window of multiple photoacoustic A-lines. For the studies described in this manuscript, 128 A-lines were used for each Fourier analysis. The optical chopping frequencies introduce sidebands to the frequency domain photoacoustic signal. Each sideband corresponding to transient absorption signal is then collected and integrated over the bandwidth of the ultrasonic transducer, producing one pixel in the resulting TAUM image.

The algorithm required to extract the TAUM signal carries a lot of computational overhead, owing largely to the large array Fourier transform that must be computed. For this reason, it was important to design the system on hardware that is optimized for this type of resource-intensive processing. A field programmable gate array (FPGA) was chosen because it is designed to optimize speed of processing algorithms that can be parallelized, such as the fast Fourier transform (FFT). Using the FlexRIO hardware platform available from National Instruments, the collected photoacoustic signal could be

digitized directly to the FPGA, minimizing signal transfer times between acquisition and processing. One of the primary benefits of a FPGA over other advanced processing hardware architectures, such as a graphics processing unit (GPU) is that a FPGA can pipeline data input directly acquire data from a digitizer. This allows processing to start on the first data point, as the second data point is being acquired.

Once acquired, a point-by-point FFT was performed on the incoming data. After the FFT, each point was sent to an accumulator, which operated based on a previously loaded binary mask, which gave TRUE values to the enable terminal of the accumulator at each frequency bin corresponding to one of the transient absorption sideband frequencies. The output of the accumulator was then a single value corresponding to the integrated TAUM signal across the bandwidth of the transducer.

Due to the nature of the FFT algorithm utilized, the FFT is first processed in bit-reversed order on the FPGA then the results are re-ordered into natural order. The concept of bit reversed order is illustrated in Figure 14. Due to memory and speed limitations, the FPGA could not keep up with performing the natural re-ordering of the FFT. Instead, the FFT was output in bit-reversed order and the binary mask was loaded into memory in bit-reversed order. Additionally, by outputting the results of the FFT in bit-reversed order, additional memory was utilized to enable windowing of the data prior to FFT.

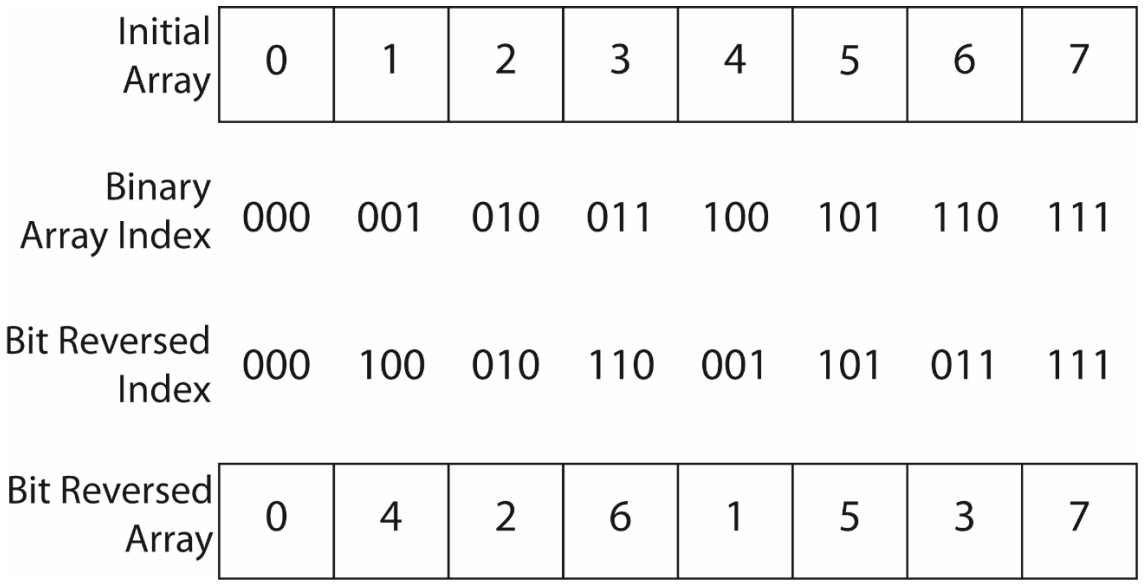

Figure 14. Illustration of bit reversal using a 3-bit array index. Note that the results of bit reversal depend upon the bit-depth of the array indices.

Results and Discussion

Most of the improvements incorporated into the new TAUM system were designed to provide increases in imaging speed. Initial implementation of TAUM with natural order output from the FFT allowed for pixel rates of 10 Hz, 100 times faster than the prototype TAUM system. Further optimization of the FPGA code to enable TAUM processing using bit-reversed results from the FFT allowed for pixel rates up to 800 Hz, a speed limited only by the repetition rate of the laser. This not only made two-dimensional imaging much more robust, but allowed for volumetric imaging.

A volumetric rendering of several erythrocytes is shown in Figure 15-A. Erythrocytes in a fresh blood smear were imaged. The blood smear was prepared using whole bovine blood and fixed to a glass slide with 95% methanol. A pulse energy of 5 nJ was used for

both the pump and probe pulses, resulting in 10 nJ of incident pulse energy on the sample at a pulse repetition rate of 50 kHz.

The images were sampled in 1 μm steps in the X and Y (*en face*) dimensions and 0.5 μm steps in the Z (depth) dimension. The volume stack was resampled by a factor of two using linear interpolation to reduce aliasing. Figure 15-B shows a zoomed area of the volume depicting a single erythrocyte, in which the concavity of the erythrocyte is evident.

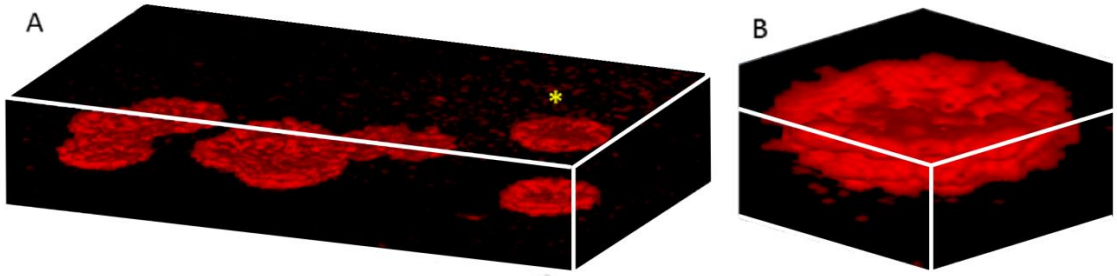

Figure 15. Volumetric rendering of red blood cells fixed on a slide imaged with TAUM. (A) 50x50x20 micron volume of several RBCs on a glass slide. (B) Volume of a single RBC marked with a yellow asterisk in (A). Reproduced with permission from [113]. Copyright 2014 Wiley-VCH Verlag GmbH & Co. KGaA.

Although the imaging speed of this second generation TAUM system has been greatly improved over past implementations, it is still a relatively slow technique when compared to other nonlinear microscopy techniques, such as two-photon excited fluorescence and confocal microscopy. The speed could be increased as a linear function of laser repetition rate, ushering in great returns as q-switched laser technology advances to higher repetition rates. Additionally, lowering the number of pulses used for each pixel can increase imaging speed. Currently, 128 pulses are used per pixel, but 64 pulses per pixel have also

been used with success. As in many imaging techniques, there is an obvious trade-off between speed and SNR.

Conclusion

In conclusion, transient absorption ultrasonic microscopy (TAUM), a high-resolution, label-free, molecular imaging technique has been demonstrated for subcellular photoacoustic microscopy in all dimensions. Increases in imaging speed of up to three orders of magnitude have been demonstrated over the initial TAUM prototype while reducing pulse energies by over one order of magnitude. These optimizations enabled three-dimensional volumetric imaging of single red blood cells, demonstrating axial resolution of 1.5 μm. This is the first time a volume of fully resolved RBCs has been captured using photoacoustic microscopy.

Simplification of Transient Absorption Ultrasonic Microscopy

This section of the text describes the methods and theory behind simplifying the optical design of a standard TAUM system making it applicable to any current PAM system. The relevant theories are outlined as well as methods and results for the work.

Introduction

Photoacoustic Microscopy (PAM) is a hybrid imaging modality that combines optical absorption contrast with ultrasonic detection to obtain the benefits of molecular imaging with the advantage of detecting sound waves. In tissue, the typical frequencies used for ultrasonic imaging are attenuated three orders of magnitude less than visible light [36].

The molecular contrast afforded by photoacoustic microscopy is ideal for mapping the location of strong endogenous absorbers including hemoglobin, melanin, and cytochromes [83].

The depth penetration benefit provided by converting optical energy to acoustic energy has enabled the development of several PAM techniques with varying resolution and penetration depth [49]. A major limitation, of current high-resolution PAM techniques, is the generation of highly asymmetric voxels. Using traditional approaches, subcellular transverse resolution imaging has previously been demonstrated; however, due to properties of the ultrasonic transducer, the axial resolution is typically limited to tens of microns. This limitation largely restricts high-resolution PAM imaging to samples of only a single cell layer. Images of thicker samples would be degraded due to averaging within the voxel.

By integrating pump-probe spectroscopy with PAM, it is possible to optically confine the point spread function in the axial dimension. This technique, termed transient absorption ultrasonic microscopy (TAUM), was demonstrated by fully resolved volumetric images of erythrocytes. A key challenge to utilizing TAUM for photoacoustic imaging was the necessity of a sensitive alignment of pump and probe beam pathways to maximize overlap. In this section, a TAUM system which removes the need for separate pump and probe pathways is proposed and demonstrated. This enables the capture of optically resolved images in three dimensions through the addition of amplitude modulation in the beam path of a typical high-resolution PAM system.

The underlying physical process responsible for TAUM is transient absorption (TA). It is typically measured with pump-probe absorption spectroscopy and commonly used to characterize molecular dynamics. Nominally a molecule is excited with a pump and a probe pulse, separated in time by an interpulse delay. The pump pulse drives a molecule from its ground state to some excited state. This process transiently alters the absorption coefficient. The transient change can be measured by recording the absorption of the probe with the pump both on and off. The difference between the two is then the transient absorption signal. Typically the pump is modulated at some frequency. The depth of modulation transferred to the probe is then the transient absorption signal.

Considering the weak field limit where Beer's law holds, the fluence of the probe after passing through some absorber with length, *l,* and absorption coefficient, μ_a, is $F_{pr} = F_{pr,0}e^{-\mu_a t}$. In the limit of weak absorption, the exponential function may be approximated by the first two terms of its Taylor series expansion. In this limit a cosinusoidal modulation of a pump beam will lead to cosinusoidal modulation of μ_a. The probe intensity is then defined by Equation 10.

$$F_{pr} = F_{pr,0}[1 - \left(\mu_a + \frac{\Delta\mu_a}{2} + \frac{\Delta\mu_a}{2}\cos(\omega_{pu}t)\right) l \tag{10}$$

Here ω_{pu} is the pump modulation frequency. $\Delta\mu_a$ is the transient change in absorption coefficient defined in Equation 11.

$$\Delta\mu_a = \sum_n \mu_{a,n}, e^{-t_d/\tau_n} - \mu_{a,bl} \sum_n e^{-t_d/\tau_n} \tag{11}$$

In this case, t_d is the interpulse delay between the pump and probe, $\mu_{a,n}$ is the effective absorption coefficient for the nth pathway back to the ground state with corresponding

decay time τ_n, and $\mu_{a,bl}$ is the bleaching of the ground state absorption due to the pump. $\Delta\mu_a$ is positive when interaction with the pump increases the absorption of the probe and negative when interaction with the pump decreases the absorption of the probe. The time varying part of Equation 10 is identified as the transient absorption as in Equation 12.

$$F_{pr} = F_{pr,0}\left(\frac{\Delta\mu_a}{2}\cos(\omega_{pu}t)\right)l \tag{12}$$

For reasons that will become apparent the probe intensity must also be modulated. Assuming a cosinusoidal modulation of the probe beam, Equation 12 becomes Equation 13.

$$F_{pr} = F_{pr,0}\frac{\Delta\mu_a}{4}\cos\left((\omega_{pu} \pm \omega_{pr})t\right)l \tag{13}$$

In the context of a photoacoustic signal, some of the pathways described in Equation 8 rapidly decay on the order of picoseconds generating heat. The resulting pressure wave (photoacoustic emission) propagates out in all directions from the absorber and is ultimately detected by an ultrasound transducer. If the time delay (t_d) between the pump and probe is much larger, on the order of 1 ns, the photoacoustic pathways do not contribute directly to the transient absorption signal. In other words, the exponential function in Equation 10 approaches zero before the probe interacts with the absorber. However, these pathways are exclusively responsible for the photoacoustic emission which allows the measurement of a signal proportional to Equation 13. This can be understood by realizing that any molecule that is temporarily (transiently) moved by the pump into a state that cannot relax via a pathway that leads to photoacoustic emission is effectively "dark." When the probe arrives, those molecules in a "dark" state cannot contribute to the photoacoustic emission. In reality the transiently occupied states may be

more or less probable to decay via pathways that lead to photoacoustic emission giving rise to “bright” and “dim” states, respectively.

In this regime, both the pump and probe pulses generate a photoacoustic emission separated in time by t_d. Given the relatively low temporal resolution (on the order of 100 ns) of a typical ultrasound transducer, the signals due to the pump and probe will be strongly overlapped in time, rendering it very difficult to measure the transfer of the pump modulation onto the probe signal. The solution is to modulate both the pump and probe, and then any interaction appears at the sum and difference of the respective modulation frequencies, as in Equation 13.

The frequency content of the signal is shown graphically in Figure 16. The repetition rate of the laser acts as a carrier frequency, such that the signals from the pump, probe, and pump-probe interaction (transient absorption, Equation 12) appear as side-bands on the laser repetition frequency, ω_{rep}, and every harmonic, $n\omega_{rep}$, which falls in the bandwidth of the ultrasound transducer. The TAUM signal may then be extracted by masking out the pump-probe interaction signals and summing. In practice only ~ 200 ns after each laser trigger is digitized and then multiple triggered acquisitions are concatenated to build up the time sequence. As a result the carrier frequency appears at 625 kHz rather than the true laser repetition rate of 50 kHz.

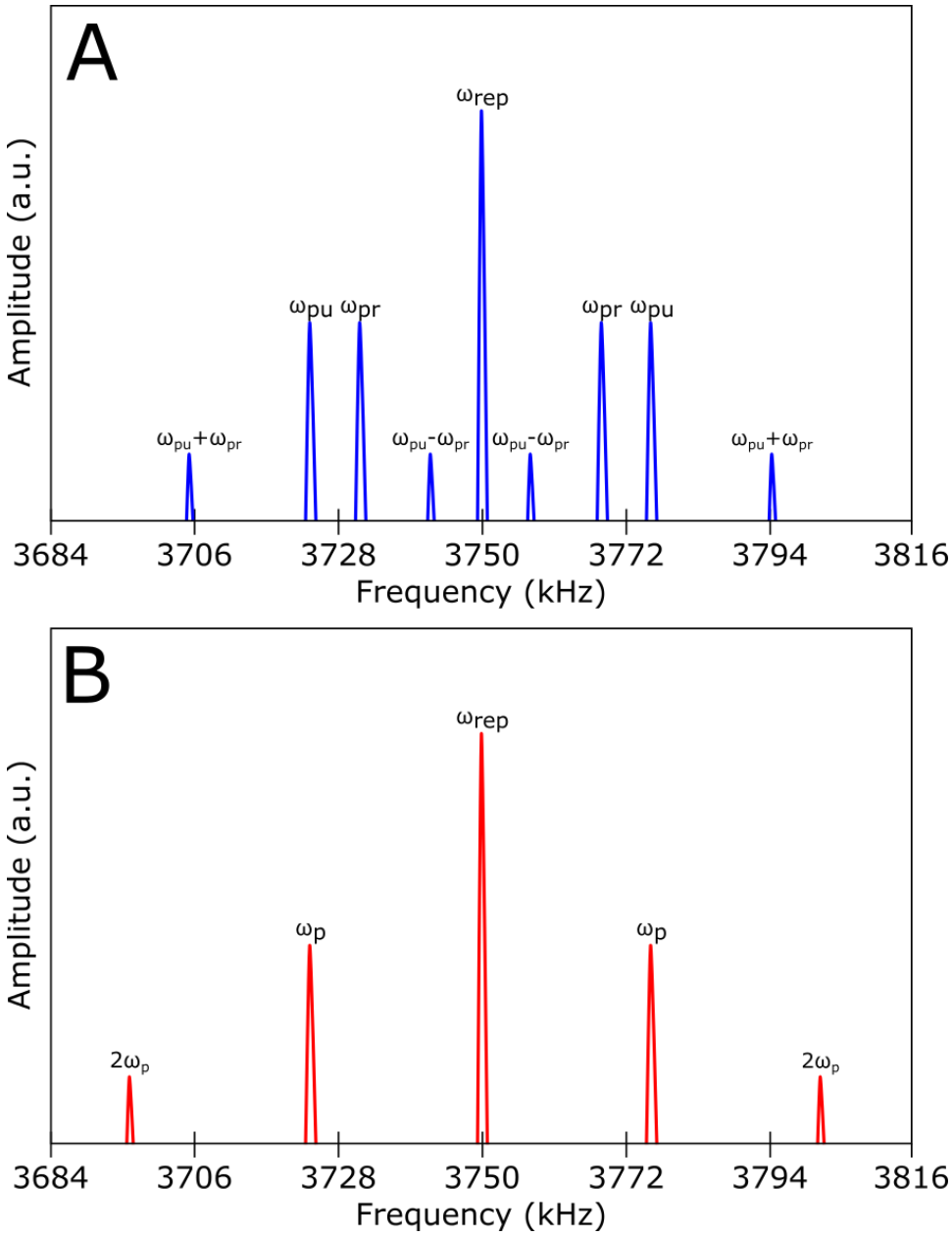

Figure 16. Frequency response of TAUM system when ω_{rep} is 50 kHz, ω_{pu} and ω_{p} are 2 kHz, and ω_{pr} is 1.42kHz. The modulation frequencies of the beam are shifted by the carrier frequency generated during digitization of discretely acquired photoacoustic signals. (A) Depicts the signal from TAUM using separate pump and probe pathways and modulation frequencies. (B) Depicts the frequency signal from TAUM using a single path with combined pump and probe. Modified with permission from [113]. Copyright 2014 OSA.

Utilizing this approach to TAUM, subcellular resolution photoacoustic microscopy has been demonstrated where the high axial resolution arises from the intensity squared dependence of the signal as in multiphoton microscopy. Likewise, it has been shown that it is feasible to exploit time resolved measurements where t_d is varied to differentiate closely related molecules like oxy and deoxy hemoglobin [54]. A key to the success of these experiments was careful overlap of the pump and probe beams which follow different beam paths as well as precise control of the interpulse delay, t_d. The fairly intricate optical and electronic setup necessary for these experiments is a potential impediment to wider adoption of this technology. However, if Equations 11 and 13 are reexamined and the case where t_d collapses to zero is considered and $\omega_{pu} = \omega_{pr} = \omega_p$, then Equations 11 and 13 simplify to Equations 14 and 15 as defined below.

$$\Delta\mu_a = \sum_n \mu_{a,n} - \mu_{a,bl} \tag{14}$$

$$F_{pr}(t) = -F_{pr,0}\frac{\Delta\mu_a}{4}\cos\left(2\omega_p t\right) l \tag{15}$$

Under these conditions $\Delta\mu_a$ is maximized and the transient absorption signal appears at the second harmonic of the amplitude modulation frequency, ω_p. Figure 16-A illustrates the frequency response of the original approach to TAUM and Figure 16-B depicts the frequency response of the new approach to TAUM. In the new approach half of the signal is pushed down to base band and is unrecoverable. However the corresponding reduction in the effective noise bandwidth mitigates any losses in the signal to noise ratio.

This fairly simple modification leads to wider separation in the frequency components, loosening requirements for signal bandwidth. More importantly, the complexity of the experimental setup is vastly reduced. Since the interpulse delay time is zero and the pump

and probe are modulated at the same frequency, there need not be separate beam paths. A single beam path with a single optical element for amplitude modulation will suffice.

The absence of a distinct pump and probe in a pump-probe type experiment may seem counterintuitive. One way to conceptualize the physical process is by considering a single laser pulse to be a packet of photons with some distribution in time. In this case, early arriving photons serve as the pump while late arriving photons serve as the probe.

Materials and Methods

The system shown schematically in Figure 17 was developed to investigate this approach to TAUM. A frequency doubled Nd:YVO_4 (Advanced Optical Technologies) laser operating at 532 nm was used for the source. This source was chosen due to its short pulse duration and ability to actively Q-switch up to 100 kHz. The output of the beam is directed into a galvanometer scanning mirror pair and a telecentric lens system with a magnification of 3 before being focused onto the sample through a 0.8 NA water immersion objective lens (CFI Apo 40XW NIR, Nikon, Inc.). The excitation beam is encoded with frequency ω_p by an optical chopper.

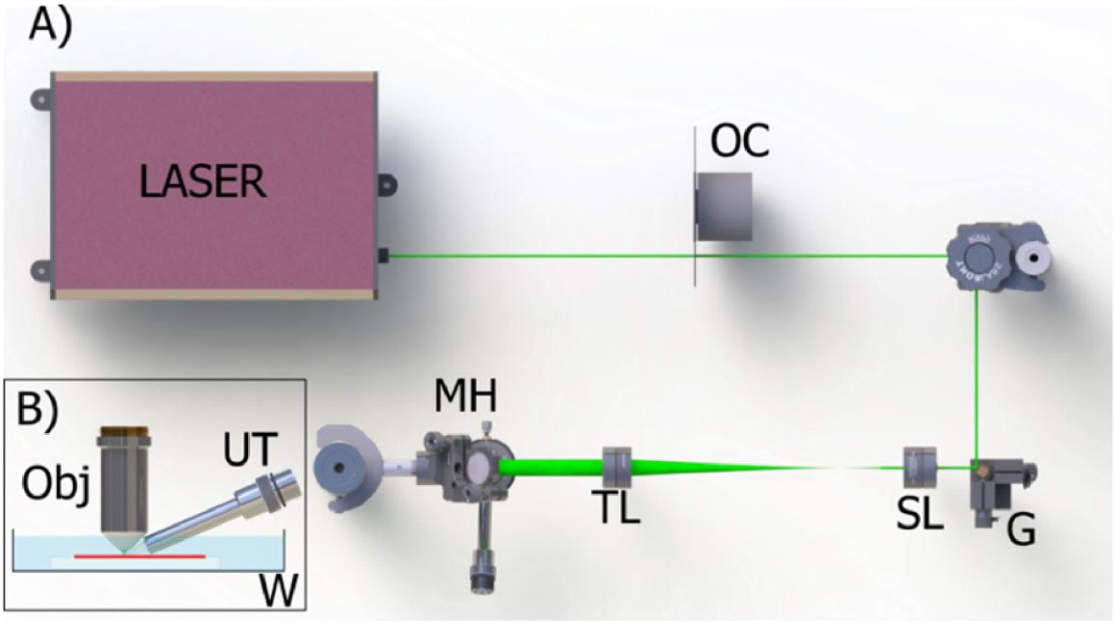

Figure 17. Schematic of the updated TAUM system where OC is an optical chopper, G is an x-y galvanometer scanning pair, SL and TL are a relay lens pair, MH is the microscope head, Obj is the objective, UT is an ultrasonic transducer, and W is a tank for water immersion of the transducer objective pair. (A) A top-down view of the system. (B) Inset view of the microscope head. Without the optical chopper, this is simply the schematic of an off-axis PAM system. Reproduced with permission from [113]. Copyright 2014 OSA.

Photoacoustic emission is collected using a 5 MHz water immersion transducer (NA = 0.23) in an off-axis detection geometry [64]. The transducer signal is amplified by two RF amplifiers and routed into the input of an 80 MHz digital front end adapter module (NI 5732, National Instruments, Inc.) connected to a field programmable gate array FlexRIO board (PXIe-7965R, National Instruments, Inc.) for processing.

It is important to carefully consider the power spectrum of the amplitude modulated beam. Any anhamonicity in the amplitude modulation that leads to signal at the second harmonic would generate unwanted background. A mechanical optical chopper provides a good approximation to a square wave. The square wave has the advantageous property

that its Fourier series only has odd harmonics. Modulation of a Gaussian shaped beam with a square wave leads to a power spectrum with only odd harmonics that are strongly dampened compared to the pure square wave. This behavior can be understood by realizing that this process can be modeled mathematically as a convolution of a square wave with a Gaussian. In the frequency domain that is the product of the odd harmonic Fourier series of the square wave and the Gaussian shaped Fourier transform of the beam. Under these conditions the power at the second harmonic is exactly zero.

In practice, neither a perfect square wave modulation nor a perfect Gaussian beam profile are ever achievable. However, measurements show that at pulse energies lower than 400 nJ, the power at the second harmonic was indistinguishable from the noise. As the typical pulse energy used for TAUM was 10 nJ, background at the second harmonic was not a factor in the experiments.

In order to obtain sufficient spectral resolution to extract the TAUM signal in the frequency domain, a number of photoacoustic A-lines are collected consecutively at a single location. The A-lines are concatenated and then Fourier transformed via the fast Fourier transform to convert the signal to the frequency domain. The magnitude of the Fourier signal is multiplied with a binary mask to isolate the frequencies of interest and summed to generate each TAUM voxel. The current implementation of this system utilizes 128 pulses per voxel with a laser repetition rate of 50 kHz. This resulted in a voxel rate of 390 Hz. Faster voxel rates can be achieved by using higher laser repetition rates or fewer A-lines per voxel; however, the signal to noise ratio is proportional to the square root of the number of A-lines.

Results and Discussion

As a demonstration of the optical sectioning provided by the system, volumetric images of fixed erythrocytes were captured. A blood smear was prepared by fixing whole bovine blood to a glass slide using 95% methanol. The cross sectional image of erythrocytes in the blood smear in Figure 18-A demonstrates the depth sectioning of TAUM. This is further demonstrated by the axial line in Figure 18-B which has a full width at half maximum of 1 μm. The red line is a Gaussian fit to the experimental points and is comparable to what has previously been measured using TAUM. Figure 19-A and Figure 19-B are a volume renderings of erythrocytes on the coverslip. Figure 18 is sampled in 0.5 μm steps in the axial dimension while Figure 19 is sampled in 1 μm steps in the axial dimension. All of the images of erythrocytes are sampled in 0.4 μm steps in the lateral dimensions. Images were processed to remove amplitude noise arising from power fluctuations of the laser. This noise is prevalent in both fundamental photoacoustic and TAUM imaging with this laser system.

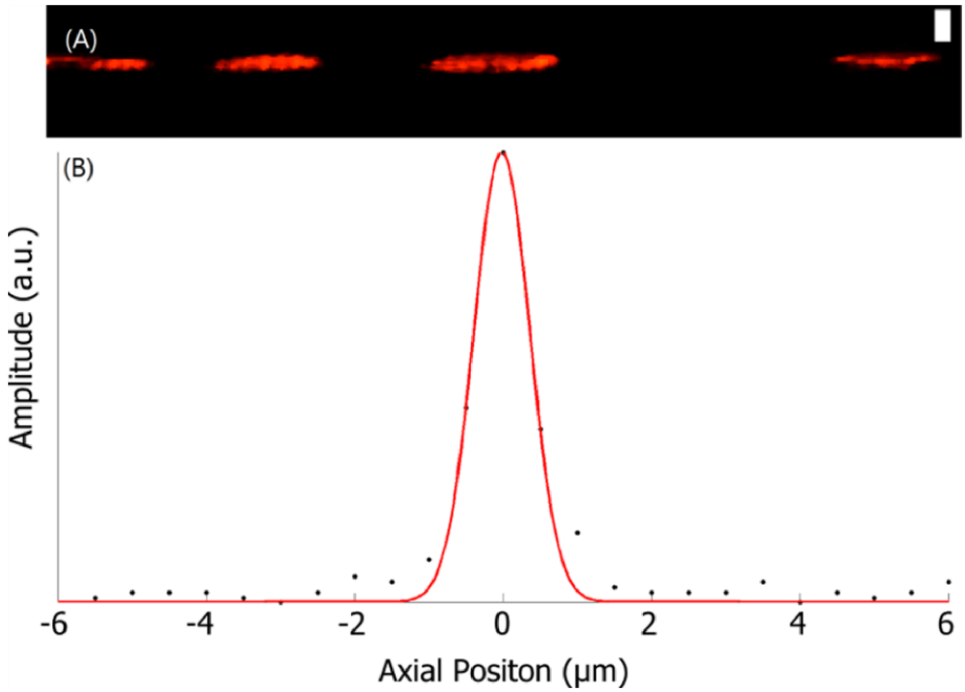

Figure 18. B-mode images of erythrocytes captured with simplified TAUM. (A) Axial scan through fixed erythrocytes on a coverslip captured using TAUM with a 5 MHz ultrasonic transducer. The left side of the figure shows two overlapping erythrocytes. The vertical scale bar is 10 um. (B) A single depth scan through the center of an erythrocyte, the red line is a Gaussian fit of the axial line (FWHM = 1 μm). Reproduced with permission from [113]. Copyright 2014 OSA.

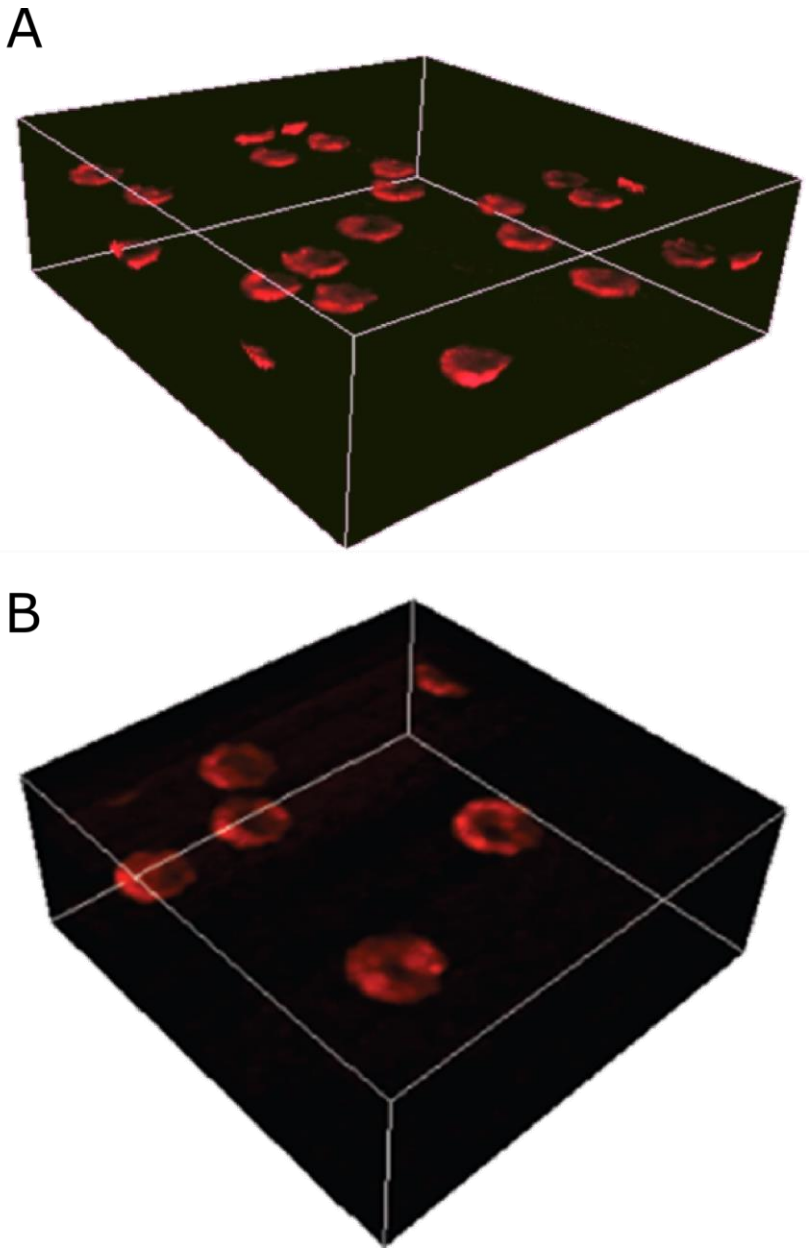

Figure 19. Volumetric renderings of erythrocytes (A) and (B) fixed on a coverslip captured using TAUM with a 5 MHz ultrasonic transducer. Field of view is 60 µm by 60 µm by 30 µm for both renderings. Modified with permission from [113]. Copyright 2014 OSA.

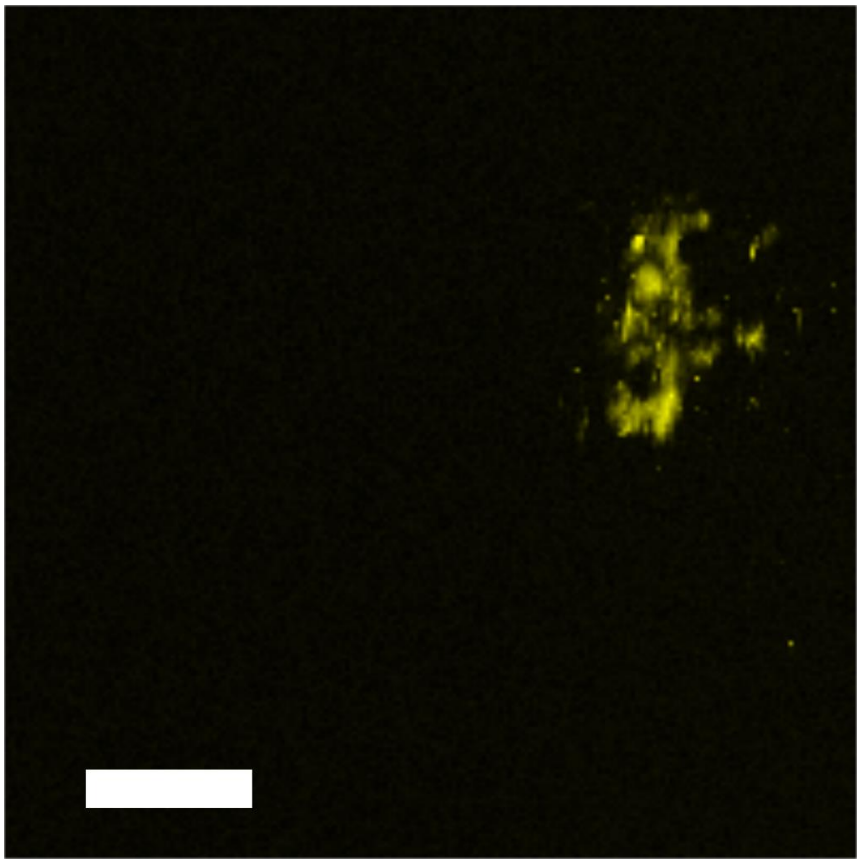

Figure 20. TAUM image of cytochromes within a fixed mouse smooth muscle cell. Based on microscope observations, the cell was undergoing apoptosis at the time of fixation. The scale bar is 20 µm.

To further demonstrate the imaging capabilities of this improved TAUM system, cytochromes indicating the presence of apoptosis were imaged in fixed mouse smooth muscle cells. Cytochromes are an important subset of hemeproteins found in high concentration in the mitochondria. They are not fluorescent, but they all bear the characteristic absorption spectrum of the hemeprotein with small shifts in the pair of bands in the 500-600 nm range depending on the particular cytochrome. For this experiment, the 40x objective was replaced with a 60x, 1.0 NA, (Nikon Fluor 60x) water immersion objective. Figure 20 depicts a TAUM image of the cytochromes in a fixed smooth muscle

cell that appeared to be undergoing apoptosis just prior to fixing. This is indicated in the TAUM image by the strong presence of cytochrome signals throughout the cell [114].

While the results demonstrate equivalent axial resolving power between two-beam TAUM and the new single beam TAUM setup, the simplified optical design comes at the cost of time resolution. Using a two-beam system, TAUM is capable of probing the time evolution of the pump-probe signal, effectively measuring the relaxation time of the excited states (τ_n in eq. 2). As has been shown previously, this property can be used to differentiate between related molecules such as oxy and deoxy hemoglobin [54]. By collapsing the interpulse delay to zero using a single pathway, time resolution is sacrificed in favor of the simplicity of the imaging system. Nevertheless, single-beam TAUM maintains the ability to achieve molecular specificity by using multiple excitation wavelengths. This is the typical approach used in photoacoustic microscopy [48].

Conclusion

A simplified technique for high-resolution photoacoustic microscopy was developed and tested. This approach enables high-resolution imaging in all dimensions and only requires the addition of amplitude modulation to a typical optical resolution PAM system. The axial sectioning is accomplished optically and is independent of the ultrasonic transducer. The axial sectioning of this approach to TAUM was demonstrated by fully resolving fixed bovine erythrocytes in all dimensions.

Hybrid Non-linear Photoacoustic and Confocal Microscope for Label Free Subcellular Imaging

This section of Chapter III details the combination of the simplified TAUM imaging system with a reflectance confocal microscope to acquire molecular absorption and scattering signals from biological samples. Relevant theory is discussed and direct comparisons are made between the resolution of the two imaging modalities on *ex vivo* and *ex vitro* biological samples.

Introduction

Over the past decade, photoacoustic microscopy (PAM) has established itself as a high-resolution imaging technique with excellent sensitivity to optical absorption [115]. PAM provides high lateral resolution, background free images of biological absorption with the improved imaging depth of ultrasonic detection. However, the axial resolution of PAM remains linked to the bandwidth of the ultrasonic detector, generating a highly asymmetrical point spread function [49]. Conversely, the point spread functions of most high resolution, optical imaging modalities, such as confocal microscopy [116] and two-photon fluorescence imaging [117], have highly symmetrical, optically resolved point spread functions. Thus, a hybrid PAM/confocal or two-photon fluorescence system would not provide complementary information in all dimensions.

Previously, a non-linear method for performing photoacoustic microscopy called transient absorption ultrasonic microscopy (TAUM) was demonstrated [53] to achieve optically resolved point spread functions. TAUM is achievable through transient absorption, a pump-probe absorption spectroscopy technique commonly used to

characterize molecular dynamics [59]. Nominally, TAUM is achieved by exciting a chromophore with a pump and a probe pulse, separated in time by an interpulse delay. In this scenario, the pump pulse drives the chromophore from its ground state to some excited state. This process transiently alters the absorption coefficient. The subsequent probe pulse interrogates the transient change in the absorption coefficient. By measuring the photoacoustic response due to the probe with the pump beam on and off, the transient absorption signal may be measured. Alternatively, by modulating the pump at some frequency and probe at a different frequency, the transient absorption signal may be extracted as the depth of modulation transferred from the pump to the probe.

As explained earlier in Chapter III, a simpler method exists to extract the transient absorption signal from a raw photoacoustic signal [113]. Instead of separate pump and probe paths, TAUM may be achieved using a single optical path which is modulated at a set frequency. This effectively sets the interpulse delay between the pump and the probe to zero and allows the TAUM signal to be extracted at the second harmonic of the modulation frequency. This system modification greatly simplifies the optical design of TAUM enabling any PAM microscope to be converted to a TAUM microscope with the addition of an optical modulator such as an acousto-optic modulator (AOM) or an optical chopper.

The ability of photoacoustic microscopy to provide high absorption contrast images is beneficial for many applications; however, photoacoustic microscopy is blind to cellular structures that do not present absorption at the excitation wavelength. Thus, there is a lack of context to the absorption signal in more complex tissues. This is evidenced in Figure

20 of the previous section, which clearly demonstrates the presence of a chromophore in the tissue; however, there is no indication of any cellular boundaries or reference points to provide context to the image. Fortunately, TAUM provides a point spread function identical to that of two photon absorption and confocal microscopy [53]. Furthermore, reflectance confocal microscopy and TAUM provide complimentary imaging contrast as TAUM provides exquisite absorption contrast [39] and reflectance confocal microscopy provides excellent scattering contrast [118]. A hybrid TAUM/confocal microscope capable of obtaining images of subcellular structures from a variety of tissue samples has been constructed. The confocal data adds much needed context to the relevant TAUM images.

Materials and Methods

Using the simplified TAUM architecture, a hybrid TAUM/confocal system was constructed into an upright Nikon microscope (Nikon Eclipse 80*i*). An isometric rendering of the system is shown in Figure 21-A and a labeled, top-down rendering is presented in Figure 21-B. A Q-switched frequency doubled Nd:YVO_4 laser (Crylas 1Q 532-2) operating at 10 KHz and 1.2 ns pulse duration was used as the light source for both the confocal and TAUM systems. The beam was directed through an optical chopper to provide the modulation frequency for TAUM signal collection. Following a polarized beamsplitter, the beam is circularly polarized by a quarter wave plate. Next, a pair of scanning galvanometers (Cambridge 6210H) then directs the beam through a scan lens focused on the back focal plane of the upright microscope. The Figure 21-C shows the optical schematic for the microscope head. The samples were excited using a 60x water

immersion objective (Nikon Fluor 60X) with a 1.0 numerical aperture. The raw photoacoustic signal is collected by a 6 MHz center frequency ultrasonic transducer with 100% bandwidth (Olympus NDT V310-SU) setup in an off-axis detection scheme. The backscattered light from the sample is collected by the 60x objective and directed back through the quarter waveplate to provide linear polarized light and the polarized beam splitter directs the scattered photons into the confocal detection arm. A pinhole lens focuses the in focus light into a 25 μm core multimode fiber (Thorlabs HPSC25). This fiber acts as a pinhole for the confocal system. The multimode fiber then directs the scattered photons into a fiber coupled avalanche photodiode (Hamamatsu C10508-01). Volumetric imaging is afforded using a vertical scanning microscope stage (Prior Scientific H101A). The system provides a convenient platform for imaging and enables simultaneous collection of morphological and absorption based images.

Raw photoacoustic signal is amplified using two 25 dB amplifiers (ZFL-500LNB+) and digitized using an 80 MHz digitizer (National Instruments 5732). For each TAUM pixel, 128 photoacoustic a-lines were collected and processed via fast Fourier transform on an in-line FPGA (National Instruments 7965R). The processed signal was then passed to the host computer and windowed to extract a raw TAUM pixel and a raw PAM pixel. Confocal data was collected on a second channel of the same 80 MHz digitizer. For each confocal pixel the signal from 128 pulses of the laser were collected on the FPGA and summed on the host computer.

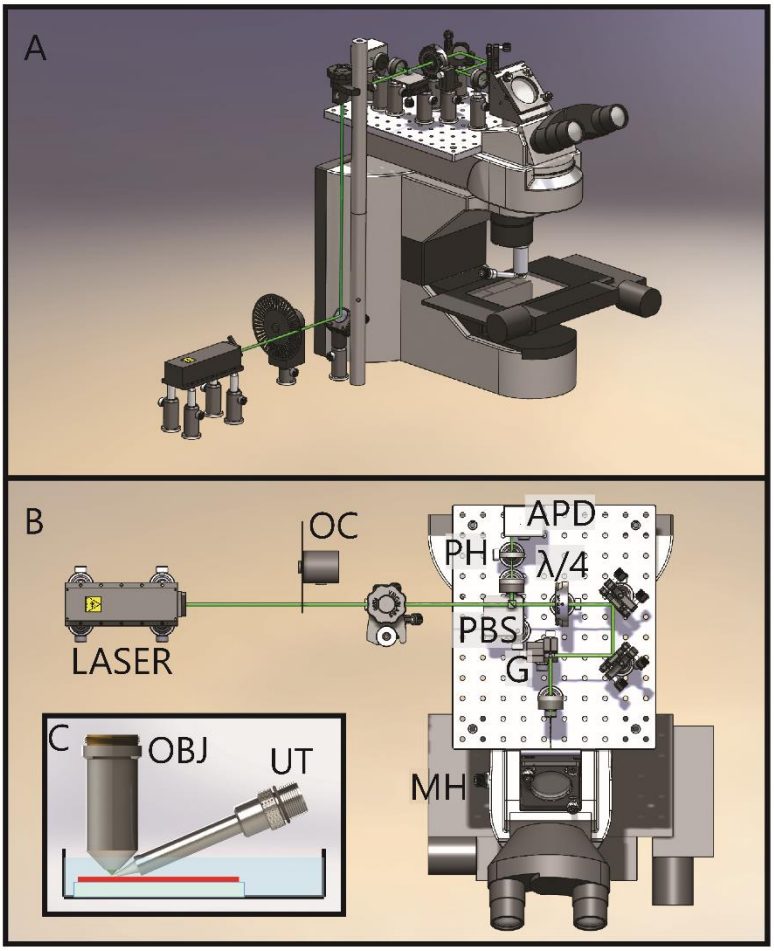

Figure 21. Rendering of proposed imaging system. (A) Isometric rendering of the hybrid TAUM/Confocal system. (B) Schematic of the hybrid TAUM/Confocal system where OC is an optical chopper, G is an x-y galvanometer scanning pair, SL and TL are a relay lens pair, MH is the microscope head, QWP denotes a quarter wave plate, PBS indicates a polarizing beam splitter, APD represents both the pinhole and the avalanche photodiode used for detection, Obj is the objective, UT is an ultrasonic transducer, and W is a tank for water immersion of the transducer objective pair. (C) Inset view of the microscope head. Without the optical chopper, this is simply the schematic of an off-axis PAM system hybridized with a confocal microscope.

In an effort to verify the theoretical sectioning capabilities of the confocal system, a cross sectional image was taken as a mirror was moved through the focal plane of the imaging system. Figure 22 shows the resulting profile of the scan, along with a Gaussian

fit. The full width at half maximum (FWHM) of the Gaussian fit is 500 nm, which matches well the theoretical value.

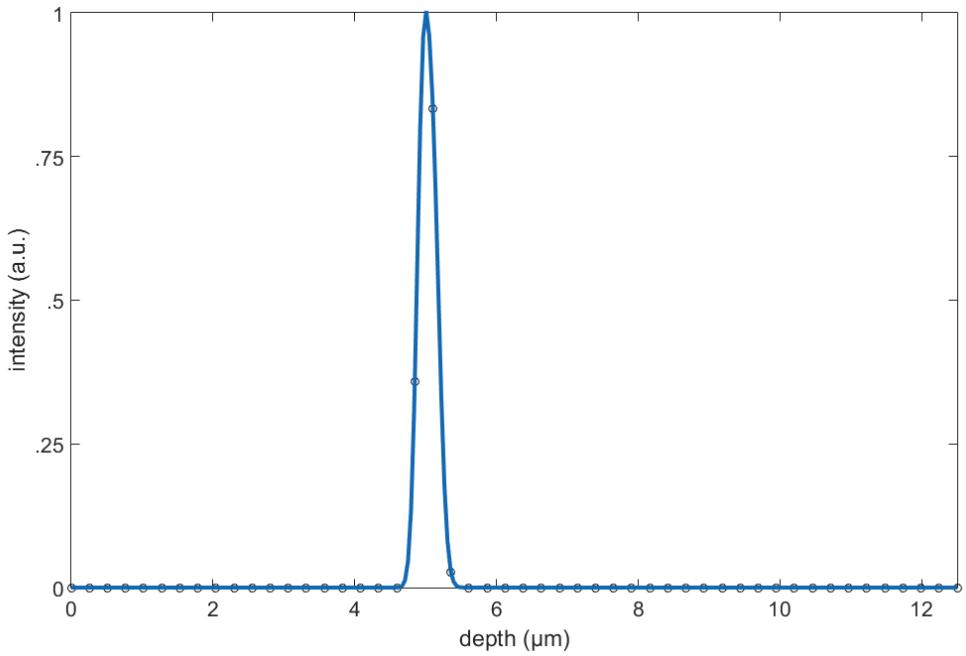

Figure 22. Confocal axial point spread function of the hybrid TAUM/confocal system. The FWHM is 0.5 μm, which well matches the theoretical resolution of the system.

Results and Discussion

After verifying the axial resolution of the confocal system, two dimensional scans were then taken. Hemoglobin is a common target for many PAM systems due to its strong absorption cross section in the visible range. For system characterization, a blood smear was prepared from fresh whole bovine blood. The blood sample was centrifuged at 4000 rcf for 5 minutes to isolate the erythrocytes. Next, the erythrocytes were diluted by a factor of 20 in phosphate buffered saline and fixed to a glass microscope slide using 95% methanol. The blood smear was then imaged using both *en face* and cross-sectional planes with the hybrid TAUM/confocal system. Pulse energies of 18 nJ were incident on the sample at a pulse repetition rate of 10 kHz.

Figure 23 shows *en face* image of erythrocytes from the blood smear. Figure 23-A is the confocal image of the erythrocytes, Figure 23-B is the TAUM image, and Figure 23-C is an overlay of the TAUM (red) and confocal (gray) images. Note that this is a true slice through the erythrocytes, evidenced by the donut shaped appearance of some of the erythrocytes in the TAUM and confocal signals while others appear disk shaped. Axial section of the system is demonstrated in a volumetric rendering, Figure 24, of the same blood smear. There is clear overlap between the confocal image (red) and the TAUM image (gray) in all three dimensions.

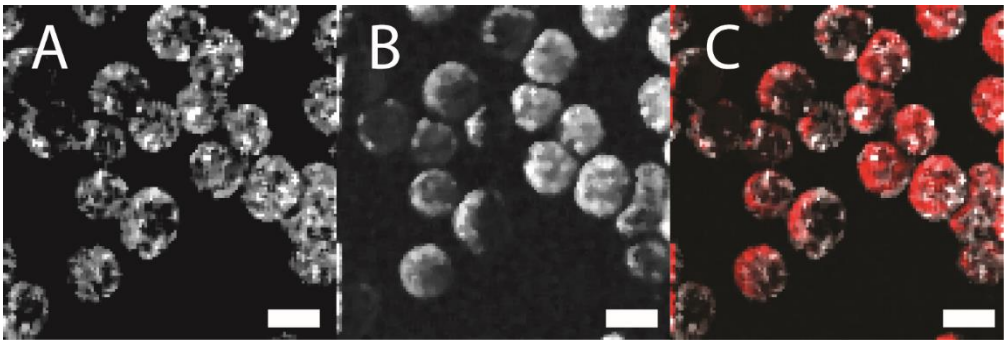

Figure 23. Hybrid TAUM and confocal images of fixed erythrocytes. (A) Confocal image of fixed bovine erythrocytes. (B) Corresponding TAUM image. (C) Hybrid TAUM (red) and confocal (gray) image of bovine erythrocytes fixed to a microscope slide. Scale bar is 10 µm.

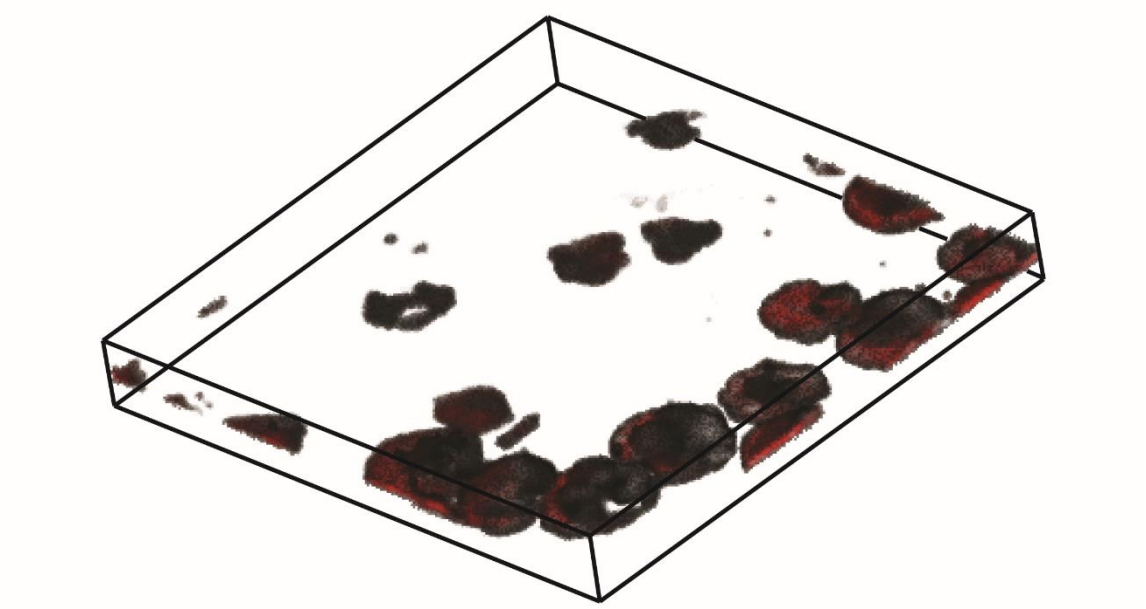

Figure 24. Volume image of fixed bovine erythrocytes captured with a hybrid TAUM (red) and confocal (gray) microscope.

At subcellular resolutions, a more interesting endogenous chromophore is cytochrome C. Cytochrome C is a hemeprotein which is integral to the electron transport chain and the aerobic pathway for the synthesis of adenosine triphosphate. In healthy cells cytochrome C is typically found associated with mitochondria in the cell cytoplasm, and localizes to

the nucleus following the start of apoptosis [119]. Photoacoustic microscopy has previously been demonstrated to be sensitive to cytochrome C, and there is excellent potential for imaging of cytochrome C distribution in cells.

3T3 Fibroblasts are a model cell for investigating cytochrome C *in vitro* and *ex vitro* as they have a high concentration of mitochondria. Freshly fixed 3T3 fibroblasts were obtained and imaged using the hybrid TAUM/confocal microscope to obtain label free images of cytochrome C distribution in the fixed cells.

Figure 25-A shows a low resolution view of a fixed fibroblast obtained using the confocal system. Figure 25-B shows the corresponding TAUM signal, and Figure 25-C shows an overlay of the TAUM (red) and confocal (gray) images. Figure 25-D shows a higher resolution confocal image of a different fibroblast. Figure 25-E shows the corresponding TAUM signal, and Figure 25-F shows an overlay of the TAUM (red) and confocal (gray) images. It is important to note that Figures 25-A, 25-B, and 25-C were obtained simultaneously. Likewise Figures 25-D, 25-E, and 25-F were also obtained simultaneously.

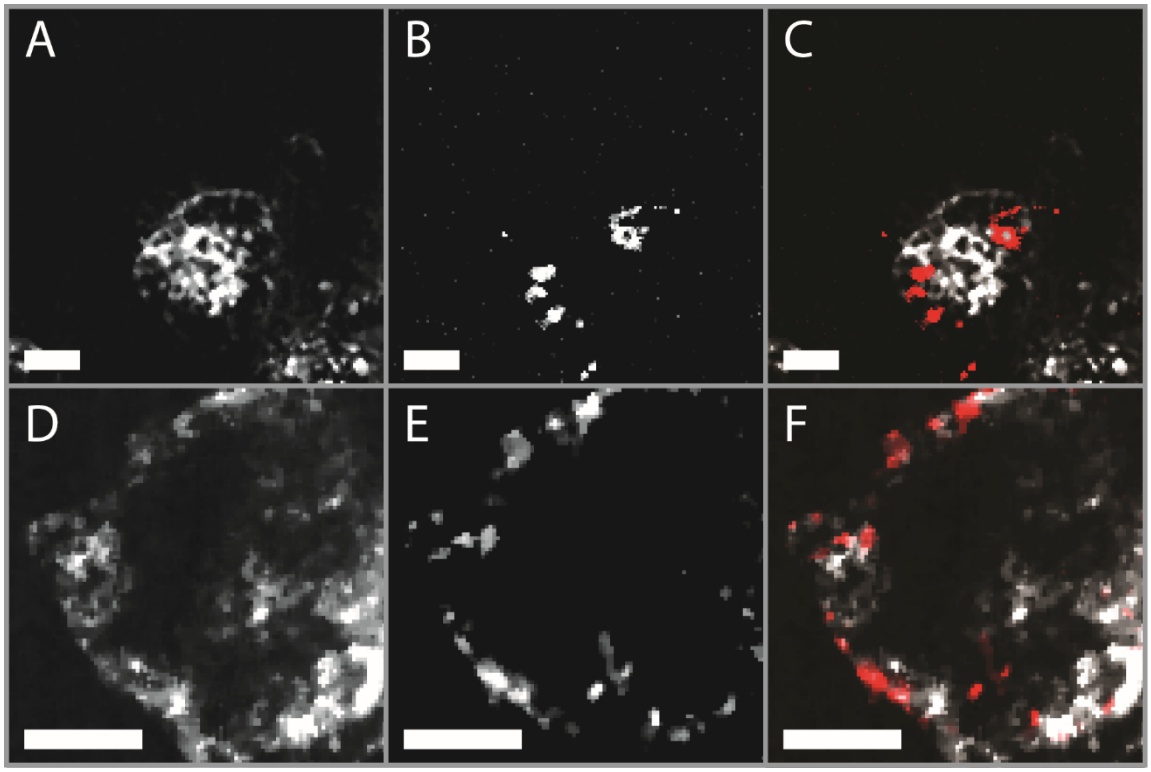

Figure 25. Hybrid TAUM and confocal images of fixed fibroblasts. (A&D) Confocal image of fixed fibroblast. (B&E) TAUM image of fixed fibroblast. (C&F) Overlay of TAUM (red) and confocal (gray) images from a fixed fibroblast. Scale bars are 10 µm.

TAUM and confocal are ideal candidates for a hybrid imaging system due to the complementary nature of their contrast mechanisms. Additionally, a confocal detection scheme may be easily added to an existing TAUM system with no loss of signal and minimal complication to the system design. Adding a TAUM detection scheme to an existing confocal microscope is more technically challenging as TAUM requires a pulsed light source and the addition of an ultrasonic detector. Additionally, TAUM requires multiple pulses to acquire each pixel which would require modification to the detection algorithm of an existing confocal microscope.

The ability to discern the morphological region surrounding areas of high absorption contrast furthers the potential for understanding of a variety of biological processes. Cytochromes [71], hemeproteins [120] involved in a variety of cellular processes, are an ideal target for the morphological system as they are difficult to resolve using standard confocal microscopy. TAUM images of molecular markers, without the morphological information provided by confocal microscopy, provide little insight into the underlying cell dynamics. Confocal images of cells provide little information about the distribution of molecular species. The combination of these two modalities provides complementary information to fully resolve the presence and distribution of various molecular species.

Conclusion

This section has demonstrated the usefulness of a combining a simplified technique for high-resolution photoacoustic microscopy with confocal microscopy. This approach enables high-resolution imaging in all dimensions for both absorption and scattering contrast. The axial sectioning of the photoacoustic microscopy is accomplished optically and is independent of the ultrasonic transducer making it an ideal partner of confocal microscopy. This technique has been demonstrated by fully resolving fixed bovine erythrocytes in all dimensions.

CHAPTER IV

MOLECULAR CONTRAST IN NON-LINEAR PHOTOACOUSTIC MICROSCOPY

Inherent Ability for Molecular Differentiation in Photoacoustic Imaging

This section of the manuscript discusses mechanisms for achieving molecular contrast inherently available to TAUM. Proper leverage of these physical phenomena may provide insight into a variety of applications in molecular imaging.

Introduction

Molecular contrast enables the detection of biomarkers deep within tissue. Both PAM and TAUM have innate molecular contrast through the absorption of light by biomarkers. However, standard approaches to PAM and TAUM cannot distinguish between absorbing molecules within tissue. The ability to differentiate between molecular markers with TAUM would enable the probing of biochemical processes on a subcellular level.

As defined earlier in Equation 1, PAM and TAUM have an inherent molecular contrast mechanism through the absorption coefficient, μ_a of the molecule being targeted. Molecules have a distinct absorption spectra and by varying the excitation wavelength of PAM or TAUM, the absorption profile of the molecule may be mapped. This approach has been utilized often using PAM to differentiate between oxygenated and deoxygenated

hemoglobin to map vasculature. Additional work has been performed to allow for the differentiation between melanin, oxygenated hemoglobin, and deoxygenated hemoglobin within tissues, demonstrating the usefulness of this approach for molecular differentiation.

In addition to the monitoring the absorption profile of a molecule, TAUM may also probe the transient absorption profile as well as the ground state recovery time of a molecule. As defined previously in Equation 11, TAUM signal is dependent upon the transient change in the absorption coefficient of a probe beam due to prior excitation by a pump beam. Just as a molecule has a distinct absorption spectrum, the transient absorption spectrum of a molecule is also distinct. The transient absorption spectrum may be mapped by varying the wavelength of either the pump or probe beam and mapping the TAUM signal.

The ground state recovery time of a molecule, defined as τ in Equation 11, is a distinct molecular property dependent upon both molecular properties and molecular environment. By varying the interpulse delay between the pump and the probe and recording the TAUM signal, the ground state recovery time of a molecule may be mapped. Prior work has demonstrated equivalence between TAUM measurements of the ground state recovery time and the fluorescent lifetime of rhodamine 6G, a common laser dye. Addition work has shown a distinct difference in the ground state recovery time of oxygenated and deoxygenated hemoglobin, demonstrating the potential for using TAUM measurements of the ground state recovery time to differentiate between biological markers.

Conclusion

There are several potential mechanism for differentiation of biological chromophores using PAM and TAUM. These approaches have previously been demonstrated for characterizing known fluorophores [54], differentiating between oxidation states of heme-proteins [54], and differentiating between various biomarkers [48].

Multispectral Transient Absorption Imaging via a Pulsed Comb-Light Source

This section of the manuscripts describes a prototype broad spectrum light source and its use in PAM and TAUM imaging. The narrow spectral line width and high pulse energies will enable spectroscopic PAM and TAUM imaging.

Introduction

In order to achieve molecular differentiation in the simplified TAUM schematic, it is necessary to utilize a light source capable of generating sufficient pulse energies across a range of tunable wavelengths. One solution to this problem is to use a dye laser, which is capable of providing tunable output based on the laser dye. Unfortunately, most dye lasers have a maximum repetition rate in the 10s of Hz [121]. For TAUM this would be equivalent to a pixel rate of 0.078 Hz or 12.8 seconds/pixel. An alternative approach is to use a super continuum laser source which can provide a pulsed light source over a broad spectral range [122]. Unfortunately, for most super continuum light sources the output power is not great enough within a small enough wavelength range to provide adequate photoacoustic emission for spectrally resolved TAUM. Stimulated Raman scattering in

optical fibers has previously been utilized to generate discrete laser lines for multiwavelength photoacoustic imaging [123].

Stimulated Raman scattering involves frequency downshifting light due to inelastic scattering of a light. Using a silica based single mode fiber will generate a stokes shift due to Raman scattering of 13.2 THz [124]. For a laser source centered around 532 nanometers, this will generate a peak approximately every 12 nanometers. Stimulated Raman scattering is polarization sensitive, as such it is beneficial to utilize a polarization maintaining optical fiber and control the polarization of light entering the fiber with a half wave plate to maximize the desired Raman peaks.

When a sufficiently intense laser pulse propagates through an optical medium, photons will undergo stimulated Raman scattering. When the first Stokes wave reaches a threshold value, a second stokes wave will be produced. This phenomenon can cascade to generate several Stokes lines that maintain the pulse duration of the input pulse; however, once the threshold for generating a higher order Stokes wave is passed, energy is lost from the lower order Stokes wave into the higher order waves.

Materials and Methods

A prototype broad spectrum light source was constructed to quantify the pulse energy which may be generated. A Q-switched DPSS laser (IQ 532-2 Crylas) with a pulse duration of 1.3 ns and a maximum repetition rate of 10 KHz was coupled into a 20 meter polarization maintaining (PM) single mode fiber (Thorlabs PM-S405-XP) with a mode field diameter of 4 μm. A schematic diagram of the prototype is shown in Figure 26. 400 μm of no-core fiber (Thorlabs FG125LA) was fusion spliced onto the end of the PM fiber

to allow coupling of high pulse energies without the risk of damaging the fiber. The output of the fiber was collimated and directed through a diffraction grating to separate the generated wavelengths. The separated beams were focused through a custom optical chopper then reimaged onto an identical diffraction grating to recombine the wavelengths into a single beam. The throughput efficiency of this system was 34.5 % of the input pulse energies, sufficient for TAUM imaging.

Figure 27-A depicts the normalized intensity of the stimulated Raman peaks output from the PM fiber. Additionally, Figure 27-B depicts the relationship between input pulse energy coupled into the fiber and the output pulse energies at each wavelength. The available wavelengths and power available at each wavelength may be tuned by selecting the optimal length of the single mode fiber, optimizing the amount of coupled light, and optimizing the polarization status of the laser entering the PM fiber. Notably, the power output at each wavelength is sufficient for photoacoustic generation and TAUM imaging.

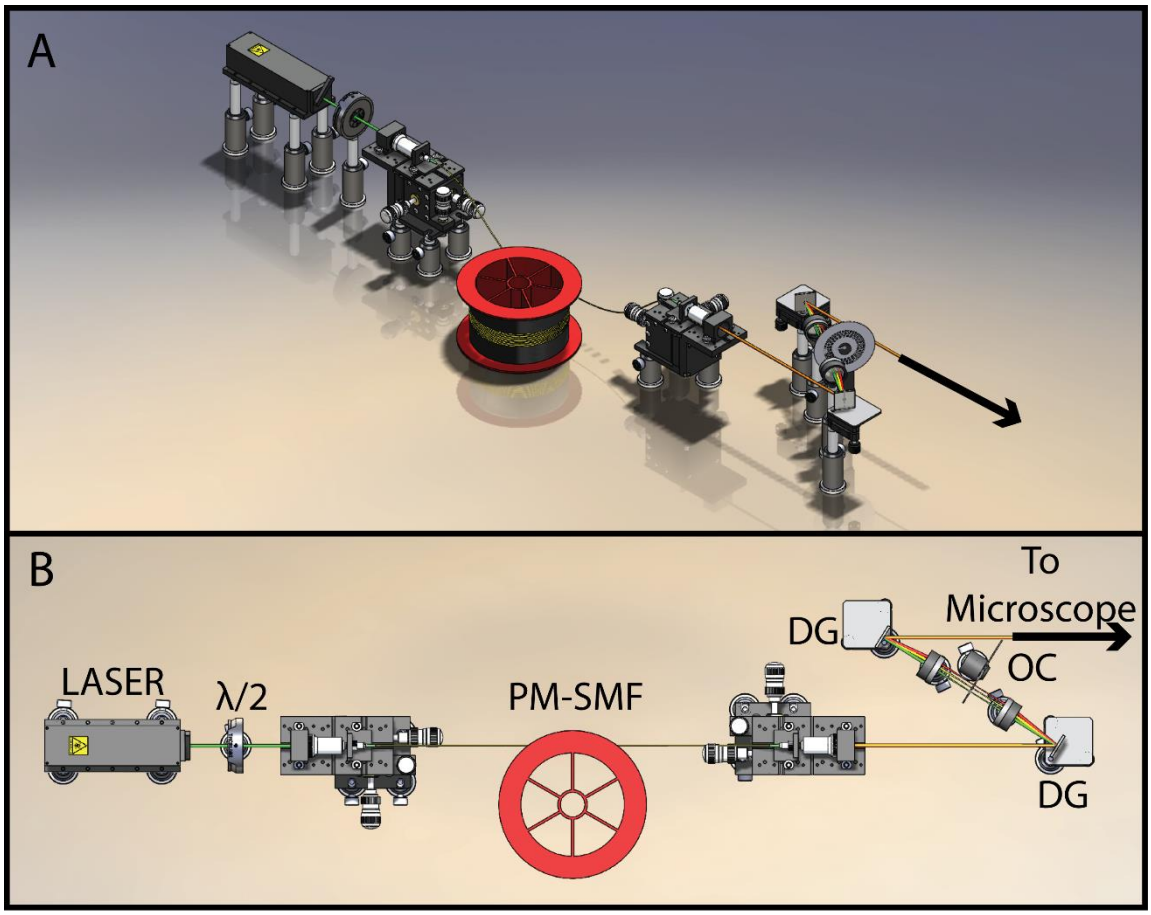

Figure 26. Schematic of prototype comb-broad spectrum laser. (A) Isometric rendering of the prototype system. (B) Top down schematic of the proposed system. λ/2 denotes a Half wave plate, PM-SMF indicates a polarization maintaining, single mode fiber, and OC is a custom made multi-frequency optical chopper. The combination of the diffraction grating and the optical chopper allows for isolation of various wavelengths in a single TAUM scan.

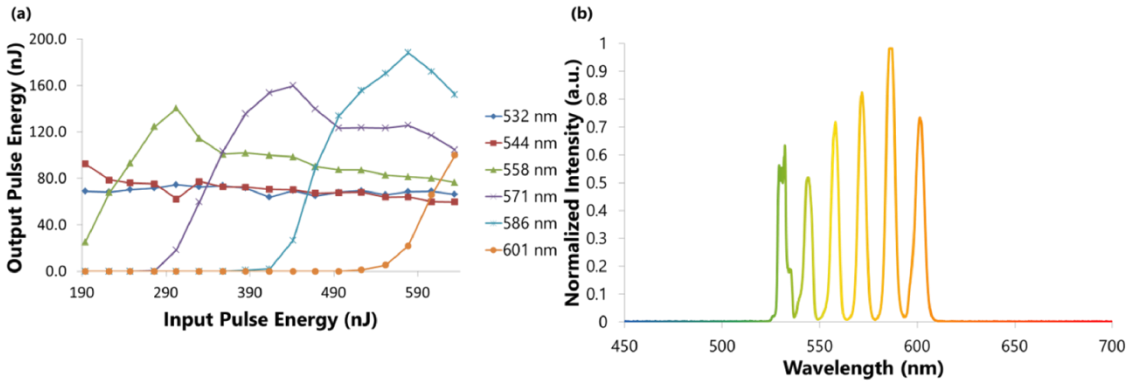

Figure 27. Output of prototype broadband pulsed light source. (A) Pulse energy throughput generated by stimulated Raman Scattering at various coupled pulse energies. (B) Spectral throughput of single mode fiber with 550 nJ coupled pulse power.

Results and Discussion

Rhodamine 6G is a common laser dye with a well-documented absorption spectrum. As such it was selected for preliminary multispectral TAUM studies. To optimize output power in each wavelength, only four wavelengths, 532 nm, 544.7 nm, 558 nm, and 572 nm were utilized for this study. TAUM signals from a 50µm inner diameter capillary tube were simultaneously captured for each wavelength. The signals were then adjusted to the square of the input pulse energy for each wavelength and normalized. The results were then plotted against the normalized absorbance for rhodamine 6G. Figure 28 shows the results of this experiment. It is interesting that the TAUM signal does not decay all the way to zero as would be expected from 570 nm excitation. There are a number of possible explanations for this phenomenon; however, the most likely scenario is there is some signal showing up as bleed through from the other transient absorption bands.

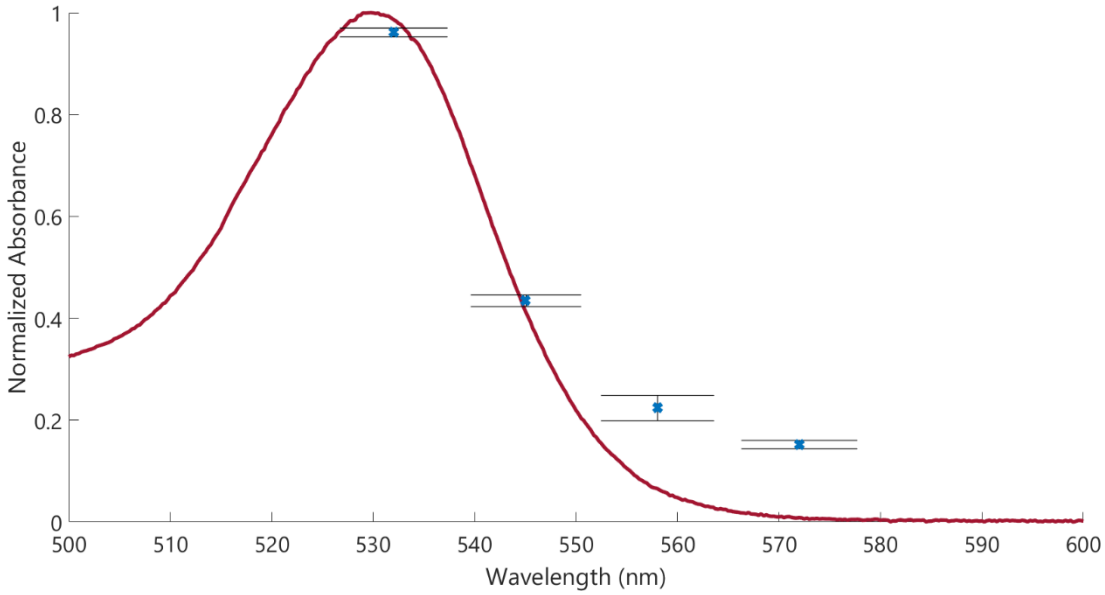

Figure 28. Multispectral transient absorption signal of rhodamine 6G plotted with the known absorption spectrum of rhodamine 6G.

The experiment was then repeated on a 50 µm inner diameter capillary tube filled with oxygenated hemoglobin. The same wavelengths, 532 nm, 544.7 nm, 558 nm, and 572 nm we utilized. The results were again normalized to the square of the incident pulse energy at each wavelength. The results are shown in Figure 29 below, with the trend of the TAUM signal closely following the trend of the absorbance of oxygenated hemoglobin.

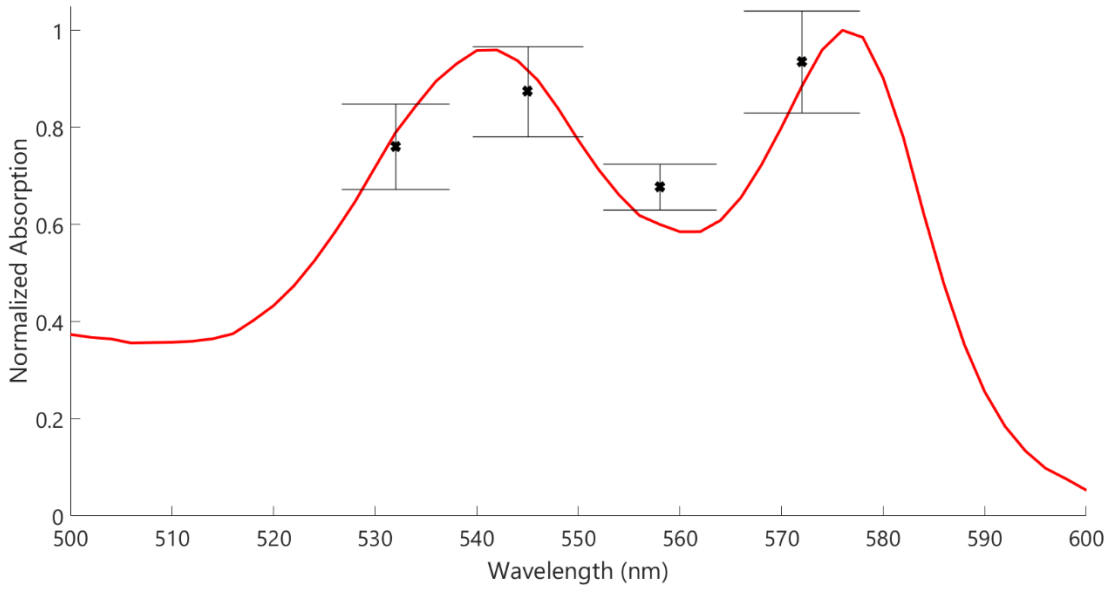

Figure 29. Multispectral TAUM signal from oxygenated hemoglobin plotted with the absorption spectrum for oxygenated hemoglobin.

Initial imaging data was taken from fixed fibroblasts using the prototype excitation source. Figure 30 shows a multispectral TAUM image of cytochromes within a fixed fibroblast. Only four wavelengths, 532 nm (Figure 30-A), 544.7 nm (Figure 30-B), 558 nm (Figure 30-C, and 572 nm (Figure 30-D), were utilized to achieve sufficient power for TAUM imaging in each wavelength. The raw TAUM data was then normalized to the square of the excitation intensity for each wavelengths and the datasets were normalized to the maximum and minimum of each of the four datasets. It is noteworthy that all of these images were captured simultaneously and therefore did not suffer from the effects of photobleaching between image captures. Figure 31 shows the corresponding average TAUM (red) and confocal (gray) image captured from this dataset.

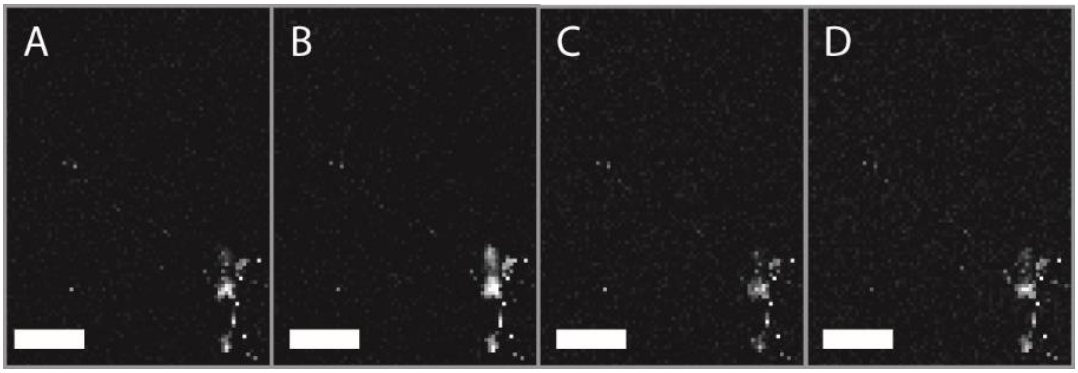

Figure 30. Multispectral TAUM image of cytochromes within a fixed fibroblast. (A) TAUM signal due to 532 nm excitation. (B) TAUM signal due to 543.5 nm excitation. (C) TAUM signal due to 555.6 nm excitation. (D) TAUM signal due to 568.3 nm excitation. All scale bars are 10 µm.

Figure 31. Combined confocal (gray) and multispectral TAUM (red) image of fixed fibroblast.

After filtering out noise, the TAUM signal for the whole image was extracted at each wavelength, normalized to the square of the input beam intensity. The signal was plotted against the known absorbance of both oxidized and reduced cytochrome C as shown in

Figure 32. However, more experimentation is required before any conclusions may be drawn from this data as the oxidation state of the cytochrome C was unknown prior to imaging.

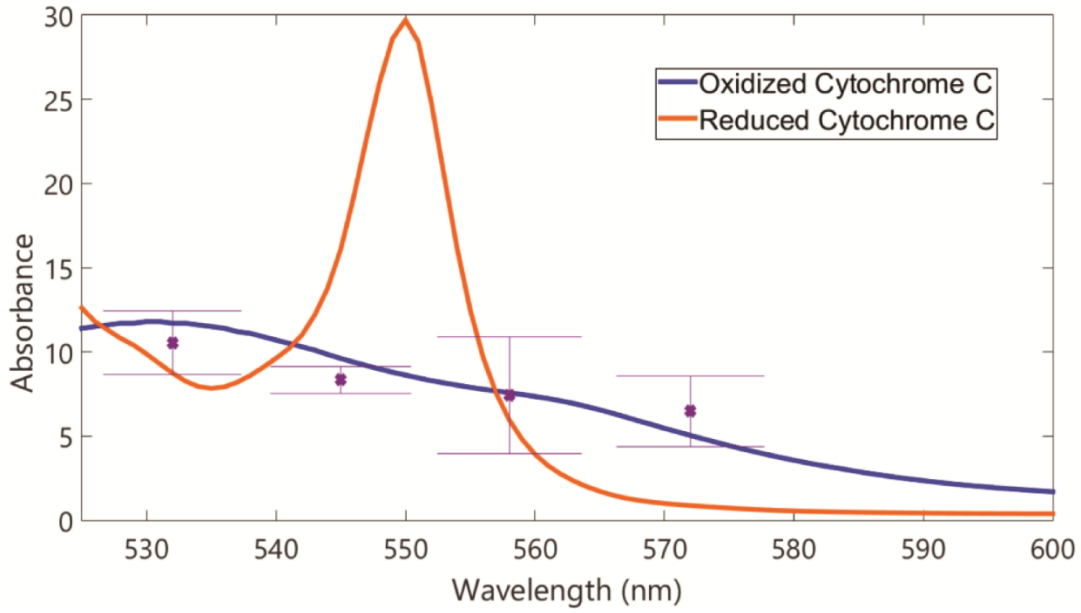

Figure 32. Normalized multispectral TAUM signal collected from fixed fibroblasts plotted with the oxidized and reduced spectrum of cytochrome C.

Conclusion

A prototype light source for a high resolution molecular specific photoacoustic microscope was developed. This approach utilizes stimulated Raman scattering within a simple mode fiber to generate discrete spectral lines for photoacoustic imaging. This light source is demonstrated in capturing multispectral TAUM images of cytochromes within a fixed fibroblast. With more background research, there is potential to image the oxidation

state of cytochromes in a sample, providing a high resolution glimpse into cell metabolism.

CHAPTER V

CONCLUSIONS AND FUTURE WORK

Conclusions

In summary, the purpose of this work was to develop and characterize a molecularly specific multiphoton photoacoustic microscope. This design was focused on improving methods for processing photoacoustic signals, combining TAUM complementary imaging modalities, and introducing potential methods for providing molecular contrast in TAUM. The need for such a microscope became apparent due to the lengthy post processing prevalent in photoacoustic microscopy and the lack of context for relevant high resolution TAUM images. Chapter I provides the motivation for increasing the resolution of traditional photoacoustic microscopy as well as the benefits of introducing molecular contrast to photoacoustic microscopy.

The first part of Chapter II details and compares post-processing methods for photoacoustic microscopy: quadrature demodulation and Hilbert transform enveloping. As photoacoustic signals are bipolar, they must be post-processed to adequately reconstruct the true morphology of the sample. Enveloping techniques, such as quadrature demodulation and Hilbert transform enveloping to transform bipolar signals into an accurate representation of the morphology of the sample. Raw, QD processed, and HT processed A-lines and B-scans are shown from data taken from the vasculature of a Syrian hamster cheek pouch. While both methods perform enveloping to reconstruct the expected

morphology, the HT method results in some bleed through of the modulation. This results in “shoulders” in the axial PSF.

Chapter II continues to detail the implementation of a real-time QD algorithm onto a field programmable gate array in-line with detection of the photoacoustic signal. The pipelining of the data flow through the FPGA is discussed in detail. Additionally, the imaging capabilities of this real time system are demonstrated both by imaging black hairs and imaging the beating heart of a zebrafish embryo. A volumetric dataset of the beating heart was assembled through post-acquisition synchronization of the acquired b-scans. This work became very important for the improvements to the multi-photon photoacoustic microscope as the processing served as the framework for the improved TAUM code.

The second half of Chapter II describes a traditional optical resolution photoacoustic microscope and the necessary post-processing required to adequately display the photoacoustic signals. This system later became the foundation for the multi-photon photoacoustic microscope. This system utilizes an off-axis detection scheme for its ultrasonic transducer. In an off-axis detection scheme, the acoustic detection axis is separated from the optical axis by simply angling the detector toward the sample and positioning it roughly 15 – 45 degrees off the optical axis. This system primarily benefits from the simplification of its optical design as it requires no custom components. A compromise for off-axis PAM is a moderate decrease in axial resolution equivalent to the inverse of the cosine of the detection angle.

Chapter III describes the design improvement of imaging and post-processing techniques of a multiphoton photoacoustic microscope. By moving from post processing

of the acquired TAUM signal to in-line processing using the FPGA, the speed of TAUM imaging was vastly improved. The processing capabilities of the FPGA were characterized by imaging whole erythrocytes on a microscope slide. Axial resolution of the system is characterized to be ~1.5 μm with a 40x microscope objective (Nikon Fluor 40x). Volumetric reconstructions of erythrocytes are also demonstrated. This work represented the first time single erythrocytes were ever fully resolved using photoacoustic imaging.

The second section of Chapter III details improvements to the design of the optical system of a TAUM system. The removal of the delay line from the pump and the probe greatly simplifies the optical setup of a TAUM system. By collapsing the time delay to zero and using the same optical path as both the pump and the probe pathways, a TAUM system may be built from any existing PAM system with the simple addition of an optical modulator in the beam path. Additionally, a mathematical derivation of the TAUM signal is formalized in this work. The axial resolution of the simplified TAUM system is demonstrated to be equivalent to previous TAUM work and volumetric images of erythrocytes are captured.

The final section of Chapter III leverages the simplified TAUM design to build a hybrid TAUM/confocal microscope into an upright Nikon microscope. The axial resolutions of both systems are characterized and shown to be equivalent. The morphological information obtained from the confocal microscope complements the absorption information that may be obtained by TAUM. Adding context to the absorption information in tissue samples vastly improves the ability to understand the information

that has been obtained from a sample. This system was demonstrated on whole bovine erythrocytes.

The first section of Chapter IV introduces the concept of time resolved TAUM imaging to measure the ground state recovery time of molecules. Time resolved TAUM imaging is made possible by modifying the TAUM setup to include a second laser and controlling the interpulse delay between the two laser sources. By mapping the TAUM intensity at each interpulse delay, the ground state recovery time may be directly measured. The accuracy of this technique was verified in Rhodamine 6G, a well-documented chromophore. The measured ground state recovery time was found to be 3.3 ns, which reasonable matches the published fluorescent lifetime of 4ns. The ground state recovery time of the oxy and deoxy forms of hemoglobin were also measured as 3.65 ns and 7.9 ns, respectively. These results suggest that future TAUM systems could be used to measure the oxygen saturation of blood using a single wavelength.

Chapter IV ends with the design and demonstration of a prototype broad spectrum light source. This light source provides the narrow spectral lines required for spectroscopic photoacoustic imaging. Integration of this light source into the existing PAM and TAUM imaging systems will enable molecular contrast through the varied absorption spectra of biological targets. By optimizing the source discussed in Figure 26, output wavelengths may be selected via control of the digital mirror device. Additionally, rotation of the half wave plate prior to the optical fiber allows for tuning of the amplified wavelength. The transient absorption spectra from a variety were captured and compared to their known

absorption spectra. Additionally, the ability to capture transient absorption spectral images was demonstrated.

Future Work

Future work on the optical resolution PAM system should include the integration of the prototype broad spectrum light source. With minor modification to the existing FPGA code, this system could potentially image blood oxygen concentration with real-time processing of the photoacoustic data. Additionally, any information gained from the spectroscopic PAM imaging would provide insight for the molecular specific TAUM system.

Future work concerning the TAUM system should include leveraging the TAUM/confocal hybrid system for imaging the targets outlined in the potential cellular and molecular targets section of Chapter I. Investigation of these chromophores, especially cytochrome C, will likely prove to be quite fruitful to the field of high resolution photoacoustic microscopy. Preliminary work has already been demonstrated for imaging of cytochrome C in fibroblasts. A demonstration of the feasibility of the hybrid TAUM/confocal system for cellular biology applications would solidify this technique as a potential alternative to exogenous labeling. Ruiz-Vela, *et al.* demonstrated that cytochrome C relocates from the mitochondria to the nucleus when the cell undergoes apoptosis [119]. A relevant experiment would be to duplicate these results without the use of exogenous labels using the hybrid TAUM/confocal microscope.

To improve upon molecular specific TAUM work, the sensitivity of the broad spectrum pulsed light source should be characterized by tissues samples containing molecules of interest. The primary goal of these experiments should be to establish the feasibility of acquiring a spectrally encoded TAUM image using the broad spectrum light source. This method will be ideal for differentiating of oxidation states of hemeproteins. The distinct absorption spectrum of hemeproteins provides an ideal starting place for the imaging system. While hemoglobin is an excellent starting point when imaging hemeproteins, imaging of the redox pairs of the cytochrome C may provide direct insight into cellular metabolism.

In the long term, greater focus should be given to developing algorithms for determining the redox state of cytochrome C and other hemeproteins using TAUM. These algorithms would provide potential for direct measurement of dynamic cell metabolism. Cytochrome C is particularly challenging as it is most highly concentrated within the mitochondria, a small structure on the order of 100s of nm. Additionally, the absorption spectra of several proteins involved in the electron transport chain closely overlap with the absorption spectrum of cytochrome C. TAUM is uniquely primed to overcome these challenges as it is capable of high resolution imaging and can provide independent measurements of two distinct molecular properties.

Attempts to improve the imaging speed of TAUM may also be made by moving to a higher repetition rate light source. Additionally, moving to a picosecond light source will provide multiple advantages. First, a picosecond light source would allow for more accurate measurement of ground state recovery time from a much larger pool of

chromophores than the current system can access. Many biological molecules, such as melanin, have been shown to exhibit lifetimes on the order of 10s of picoseconds. This lifetime is not readily measurable with either of the current sources used for TAUM imaging due to their longer (600 ps and 1.3 ns) pulse durations. Additionally, picosecond light sources are available with much higher repetition rates than our current light sources. Finally, a picoseconds light source will generate more stable stimulated Raman scattering within a single mode fiber, improving the pulse stability of our prototype broad spectrum light source. These improvements will enable TAUM to be a successful high resolution imaging system for molecular targets.

REFERENCES

[1] G. D. Ludwig and F. W. Struthers, “Considerations Underlying the use of Ultrasound to Detect Gallstones and Foreign Bodies in Tissue,” Jun. 1949.

[2] W. H. Oldendorf, “Isolated Flying Spot Detection of Radiodensity Dis-Continuities-Displaying the Internal Structural Pattern of a Complex Object,” *Ire Trans. Biomed. Electron.*, vol. 8, no. 1, pp. 68–72, Jan. 1961.

[3] P. C. Lauterbur, “Image Formation by Induced Local Interactions: Examples Employing Nuclear Magnetic Resonance,” *Nature*, vol. 242, no. 5394, pp. 190–191, Mar. 1973.

[4] D. D. Adler, P. L. Carson, J. M. Rubin, and D. Quinn-Reid, “Doppler ultrasound color flow imaging in the study of breast cancer: Preliminary findings,” *Ultrasound Med. Biol.*, vol. 16, no. 6, pp. 553–559, Jan. 1990.

[5] R. Aaslid, T. M. Markwalder, and H. Nornes, “Noninvasive transcranial Doppler ultrasound recording of flow velocity in basal cerebral arteries.,” *J. Neurosurg.*, vol. 57, no. 6, pp. 769–74, Dec. 1982.

[6] K. J. Friston, P. Jezzard, and R. Turner, “Analysis of functional MRI time-series,” *Hum. Brain Mapp.*, vol. 1, no. 2, pp. 153–171, Oct. 1994.

[7] S. Iskander and A. E. Iskandrian, “Risk assessment using single-photon emission computed tomographic technetium-99m sestamibi imaging,” *J. Am. Coll. Cardiol.*, vol. 32, no. 1, pp. 57–62, Jul. 1998.

[8] H. T. Chugani, M. E. Phelps, and J. C. Mazziotta, “Positron emission tomography study of human brain functional development.,” *Ann. Neurol.*, vol. 22, no. 4, pp. 487–97, Oct. 1987.

[9] D. M. Shotton, “Confocal scanning optical microscopy and its applications for biological specimens,” *J. Cell Sci.*, vol. 94, no. 2, pp. 175–206, Oct. 1989.

[10] S. González and Z. Tannous, “Real-time, in vivo confocal reflectance microscopy of basal cell carcinoma.,” *J. Am. Acad. Dermatol.*, vol. 47, no. 6, pp. 869–74, Dec. 2002.

[11] R. Kiesslich, J. Burg, M. Vieth, J. Gnaendiger, M. Enders, P. Delaney, A. Polglase, W. McLaren, D. Janell, S. Thomas, B. Nafe, P. R. Galle, and M. F. Neurath, “Confocal laser endoscopy for diagnosing intraepithelial neoplasias and colorectal

cancer in vivo," *Gastroenterology*, vol. 127, no. 3, pp. 706–713, Sep. 2004.

[12] C. Zeng, S. Vangveravong, J. Xu, K. C. Chang, R. S. Hotchkiss, K. T. Wheeler, D. Shen, Z.-P. Zhuang, H. F. Kung, and R. H. Mach, "Subcellular localization of sigma-2 receptors in breast cancer cells using two-photon and confocal microscopy.," *Cancer Res.*, vol. 67, no. 14, pp. 6708–16, Jul. 2007.

[13] H. Sato, T. Suzuki, B. B. Andriana, S. Morita, A. Maruyama, H. Shinzawa, Y. Komachi, G. Kanai, N. Ura, K. Masutani, Y. Matsuura, M. Toi, T. Shimosegawa, and Y. Ozaki, "An optical biopsy system with miniaturized raman and spectral imaging probes; in vivo animal and ex vivo clinical application studies," in *SPIE BiOS: Biomedical Optics*, 2009, p. 71690M–71690M–8.

[14] J. G. Fujimoto, M. E. Brezinski, G. J. Tearney, S. A. Boppart, B. Bouma, M. R. Hee, J. F. Southern, and E. A. Swanson, "Optical biopsy and imaging using optical coherence tomography," *Nat. Med.*, vol. 1, no. 9, pp. 970–972, Sep. 1995.

[15] S. Bota, J. B. Auliac, C. Paris, J. Métayer, R. Sesboüé, G. Nouvet, and L. Thiberville, "Follow-up of bronchial precancerous lesions and carcinoma in situ using fluorescence endoscopy.," *Am. J. Respir. Crit. Care Med.*, vol. 164, no. 9, pp. 1688–93, Nov. 2001.

[16] W. Denk, J. Strickler, and W. Webb, "Two-photon laser scanning fluorescence microscopy," *Science (80-.).*, vol. 248, no. 4951, pp. 73–76, Apr. 1990.

[17] J. A. Giordmaine, "Two-Photon Excitation of Fluorescence by Picosecond Light Pulses," *Appl. Phys. Lett.*, vol. 11, no. 7, p. 216, Nov. 1967.

[18] J. M. Squirrell, D. L. Wokosin, J. G. White, and B. D. Bavister, "Long-term two-photon fluorescence imaging of mammalian embryos without compromising viability.," *Nat. Biotechnol.*, vol. 17, no. 8, pp. 763–7, Aug. 1999.

[19] M. G. L. Gustafsson, "Surpassing the lateral resolution limit by a factor of two using structured illumination microscopy.," *J. Microsc.*, vol. 198, no. 2, pp. 82–87, May 2000.

[20] J. Huisken, J. Swoger, F. Del Bene, J. Wittbrodt, and E. H. K. Stelzer, "Optical sectioning deep inside live embryos by selective plane illumination microscopy.," *Science*, vol. 305, no. 5686, pp. 1007–9, Aug. 2004.

[21] M. Chalfie, "Green Fluorescent Protein," *Photochem. Photobiol.*, vol. 62, no. 4, pp. 651–656, Oct. 1995.

[22] L. Cong, F. A. Ran, D. Cox, S. Lin, R. Barretto, N. Habib, P. D. Hsu, X. Wu, W. Jiang, L. A. Marraffini, and F. Zhang, "Multiplex genome engineering using CRISPR/Cas systems.," *Science*, vol. 339, no. 6121, pp. 819–23, Feb. 2013.

[23] Y. Fu, H. Wang, R. Shi, and J. X. Cheng, "Second harmonic and sum frequency generation imaging of fibrous astroglial filaments in ex vivo spinal tissues.," *Biophys. J.*, vol. 92, no. 9, pp. 3251–9, May 2007.

[24] D. Oron, D. Yelin, E. Tal, S. Raz, R. Fachima, and Y. Silberberg, "Depth-resolved structural imaging by third-harmonic generation microscopy.," *J. Struct. Biol.*, vol. 147, no. 1, pp. 3–11, Jul. 2004.

[25] P. J. Campagnola, M. D. Wei, A. Lewis, and L. M. Loew, "High-resolution nonlinear optical imaging of live cells by second harmonic generation.," *Biophys. J.*, vol. 77, no. 6, pp. 3341–9, Dec. 1999.

[26] E. Brown, T. McKee, E. diTomaso, A. Pluen, B. Seed, Y. Boucher, and R. K. Jain, "Dynamic imaging of collagen and its modulation in tumors in vivo using second-harmonic generation.," *Nat. Med.*, vol. 9, no. 6, pp. 796–800, Jun. 2003.

[27] J.-X. Cheng, L. D. Book, and X. S. Xie, "Polarization coherent anti-Stokes Raman scattering microscopy," *Opt. Lett.*, vol. 26, no. 17, p. 1341, Sep. 2001.

[28] A. Zumbusch, G. Holtom, and X. Xie, "Three-Dimensional Vibrational Imaging by Coherent Anti-Stokes Raman Scattering," *Phys. Rev. Lett.*, vol. 82, no. 20, pp. 4142–4145, May 1999.

[29] B. Hein, K. I. Willig, and S. W. Hell, "Stimulated emission depletion (STED) nanoscopy of a fluorescent protein-labeled organelle inside a living cell.," *Proc. Natl. Acad. Sci. U. S. A.*, vol. 105, no. 38, pp. 14271–6, Sep. 2008.

[30] M. J. Rust, M. Bates, and X. Zhuang, "Sub-diffraction-limit imaging by stochastic optical reconstruction microscopy (STORM).," *Nat. Methods*, vol. 3, no. 10, pp. 793–5, Oct. 2006.

[31] H. Shroff, C. G. Galbraith, J. A. Galbraith, and E. Betzig, "Live-cell photoactivated localization microscopy of nanoscale adhesion dynamics.," *Nat. Methods*, vol. 5, no. 5, pp. 417–23, May 2008.

[32] M. Luukkala and A. Penttinen, "Photoacoustic microscope," *Electron. Lett.*, vol. 15, no. 11, p. 325, May 1979.

[33] M. Xu and L. V. Wang, "Photoacoustic imaging in biomedicine," *Rev. Sci.*

Instrum., vol. 77, no. 4, p. 041101, Apr. 2006.

[34] X. Wang, Y. Pang, G. Ku, X. Xie, G. Stoica, and L. V. Wang, "Noninvasive laser-induced photoacoustic tomography for structural and functional in vivo imaging of the brain.," *Nat. Biotechnol.*, vol. 21, no. 7, pp. 803–6, Jul. 2003.

[35] R. O. Esenaliev, A. A. Karabutov, and A. A. Oraevsky, "Sensitivity of laser opto-acoustic imaging in detection of small deeply embedded tumors," *IEEE J. Sel. Top. Quantum Electron.*, vol. 5, no. 4, pp. 981–988, 1999.

[36] K. Maslov, G. Stoica, and L. V. Wang, "In vivo dark-field reflection-mode photoacoustic microscopy.," *Opt. Lett.*, vol. 30, no. 6, pp. 625–7, Mar. 2005.

[37] C. G. A. Hoelen, F. F. M. de Mul, R. Pongers, and A. Dekker, "Three-dimensional photoacoustic imaging of blood vessels in tissue," *Opt. Lett.*, vol. 23, no. 8, p. 648, Apr. 1998.

[38] X. Wang, X. Xie, G. Ku, L. V. Wang, and G. Stoica, "Noninvasive imaging of hemoglobin concentration and oxygenation in the rat brain using high-resolution photoacoustic tomography.," *J. Biomed. Opt.*, vol. 11, no. 2, p. 024015, Jan. 2006.

[39] C. Zhang, Y. S. Zhang, D. K. Yao, Y. Xia, and L. V. Wang, "Label-free photoacoustic microscopy of cytochromes.," *J. Biomed. Opt.*, vol. 18, no. 2, p. 20504, Feb. 2013.

[40] J. A. Westrick and K. S. Peters, "A photoacoustic calorimetric study of horse myoglobin," *Biophys. Chem.*, vol. 37, no. 1–3, pp. 73–79, Aug. 1990.

[41] B. E. Urban, J. Yi, V. Yakovlev, and H. F. Zhang, "Investigating femtosecond-laser-induced two-photon photoacoustic generation.," *J. Biomed. Opt.*, vol. 19, no. 8, p. 085001, Aug. 2014.

[42] D. L. Chamberland, A. Agarwal, N. Kotov, J. Brian Fowlkes, P. L. Carson, and X. Wang, "Photoacoustic tomography of joints aided by an Etanercept-conjugated gold nanoparticle contrast agent-an ex vivo preliminary rat study.," *Nanotechnology*, vol. 19, no. 9, p. 095101, Mar. 2008.

[43] L. Li, R. J. Zemp, G. Lungu, G. Stoica, and L. V. Wang, "Photoacoustic imaging of lacZ gene expression in vivo.," *J. Biomed. Opt.*, vol. 12, no. 2, p. 020504, Jan. 2007.

[44] J. Xia, J. Yao, and L. V. Wang, "Photoacoustic tomography: principles and advances.," *Electromagn. waves (Cambridge, Mass.)*, vol. 147, pp. 1–22, Jan. 2014.

[45] L. V. Wang, “Tutorial on photoacoustic microscopy and computed tomography,” *IEEE J. Sel. Top. Quantum Electron.*, vol. 14, no. 1, pp. 171–179, 2008.

[46] S. P. Mattison, R. L. Shelton, R. T. Maxson, and B. E. Applegate, “Continuous real-time photoacoustic demodulation via field programmable gate array for dynamic imaging of zebrafish cardiac cycle.,” *Biomed. Opt. Express*, vol. 4, no. 8, pp. 1451–63, Jan. 2013.

[47] C. M. W. Daft, G. A. D. Briggs, and W. D. O’Brien, “Frequency dependence of tissue attenuation measured by acoustic microscopy,” in *IEEE 1988 Ultrasonics Symposium Proceedings.*, 1988, pp. 971–974.

[48] H. F. Zhang, K. Maslov, G. Stoica, and L. V. Wang, “Functional photoacoustic microscopy for high-resolution and noninvasive in vivo imaging.,” *Nat. Biotechnol.*, vol. 24, no. 7, pp. 848–51, Jul. 2006.

[49] K. Maslov, H. F. Zhang, S. Hu, and L. V. Wang, “Optical-resolution photoacoustic microscopy for in vivo imaging of single capillaries,” *Opt. Lett.*, vol. 33, no. 9, p. 929, Apr. 2008.

[50] E. M. Strohm, E. S. L. Berndl, and M. C. Kolios, “High frequency label-free photoacoustic microscopy of single cells.,” *Photoacoustics*, vol. 1, no. 3–4, pp. 49–53, Dec. 2013.

[51] C. Zhang, K. Maslov, and L. V. Wang, “Subwavelength-resolution label-free photoacoustic microscopy of optical absorption in vivo.,” *Opt. Lett.*, vol. 35, no. 19, pp. 3195–7, Oct. 2010.

[52] A. Danielli, K. Maslov, A. Garcia-Uribe, A. M. Winkler, C. Li, L. Wang, Y. Chen, G. W. Dorn, and L. V. Wang, “Label-free photoacoustic nanoscopy.,” *J. Biomed. Opt.*, vol. 19, no. 8, p. 086006, Aug. 2014.

[53] R. L. Shelton and B. E. Applegate, “Ultrahigh resolution photoacoustic microscopy via transient absorption.,” *Biomed. Opt. Express*, vol. 1, no. 2, pp. 676–686, Jan. 2010.

[54] R. L. Shelton, S. P. Mattison, and B. E. Applegate, “Molecular specificity in photoacoustic microscopy by time-resolved transient absorption.,” *Opt. Lett.*, vol. 39, no. 11, pp. 3102–5, Jun. 2014.

[55] J. B. Pawley, Ed., *Handbook Of Biological Confocal Microscopy*. Boston, MA: Springer US, 2006.

[56] D. V Patel and C. N. J. McGhee, “Contemporary in vivo confocal microscopy of the living human cornea using white light and laser scanning techniques: a major review.,” *Clin. Experiment. Ophthalmol.*, vol. 35, no. 1, pp. 71–88, Jan. 2007.

[57] J. M. Jabbour, B. H. Malik, C. Olsovsky, R. Cuenca, S. Cheng, J. A. Jo, Y. S. L. Cheng, J. M. Wright, and K. C. Maitland, “Optical axial scanning in confocal microscopy using an electrically tunable lens.,” *Biomed. Opt. Express*, vol. 5, no. 2, pp. 645–52, Feb. 2014.

[58] M. Gu, C. J. R. Sheppard, and X. Gan, “Image formation in a fiber-optical confocal scanning microscope,” *J. Opt. Soc. Am. A*, vol. 8, no. 11, p. 1755, Nov. 1991.

[59] R. Berera, R. van Grondelle, and J. T. M. Kennis, “Ultrafast transient absorption spectroscopy: principles and application to photosynthetic systems,” *Photosynth. Res.*, vol. 101, no. 2–3, pp. 105–118, Jul. 2009.

[60] D. Fu, T. Ye, T. E. Matthews, B. J. Chen, G. Yurtserver, and W. S. Warren, “High-resolution in vivo imaging of blood vessels without labeling.,” *Opt. Lett.*, vol. 32, no. 18, pp. 2641–3, Sep. 2007.

[61] D. Fu, T. Ye, T. E. Matthews, G. Yurtsever, and W. S. Warren, “Two-color, two-photon, and excited-state absorption microscopy.,” *J. Biomed. Opt.*, vol. 12, no. 5, p. 054004, Jan. 2007.

[62] H. Kang, S. W. Lee, E.-S. Lee, S. H. Kim, and T. G. Lee, “Real-time GPU-accelerated processing and volumetric display for wide-field laser-scanning optical-resolution photoacoustic microscopy,” *Biomed. Opt. Express*, vol. 6, no. 12, p. 4650, Nov. 2015.

[63] C. Zhang, K. Maslov, J. Yao, and L. V. Wang, “In vivo photoacoustic microscopy with 7.6-μm axial resolution using a commercial 125-MHz ultrasonic transducer.,” *J. Biomed. Opt.*, vol. 17, no. 11, p. 116016, Nov. 2012.

[64] R. L. Shelton and B. E. Applegate, “Off-axis photoacoustic microscopy.,” *IEEE Trans. Biomed. Eng.*, vol. 57, no. 8, pp. 1835–8, Aug. 2010.

[65] A. S. Popel, “Theory of oxygen transport to tissue.,” *Crit. Rev. Biomed. Eng.*, vol. 17, no. 3, pp. 257–321, Jan. 1989.

[66] W. Zijlstra and A. Buursma, “Spectrophotometry of Hemoglobin: Absorption Spectra of Bovine Oxyhemoglobin, Deoxyhemoglobin, Carboxyhemoglobin, and Methemoglobin,” *Comp. Biochem. Physiol. Part B Biochem. Mol. Biol.*, vol. 118, no. 4, pp. 743–749, Dec. 1997.

[67] S. Hu, K. Maslov, and L. V. Wang, “Noninvasive label-free imaging of microhemodynamics by optical-resolution photoacoustic microscopy,” *Opt. Express*, vol. 17, no. 9, p. 7688, Apr. 2009.

[68] J. Yao, L. Wang, J. M. Yang, K. I. Maslov, T. T. W. Wong, L. Li, C.-H. Huang, J. Zou, and L. V. Wang, “High-speed label-free functional photoacoustic microscopy of mouse brain in action.,” *Nat. Methods*, vol. 12, no. 5, pp. 407–10, May 2015.

[69] L. D. Liao, M. L. Li, H.-Y. Lai, Y. Y. I. Shih, Y. C. Lo, S. Tsang, P. C. P. Chao, C. T. Lin, F. S. Jaw, and Y. Y. Chen, “Imaging brain hemodynamic changes during rat forepaw electrical stimulation using functional photoacoustic microscopy.,” *Neuroimage*, vol. 52, no. 2, pp. 562–70, Aug. 2010.

[70] K. Blinova, S. Carroll, S. Bose, A. V Smirnov, J. J. Harvey, J. R. Knutson, and R. S. Balaban, “Distribution of mitochondrial NADH fluorescence lifetimes: steady-state kinetics of matrix NADH interactions.,” *Biochemistry*, vol. 44, no. 7, pp. 2585–94, Feb. 2005.

[71] M. K. F. Wikstrom, “Proton pump coupled to cytochrome c oxidase in mitochondria,” *Nature*, vol. 266, no. 5599, pp. 271–273, Mar. 1977.

[72] M. Jastroch, A. S. Divakaruni, S. Mookerjee, J. R. Treberg, and M. D. Brand, “Mitochondrial proton and electron leaks.,” *Essays Biochem.*, vol. 47, pp. 53–67, Jan. 2010.

[73] R. A. Gatenby and R. J. Gillies, “Why do cancers have high aerobic glycolysis?,” *Nat. Rev. Cancer*, vol. 4, no. 11, pp. 891–9, Nov. 2004.

[74] A. D. Hershey, “Independent Functions of Viral Protein and Nucleic Acid in Growth of Bacteriophage,” *J. Gen. Physiol.*, vol. 36, no. 1, pp. 39–56, Sep. 1952.

[75] J. D. Watson and C. Levinthal., “Molecular biology of the gene.,” 1965.

[76] B. E. Bernstein, T. S. Mikkelsen, X. Xie, M. Kamal, D. J. Huebert, J. Cuff, B. Fry, A. Meissner, M. Wernig, K. Plath, R. Jaenisch, A. Wagschal, R. Feil, S. L. Schreiber, and E. S. Lander, “A bivalent chromatin structure marks key developmental genes in embryonic stem cells.,” *Cell*, vol. 125, no. 2, pp. 315–26, Apr. 2006.

[77] W. D. Bush, J. Garguilo, F. A. Zucca, A. Albertini, L. Zecca, G. S. Edwards, R. J. Nemanich, and J. D. Simon, “The surface oxidation potential of human neuromelanin reveals a spherical architecture with a pheomelanin core and a eumelanin surface.,” *Proc. Natl. Acad. Sci. U. S. A.*, vol. 103, no. 40, pp. 14785–9,

Oct. 2006.

[78] A. Hennessy, C. Oh, B. Diffey, K. Wakamatsu, S. Ito, and J. Rees, "Eumelanin and pheomelanin concentrations in human epidermis before and after UVB irradiation.," *Pigment Cell Res.*, vol. 18, no. 3, pp. 220–3, Jun. 2005.

[79] S. Ito and K. Wakamatsu, "Quantitative Analysis of Eumelanin and Pheomelanin in Humans, Mice, and Other Animals: a Comparative Review," *Pigment Cell Res.*, vol. 16, no. 5, pp. 523–531, Oct. 2003.

[80] J. Kong, "Analysis and biological activities of anthocyanins," *Phytochemistry*, vol. 64, no. 5, pp. 923–933, Nov. 2003.

[81] M. Mangel, D. S. Berns, and A. Ilani, "Dependence of photosensitivity of bileaflet lipid membranes upon the chlorophyll and carotenoid content," *J. Membr. Biol.*, vol. 20, no. 1, pp. 171–180, Dec. 1975.

[82] K. E. van Holde, K. I. Miller, and H. Decker, "Hemocyanins and invertebrate evolution.," *J. Biol. Chem.*, vol. 276, no. 19, pp. 15563–6, May 2001.

[83] C. Zhang, Y. J. Cheng, J. Chen, S. Wickline, and L. V. Wang, "Label-free photoacoustic microscopy of myocardial sheet architecture.," *J. Biomed. Opt.*, vol. 17, no. 6, p. 060506, Jun. 2012.

[84] R. L. Shelton, W. Jung, S. I. Sayegh, D. T. McCormick, J. Kim, and S. A. Boppart, "Optical coherence tomography for advanced screening in the primary care office.," *J. Biophotonics*, vol. 7, no. 7, pp. 525–33, Jul. 2014.

[85] S. Che, J. Li, J. W. Sheaffer, K. Skadron, and J. Lach, "Accelerating Compute-Intensive Applications with GPUs and FPGAs," in *2008 Symposium on Application Specific Processors*, 2008, pp. 101–107.

[86] M. Zhao, Y. Li, and L. Peng, "FPGA-based multi-channel fluorescence lifetime analysis of Fourier multiplexed frequency-sweeping lifetime imaging.," *Opt. Express*, vol. 22, no. 19, pp. 23073–85, Sep. 2014.

[87] H. Y. Lee, P. D. Raphael, J. Park, A. K. Ellerbee, B. E. Applegate, and J. S. Oghalai, "Noninvasive in vivo imaging reveals differences between tectorial membrane and basilar membrane traveling waves in the mouse cochlea," *Proc. Natl. Acad. Sci.*, vol. 112, no. 10, pp. 3128–3133, Mar. 2015.

[88] S. Abeytunge, R. Toledo-Crow, and M. Rajadhyaksha, "FPGA-based electronics for confocal line scanners with linear detector arrays," in *SPIE BiOS: Biomedical*

Optics, 2009, p. 71840A–71840A–11.

[89] S. Jie, X. Qin, L. Ying, and L. Gengying, "Home-built magnetic resonance imaging system (0.3 T) with a complete digital spectrometer," *Rev. Sci. Instrum.*, vol. 76, no. 10, p. 105101, Oct. 2005.

[90] G.-D. Kim, C. Yoon, S.-B. Kye, Y. Lee, J. Kang, Y. Yoo, and T. Song, "A single FPGA-based portable ultrasound imaging system for point-of-care applications.," *IEEE Trans. Ultrason. Ferroelectr. Freq. Control*, vol. 59, no. 7, pp. 1386–94, Jul. 2012.

[91] S.-L. Chen, Z. Xie, T. Ling, L. J. Guo, X. Wei, and X. Wang, "Miniaturized all-optical photoacoustic microscopy based on microelectromechanical systems mirror scanning.," *Opt. Lett.*, vol. 37, no. 20, pp. 4263–5, Oct. 2012.

[92] L. Wang, K. Maslov, J. Yao, B. Rao, and L. V. Wang, "Fast voice-coil scanning optical-resolution photoacoustic microscopy.," *Opt. Lett.*, vol. 36, no. 2, pp. 139–41, Jan. 2011.

[93] H. F. Zhang, K. Maslov, M. L. Li, G. Stoica, and L. V. Wang, "In vivo volumetric imaging of subcutaneous microvasculature by photoacoustic microscopy.," *Opt. Express*, vol. 14, no. 20, pp. 9317–23, Oct. 2006.

[94] J. T. Oh, M.-L. Li, H. F. Zhang, K. Maslov, G. Stoica, and L. V. Wang, "Three-dimensional imaging of skin melanoma in vivo by dual-wavelength photoacoustic microscopy.," *J. Biomed. Opt.*, vol. 11, no. 3, p. 34032, Jan. 2006.

[95] R. G. M. Kolkman, M. J. Mulder, C. P. Glade, W. Steenbergen, and T. G. van Leeuwen, "Photoacoustic imaging of port-wine stains.," *Lasers Surg. Med.*, vol. 40, no. 3, pp. 178–82, Mar. 2008.

[96] K. H. Song, E. W. Stein, J. A. Margenthaler, and L. V. Wang, "Noninvasive photoacoustic identification of sentinel lymph nodes containing methylene blue in vivo in a rat model.," *J. Biomed. Opt.*, vol. 13, no. 5, p. 054033, Jan. 2008.

[97] V. P. Zharov, E. I. Galanzha, E. V Shashkov, J. W. Kim, N. G. Khlebtsov, and V. V Tuchin, "Photoacoustic flow cytometry: principle and application for real-time detection of circulating single nanoparticles, pathogens, and contrast dyes in vivo.," *J. Biomed. Opt.*, vol. 12, no. 5, p. 051503, Jan. 2007.

[98] Y. Hou, S. W. Huang, S. Ashkenazi, R. Witte, and M. O'Donnell, "Thin polymer etalon arrays for high-resolution photoacoustic imaging.," *J. Biomed. Opt.*, vol. 13, no. 6, p. 064033, Jan. 2008.

[99] W. Shi, P. Shao, P. Hajireza, A. Forbrich, and R. J. Zemp, “In vivo dynamic process imaging using real-time optical-resolution photoacoustic microscopy.,” *J. Biomed. Opt.*, vol. 18, no. 2, p. 26001, Feb. 2013.

[100] G. York and Y. Kim, “Ultrasound processing and computing: review and future directions.,” *Annu. Rev. Biomed. Eng.*, vol. 1, pp. 559–88, Jan. 1999.

[101] Y. Wang, D. Xing, Y. Zeng, and Q. Chen, “Photoacoustic imaging with deconvolution algorithm,” *Phys. Med. Biol.*, vol. 49, no. 14, pp. 3117–3124, Jul. 2004.

[102] J. H. Chang, J. T. Yen, and K. K. Shung, “A novel envelope detector for high-frame rate, high-frequency ultrasound imaging.,” *IEEE Trans. Ultrason. Ferroelectr. Freq. Control*, vol. 54, no. 9, pp. 1792–801, Sep. 2007.

[103] R. A. Colyer, C. Lee, and E. Gratton, “A novel fluorescence lifetime imaging system that optimizes photon efficiency.,” *Microsc. Res. Tech.*, vol. 71, no. 3, pp. 201–13, Mar. 2008.

[104] M. C. Hemmsen, S. I. Nikolov, M. M. Pedersen, M. J. Pihl, M. S. Enevoldsen, J. M. Hansen, and J. A. Jensen, “Implementation of a versatile research data acquisition system using a commercially available medical ultrasound scanner.,” *IEEE Trans. Ultrason. Ferroelectr. Freq. Control*, vol. 59, no. 7, pp. 1487–99, Jul. 2012.

[105] T. E. Ustun, N. V Iftimia, R. D. Ferguson, and D. X. Hammer, “Real-time processing for Fourier domain optical coherence tomography using a field programmable gate array.,” *Rev. Sci. Instrum.*, vol. 79, no. 11, p. 114301, Nov. 2008.

[106] Z. Xie, S. Jiao, H. F. Zhang, and C. A. Puliafito, “Laser-scanning optical-resolution photoacoustic microscopy,” *Opt. Lett.*, vol. 34, no. 12, p. 1771, Jun. 2009.

[107] J. Karlsson, J. von Hofsten, and P. E. Olsson, “Generating transparent zebrafish: a refined method to improve detection of gene expression during embryonic development.,” *Mar. Biotechnol. (NY).*, vol. 3, no. 6, pp. 522–7, Nov. 2001.

[108] M. Liebling, A. S. Forouhar, M. Gharib, S. E. Fraser, and M. E. Dickinson, “Four-dimensional cardiac imaging in living embryos via postacquisition synchronization of nongated slice sequences.,” *J. Biomed. Opt.*, vol. 10, no. 5, p. 054001, Jan. 2005.

[109] N. Rana, M. Moond, A. Marthi, S. Bapatla, T. Sarvepalli, K. Chatti, and A. K. Challa, “Caffeine-induced effects on heart rate in zebrafish embryos and possible

mechanisms of action: an effective system for experiments in chemical biology.," *Zebrafish*, vol. 7, no. 1, pp. 69–81, Mar. 2010.

[110] G. Ku, K. Maslov, L. Li, and L. V. Wang, "Photoacoustic microscopy with 2-microm transverse resolution.," *J. Biomed. Opt.*, vol. 15, no. 2, p. 021302, Jan. 2010.

[111] Y. Yamaoka, M. Nambu, and T. Takamatsu, "Fine depth resolution of two-photon absorption-induced photoacoustic microscopy using low-frequency bandpass filtering.," *Opt. Express*, vol. 19, no. 14, pp. 13365–77, Jul. 2011.

[112] D. S. Gareau, S. Abeytunge, and M. Rajadhyaksha, "Line-scanning reflectance confocal microscopy of human skin: comparison of full-pupil and divided-pupil configurations.," *Opt. Lett.*, vol. 34, no. 20, pp. 3235–7, Oct. 2009.

[113] R. L. Shelton, S. P. Mattison, and B. E. Applegate, "Volumetric imaging of erythrocytes using label-free multiphoton photoacoustic microscopy.," *J. Biophotonics*, vol. 7, no. 10, pp. 834–840, Oct. 2014.

[114] M. Zhao, F. Antunes, J. W. Eaton, and U. T. Brunk, "Lysosomal enzymes promote mitochondrial oxidant production, cytochrome c release and apoptosis.," *Eur. J. Biochem.*, vol. 270, no. 18, pp. 3778–86, Sep. 2003.

[115] A. Taruttis and V. Ntziachristos, "Advances in real-time multispectral optoacoustic imaging and its applications," *Nat. Photonics*, vol. 9, no. 4, pp. 219–227, Mar. 2015.

[116] R. W. Cole, T. Jinadasa, and C. M. Brown, "Measuring and interpreting point spread functions to determine confocal microscope resolution and ensure quality control.," *Nat. Protoc.*, vol. 6, no. 12, pp. 1929–41, Dec. 2011.

[117] C. Y. Dong, K. Koenig, and P. So, "Characterizing point spread functions of two-photon fluorescence microscopy in turbid medium.," *J. Biomed. Opt.*, vol. 8, no. 3, pp. 450–9, Jul. 2003.

[118] H. D. Cavanagh, W. M. Petroll, H. Alizadeh, Y. G. He, J. P. McCulley, and J. V. Jester, "Clinical and Diagnostic Use of In Vivo Confocal Microscopy in Patients with Corneal Disease," *Ophthalmology*, vol. 100, no. 10, pp. 1444–1454, Oct. 1993.

[119] A. Ruiz-Vela, G. González de Buitrago, and C. Martínez-A, "Nuclear Apaf-1 and cytochrome c redistribution following stress-induced apoptosis.," *FEBS Lett.*, vol. 517, no. 1–3, pp. 133–8, Apr. 2002.

[120] G. A. Ordway and D. J. Garry, "Myoglobin: an essential hemoprotein in striated

muscle.," *J. Exp. Biol.*, vol. 207, no. Pt 20, pp. 3441–6, Sep. 2004.

[121] C. F. Kaminski, J. Hult, and M. Aldén, "High repetition rate planar laser induced fluorescence of OH in a turbulent non-premixed flame," *Appl. Phys. B Lasers Opt.*, vol. 68, no. 4, pp. 757–760, Apr. 1999.

[122] W. J. Wadsworth, A. Ortigosa-Blanch, J. C. Knight, T. A. Birks, T. P. M. Man, and P. S. J. Russell, "Supercontinuum generation in photonic crystal fibers and optical fiber tapers: a novel light source," *J. Opt. Soc. Am. B*, vol. 19, no. 9, p. 2148, Sep. 2002.

[123] D. Koeplinger, M. Liu, and T. Buma, "Photoacoustic microscopy with a pulsed multi-color source based on stimulated Raman scattering," in *2011 IEEE International Ultrasonics Symposium*, 2011, pp. 296–299.

[124] G. P. Agrawal, *Nonlinear Fiber Optics*, 4th ed. New York: Academic Press, 2007.

APPENDIX A

LAYPERSON EXPLANATION OF DISSERTATION WORK

Disclaimer

This section is meant to serve as an introduction to the science and engineering problems addressed in this manuscript and provide context regarding the importance of this work to readers without an engineering or scientific background. The goal of this section is to concisely convey the core concepts of the completed. As is the case throughout all levels of education, the ideas presented in this section are a simplification of more complicated processes. For a more detailed discussion of any of the topics, refer to the main section of the manuscript.

Photoacoustic Microscopy

In gases, temperature and volume are inversely related. However, an increase in temperature with a fixed volume cannot follow this rule so instead there is an increase in pressure. The opposite, a decrease in temperature will lead to a decrease in pressure, is also true. While the samples for photoacoustic microscopy are not always gases, the core concepts remain the same; an increase in temperature generates an increase in pressure.

Photoacoustic microscopy is a technique that may be used to image the absorption of light by small objects. When light is absorbed, the energy of the light is often converted to heat. This is why the earth typically gets warmer during the day; the light from the sun is absorbed by the earth which generates heat. Instead of a constant light source, like the

sun, photoacoustic microscopy uses very short bursts of light. The rapid changes in temperature generated by these short bursts of light do not allow the volume of the sample to change; instead the bursts generate rapid changes in pressure. Repetitive changes in the pressure of the air are in essence sound. For this reason, the changes in pressure generated by the absorption of light may then be detected as sound hence the acoustic part of photoacoustics. This phenomenon is known as the photoacoustic effect and was first reported by Alexander Graham Bell in the 1800s when he was developing ideas for the telephone.

In photoacoustic microscopy, a short burst of light is tightly focused to a small spot, and moved across a sample. Whenever the light is focused on an absorber, a sound is generated. This works in a similar fashion to a metal detector. You slowly move the metal detector across the ground until you hear a noise that tells you there is something under the ground. Photoacoustic microscopy is moving across the sample looking for the "metal" it is meant to detect.

A limitation of this technique is the focusing of the beam only confines the image in two-dimensions and cannot determine where the signal is coming from in the third dimension. So essentially, you have no depth perception and what you are looking for could be 2 cm in front of you or 2 km. Instead, the depth of the signal is determined by the response of the ultrasound transducer. Unfortunately, ultrasonic transducers do not create an image but provide data that can be used to create an image, and converting from the signal to an actual image creates a delay between capturing the data and showing the image to the user.

Signal enveloping is a general purpose technique technique used to accurately convert from an ultrasound signal to an image. Unfortunately the computations required to perform signal enveloping are all very hard for a computer to do quickly. This means that photoacoustic data must be collected then processed before displaying the results to the user. This requirement of separate processing makes it difficult to utilize photoacoustic microscopy when trying to image rapidly changing systems, like those found in biological applications. A good comparison for this is when 3D movies were first being shown in theaters. The result was often that the film was left choppy and rather than flowing smoothly like it does today.

A specialized computer known as a field programmable gate array was utilized to perform signal enveloping. While a typical central processing unit of a computer may only perform a few tasks simultaneously, the design of a field programmable gate array can perform thousands of tasks simultaneously. This allows for the processing steps of signal enveloping to occur as data is collected and transmit the processed data to the user without any observable delay.

Implementing signal enveloping for photoacoustic microscopy enables high speed photoacoustic imaging of biological systems. With this system, the beating heart of a zebrafish was imaged and displayed to the user in real time. Without the implementation of signal enveloping on the field programmable gate array, this would have required several minutes to accurately display the data to the user. In medicine the removal of this delay is imperative. If photacoustic microscopy was being used to guide the removal of a tumor, any delay would lead to the surgeon missing parts of the tumor.

Transient Absorption Ultrasonic Microscopy

A limitation of photoacoustic microscopy is that the focusing of the beam only confines the generation of the image in two-dimensions and cannot determine where the signal is coming from in the third dimension. Instead the depth of the signal is determined by the response of the ultrasound transducer as was discussed in the previous section. While this is okay for some imaging applications, truly high resolution photoacoustic microscopy for single cells requires the origin of the photoacoustic signal be confined in three dimensions with the location of the signal known in all three dimensions which allows excellent depth perception. Transient absorption ultrasonic microscopy is one approach to obtain the location of the depth of the signal without the limitations of an ultrasound transducer.

Transient absorption ultrasonic microscopy typically utilizes two laser sources, called a pump beam and a probe beam that are separated in time by one billionth of a second. When the pump beam is absorbed by the sample, the absorption of the sample is temporarily modified. If the probe beam arrives before the absorption of the sample returns to normal, the photoacoustic signal will be slightly modified. These overlapping signals provide reference in the third dimension and are how the depth can be accurately determined.

The time difference between the pump and probe beams is so small that the high resolution signal is mixed with the typical lower resolution photoacoustic response. In order to extract the high resolution signal (the information needed to determine the depth of the image) a mathematical operation known as a Fourier transform is required. A

Fourier transform takes the change in signal over time and reports the frequencies of any repetitive signals. Therefore, by knowing how many times per second (the frequency) the pump beam is shined onto the sample and how many times per second (the frequency) the probe beam is incident on the sample, the Fourier transform may be utilized to find the high resolution signal. Any signal that occurs at this the sum of the pump frequency and the probe is known to be the high resolution signal.

A major limitation of transient absorption ultrasonic microscopy is the requirement of a pump and a probe beam. However, if the pump and probe beams arrive simultaneously and occur at the same frequency they may be replaced by a single beam and the high resolution signal may be extracted at twice the frequency of the single beam providing a location, in depth, for the image. This approach greatly simplifies the optical design of a transient absorption ultrasonic microscope, enabling any photoacoustic microscope to be easily converted to a photoacoustic microscope.

Utilizing Transient Absorption Ultrasonic Microscopy, the first ever fully accurate three dimensional image of a red blood cell was captured. Additionally, this approach enables the imaging of the power houses of cells, mitochondria. Imaging of mitochondria has major potential applications in monitoring cancer treatments, developing new medicines, and understanding cell metabolism and could change the diagnosis procedures for many health problems dramatically as more information could be identified without invasive procedures.

APPENDIX B

LABVIEW PROGRAMMING OF A FIELD PROGAMMABLE GATE ARRAY FOR TRANSIENT ABSORPTION ULTRASONIC MICROSCOPY

Background

Field Programmable gate arrays (FPGAs) consist of billions of transistors that make up configurable logic blocks capable of complex mathematics, digital filtering, and high-speed synchronization. The FPGA logic blocks are interconnected by a programmable wiring mesh that allows complete reconfigurations of the signal routing. This design provides flexibility for a variety of applications and reconfigurable programming based on application needs.

Typically, FPGAs must be programmed in hardware description languages such as very high speed integrated circuit (VHSIC) hardware description language (VHDL) or Verilog. These languages require specific knowledge of the hardware being utilized and intensive training to understand coding syntax. Fortunately, high level programming languages such as MATLAB (MathWorks) and LabView (National Instruments) have developed compilers for translating their code to a hardware descriptive language for specific FPGA targets. The introduction of this level of abstraction makes programming of FPGAs available to a broader range of backgrounds at the cost of full optimization of the code.

In this appendix, an overview of the LabView programs written to perform the necessary processing onboard the FPGA is described. This is meant to be a high level look

at the logic behind the program designs and not an in-depth step by step breakdown of the code.

Single Cycle Timed Loops and Pipelining

Single cycle timed loops are 'while loops' that run at a specified clock speed, providing a mechanism for precise timing of events. For the application of TAUM and PAM the utilized clock speed is 80 MHz as set by the digitizer. However, clock speed may be faster or slower for other applications. Any sequence of commands executed within a single cycle time loop must be completed within one update of the FPGA clock cycle. This implies a fundamental limit of the electron physically traveling across the circuit board. Complicated commands that must be performed within a single cycle timed loop may instead be broken up into finite steps through a process known as data pipelining. Data pipelining allows complex calculations requiring multiple clock cycles to be parallelized for increased efficiency. Using parallel processing, these steps can be performed simultaneously on multiple data points.

First In First Out Arrays

First In First Out (FIFO) arrays are mechanisms for the FPGA to pass large datasets both across the FPGA target and between the FPGA target and the Host computer. All of the properties, including the data type, the maximum size, and the scope, of a FIFO array are defined by the user during the initial setup of the LabView project. A target-scoped FIFO array enables the flow of data between two single cycle timed loops in the FPGA code. Host-to-target and target-to-host FIFO arrays are the easiest and most efficient way

to transfer large datasets between the host computer and the target FPGA. It is important to remember that while memory on the FPGA is limited, the host computer may allocate large amounts of FIFO memory for data transfer. Additionally, FIFO arrays may easily be monitored for attempts to write data that will not fit into the allocated size of the FIFO, providing an ideal tool for monitoring for data loss.

Xilinx Intellectual Property Cores

Xilinx intellectual property cores are third party FPGA programs written for use in LabView FPGA. When implemented in code, the user will be prompted to set the parameters of the Xilinx intellectual property core using a graphical user interface. Each Xilinx intellectual property core comes with a manual for setting parameters. Some essential Xilinx intellectual property cores for LabView FPGA include single cycle time loop optimized code for large dataset size fast Fourier transforms and custom finite impulse response filters.

Acquisition of Raw Photoacoustic Signal

Due to the large difference between the speed of sound in water and the speed of light in water, there is a significant delay between the arrival of the excitation pulse and the acquisition of the photoacoustic signal. Additionally, there is a significant temporal difference between the duration of the photoacoustic signal and the time between laser pulses. Thus, it becomes necessary to trigger the photoacoustic acquisition based on the acquisition of a trigger from the laser. This trigger may be generated either by the laser itself, or by a photodiode detecting a light source. Therefore one of the input channels on

the FPGA data acquisition board is used for reading of the input trigger. When this occurs, the FPGA is triggered and the program begins waiting for the arrival of the relevant photoacoustic signal. This processing is best performed in a state machine as outlined in the state diagram provided in Figure B-1.

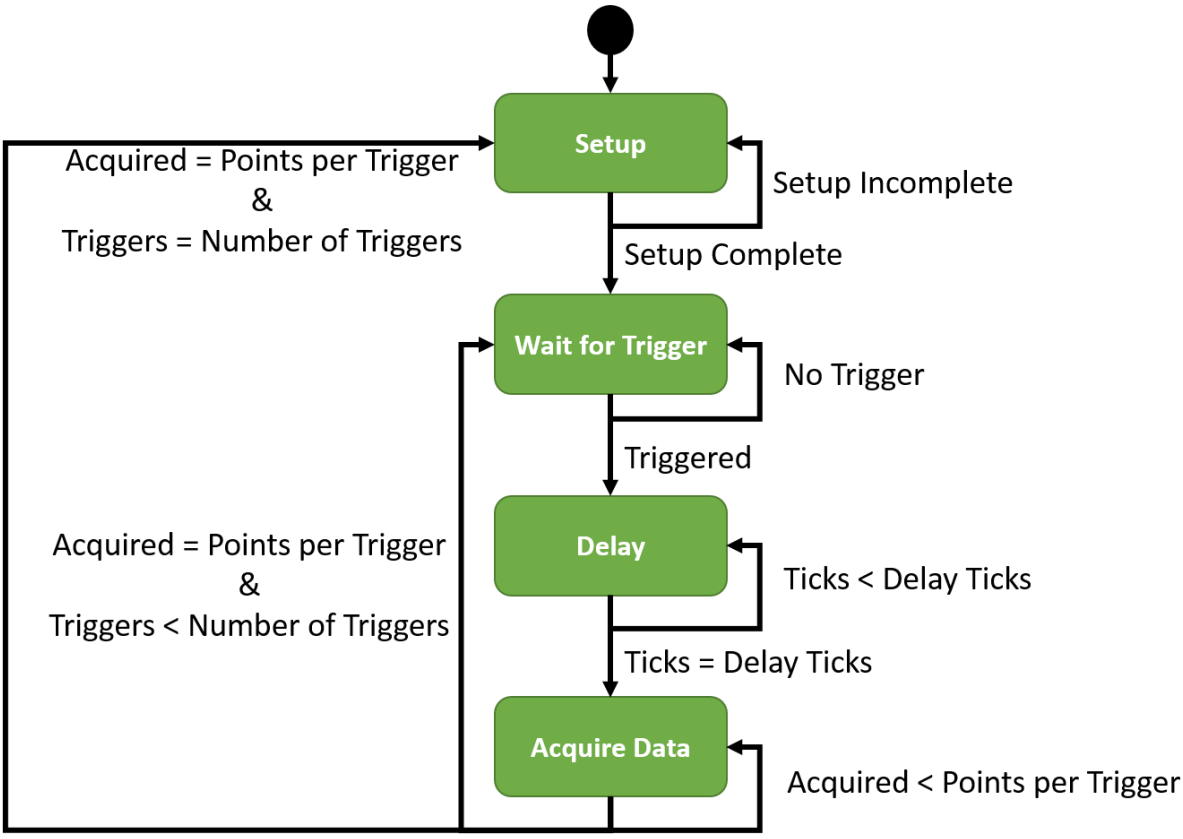

Figure B-1. State diagram for raw photoacoustic signal acquisition.

An initial ‘Setup’ state is used to define variables such as the “trigger threshold”, the delay between the trigger and the photoacoustic signal, and the number of points to acquire per laser trigger. Once leaving the ‘Setup’ state, the signal from the trigger input is monitored over time over time by the ‘Wait for trigger’ state. A trigger is defined as a data

point where the previous data point was below the “trigger threshold” and the current data point is above the “trigger threshold”. Once a trigger is received, the system waits in a ‘Delay’ state until the number of clock ticks corresponding to the time between the laser pulse arrival and the detection of photoacoustic signal. Finally, the system enters an ‘Acquire Data’ state which reads input from the ultrasound transducer for a specified number of points and inputs it into a target-scoped FIFO array. From this state the system either resets to ‘Wait for Trigger’ to await the next trigger or returns to the ‘Setup’ state to acquire more data based on whether the number of expected triggers have arrived.

Figure B-1 represents an idealized case where the delay is shorter than the time between laser pulses. When this state changes, it becomes necessary to monitor for additional triggers while delaying and acquiring data. Eventually, at high enough repetition rates, it no longer remains a necessity to trigger the data acquisition after the first pulse as the ratio between the duration of the photoacoustic signal and the interpulse delay becomes negligible.

State Machine for Triggered Fast Fourier Transform

In LabView FPGA, utilizing a triggered Fast Fourier Transform (FFT) has a few unique quirks. First, the enabling of the FFT core and the input for the data being valid are tied to one another. This means if the data being sent to the FFT should be ignored, as is the case when the photoacoustic signal is not being acquired, the FFT stops running entirely. As such it is necessary to use a state machine to control the flow of data into and

out of the FFT node. Figure B-2 provides a state diagram of the data control state machine for the FPGA based FFT.

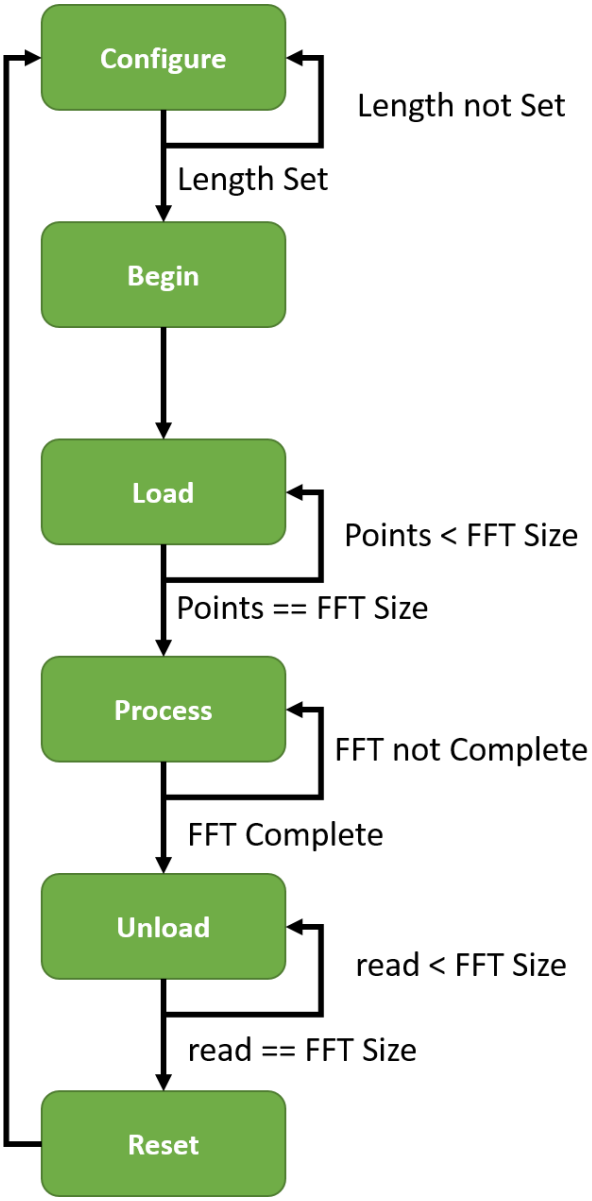

Figure B-2. State diagram for controlling the flow of data into and out of the LabView FPGA FFT node.

The flow of data through this state machine is outlined in the Control Data Flow Graph shown in Figure B-3.

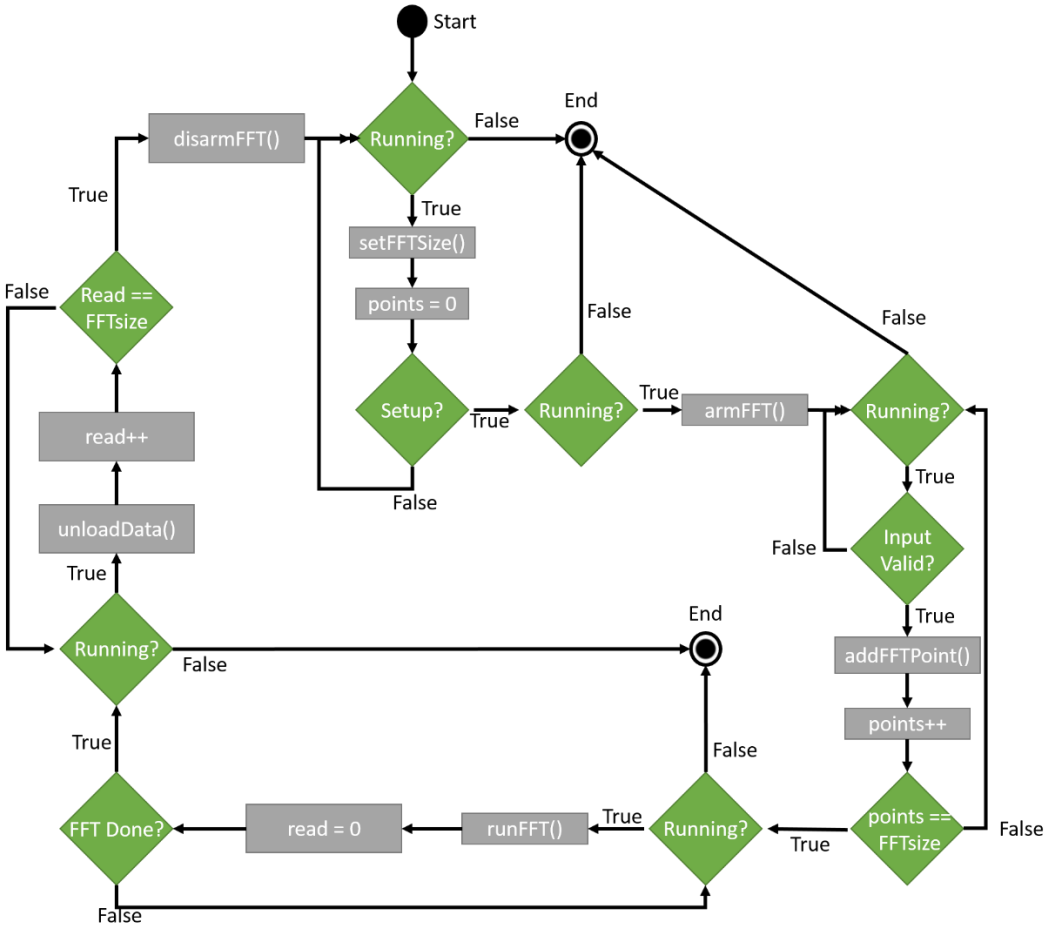

Figure B-3. Control Data Flow Graph of the state machine controlling the FFT node for LabView FPGA.

As can be seen in Figure B-3, after ever update of the single cycle timed loop this state machine is found within, the program must first make sure it is still running. Next, necessary steps are performed within the confines of the single cycle timed loop and the conditionals are checked to see if the state should be changed. In the ‘Setup’ state, the size

of the FFT size is set and a counter for the number of points that have been fed into the FFT node is set to zero. When the user sends the command that the FFT is setup, the FFT is armed within the ‘Begin’ state and the program immediately enters the ‘Load’ state. Within the load state, data is read point-by-point from the target-scoped FIFO containing the raw PAM data. The data is then added to the FFT node and a count of the number of points waiting to undergo FFT is updated. Once the number of points loaded to the FFT node is equal to the length of the desired FFT, the system enters the ‘Process’ state. Within the process state, the FFT will run in pipelined increments until completion and a counter of the number of points read from the FFT will be set to zero. Once the FFT finishes, the system enters the ‘Unload’ state which reads both the real and imaging data point-by-point from the FFT node and into a square root of the sum of squares node. Once all of the points have been read from the FFT, the system enters the ‘Reset’ state for one clock cycle, the FFT is disarmed, and the system returns to the ‘Setup’ state. Following the square-root of the sum of squares node, data is transferred to the Host via a target-to-host scoped FIFO.

Closing Remarks

This section has been a quick overview of the control necessary for utilizing LabView FPGA for performing TAUM processing. This approach to performing FFT processing allows for high speed data acquisition and processing of TAUM data at laser repetition rates up to 5 MHz. It is important to note that all of this work was done in LabView 2013. Newer versions of LabView may have been developed with more elegant solutions for handling triggered FFTs.